Investigation of Coherent Diffraction Radiation from a dual target system at CTF3 and its application for longitudinal bunch profile diagnostics

Konstantin Lekomtsev

Department of Physics

Royal Holloway, University of London

A thesis submitted to the University of London for the degree of Doctor of Philosophy

February 2012

Declaration of Authorship

I Konstantin Lekomtsev hereby declare that this thesis and the work presented in it is entirely my own. Where I have consulted the work of others, this is always clearly stated.

Signed:

Date:

Abstract

A coherent Diffraction Radiation (CDR) originating from a dual-target system was investigated theoretically and experimentally. Diffraction Radiation is emitted when a bunch of charged particles moves in the vicinity of an optical obstacle. The coherency of the effect is achieved when electrons in the bunch radiate in phase, i.e. the wavelength of the radiation is comparable to or larger than the bunch length. An experimental setup at the CLIC Test Facility 3 (CTF3) at CERN was modified by installation of a second target. In the experiment two targets are positioned to one side of the beam and the radiation originating from them is translated towards a Michelson interferometer. The ultimate goal of the experiment is to reconstruct the longitudinal parameters of the beam from the CDR spectrum. A precise knowledge of the bunch time profile is particularly important in the context of a luminosity challenge in the future linear colliders and therefore the development of a non-invasive and robust longitudinal beam diagnostic technique is very important.

A theoretical model based on the classical Diffraction Radiation theory was developed to calculate the spatial distributions of the CDR from the dual-target system and based on this knowledge to calculate a single electron spectrum which is used in a bunch shape reconstruction. The Kramers-Kronig analysis as a tool for the bunch profile reconstruction was studied theoretically. The CDR spatial distributions were measured at the experimental setup and compared with the theory. The ability of the two-target system to cut-off the backgrounds originating upstream of the experimental setup was tested. The influence of the bunch length and shape instabilities at CTF3

on the measurements was investigated. The interferometric measurements of the CDR were performed. A clear understanding of the hardware constraints was achieved and the possible improvements to the experimental setup were suggested.

Acknowledgements

This work is dedicated to my parents Valentina and Vladimir Lekomtsev. I am truly grateful to them for their help, guidance and never ending emotional support.

I would like to express my gratitude to my supervisor Dr. Pavel Karataev for his supervision, guidance and interesting scientific discussions in the last three years. Without his help this thesis would not have been possible.

I would like to thank all of my colleagues at John Adams Institute at Royal Holloway, University of London. I would like to express my gratitude to Professor Grahame Blair for giving me an opportunity to perform my research at physics department of Royal Holloway, University of London. I am thankful to Dr. Stewart Boogert, Dr. Stephen Molloy and Dr. Alexey Lyapin for interesting scientific discussions and general advice.

I am expressing my gratitude to all members of the CLIC / CTF3 collaboration at CERN. I would like to thank Dr. Roberto Corsini, Dr. Frank Tecker and Dr. Thibaut Lefevre for an opportunity to participate in the CTF3 operation over the course of 2010 - 2011. Special thank you to Dr. Xavier Barranco, Dr. Steffen Döebert and Dr. Guido Sterbini for their active interest in the CDR project and help during my time at CERN.

I would like to thank my colleagues and friends Nirav Joshi, Dr. Maximilian Micheler, Robert Ainsworth, William Shields, Francis Cullinan and Tom Aumeyr for creating a very friendly working environment during my time at Royal Holloway and CERN.

I would also like to acknowledge the DITANET scientific network for an extensive

training program and providing me with the funds necessary for the completion of my PhD research.

Contents

List of Figures

List of Tables

Chapter 1

Introduction

The Large Hadron Collider (LHC) will probe a tera-scale energy region and provide a future physics agenda at a new high energy frontier. In this energy domain LHC will study validity of the Standard model and explore the possibilities for physics beyond it. The required beam collision energy range will be better defined by the LHC results when substantial integrated luminosity will have been accumulated, estimated to be by 2015.

Following the successful development and operation of the 100 GeV centre of mass SLAC Linear Collider (SLC), the only linear collider built so far, extensive R&D has greatly improved the design of linear colliders and their potential performance. Currently there are two alternative technologies under development. The International Linear Collider (ILC) aiming at 500 GeV energy for colliding beams, possibly upgradeable to 1 TeV, is based on the beam acceleration by super-conducting RF structures. The second alternative is the Compact Linear Collider (CLIC), which will potentially explore the possibility to extend the energy of the linear colliders to the multi-TeV energy range by developing a novel technology of two-beam acceleration [1]. CLIC aims to accelerate electron and positron beams with 100 MV/m accelerating gradient up to 3 TeV centre of mass energy. Currently a possibility to build a 500 GeV CLIC is considered.

Development of low-cost and robust beam diagnostic techniques is of an ultimate importance for the future linear colliders. In this thesis a longitudinal beam profiling

technique based on the detection of Coherent Diffraction Radiation from a dual-target system will be considered in detail.

1.1 CLIC

CLIC is based on a two-beam acceleration scheme. Power for acceleration is transported to acceleration structures by the second electron beam, the drive beam, which runs parallel to the main beam. The power is extracted from the drive beam and converted into RF power in special RF devices called PETS (Power Extraction and Transfer Structures), it is then transported to the accelerating structures of the main beam.
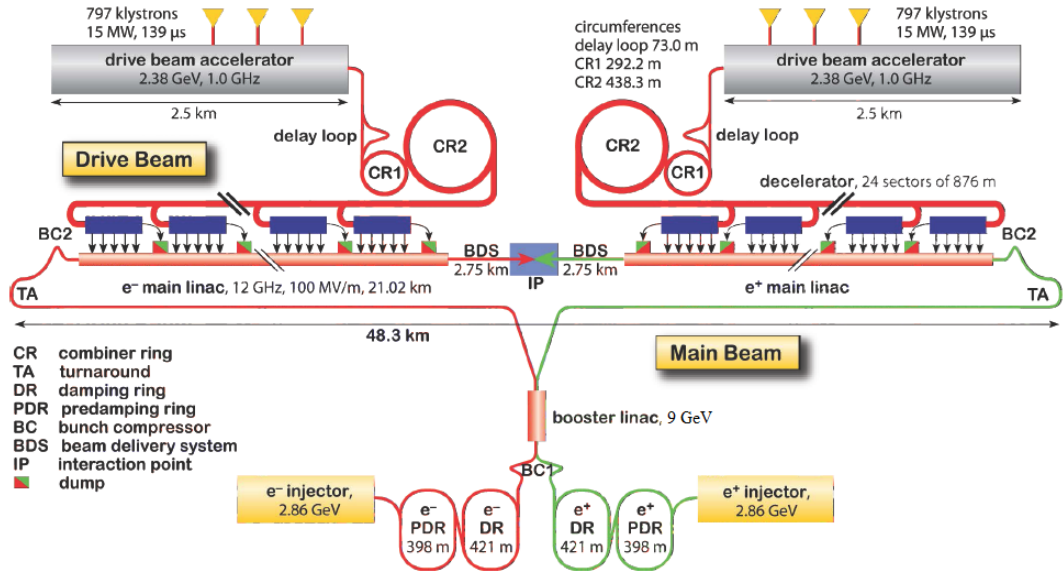
Figure 1.1: CLIC layout at 3 TeV.

A schematic layout of 3 TeV CLIC is shown in figure 1.1 [2]. The drive beam is generated from a 140 μs bunch train with a nominal charge per bunch of 8.4 nC, initial beam has a large bunch spacing and a low average power. The final time structure of the beam is achieved by a pulse compression using a bunch interleaving technique. The drive beam carries the total power required for the acceleration of the main beam, this power is generated by a drive beam accelerator (DBA). The DBA accelerates long trains of bunches (140 μs) in a normal conducting linac with an acceleration frequency of 999.5 MHz. High efficiency klystrons can be used as RF power sources for the

drive beam. The DBA is operated under full beam loading conditions, which means that no RF power leaves an accelerating structure. All the power with exception of wall current losses is converted into the beam power. The CLIC Test Facility (see section 1.6) routinely demonstrates this type of operation and a transfer efficiency of RF power reaches 93 % [3].

The beam in DBA is phase coded, it consists of 243.7 ns long sub-trains with a bunch repetition frequency of $f_r = 499.75$ MHz as only every second bucket of a train is occupied. After each sub-train the bunches are switched from odd to even buckets. An RF deflector positioned at the entrance to the delay loop and operating at the bunch repetition frequency deflects subsequent trains either into the delay loop or along the straight path. If the flight time of the electrons between the two paths exactly matches the length of the train, the bunches of the delayed train are placed between the bunches of the train travelling in the straight path by a second RF deflector. Consequently, the recombined train bunch repetition frequency and the peak current are doubled (see figure 1.2) [3].

After the beam recombination in the delay loop the trains are injected into the first combiner ring which has a circumference of twice that of the delay loop. Two RF deflectors create a closed orbit bump. They operate at the frequency $f_0 = 2f_r = 999.5$ MHz and are spaced by the distance $(n + 1/2) \times \lambda_0$ where $\lambda_0 = c/f_0$ and n is an integer. The second deflector compensates a transverse kick created by the first one. The beam is injected in between the two deflectors at the maximum of the deflecting field. After one turn the bunches of the newly arrived train are interleaved in between the already circulating ones. For a combination factor m the bunches are placed in between the bunches of the first injected train at an distance λ_0/m. This principle is demonstrated in figure 1.3 [3].

CLIC will have two combiner rings, the first one with a combination factor three and the second one with a factor four. The first ring will have a circumference of 292.2 m with an RF deflector operating at 1 GHz. The second combiner ring will have a circumference of 438.3 m and an RF deflector operating at 3 GHz. After the second combiner ring the final beam structure will be obtained with a bunch repetition frequency increased to 12 GHz and a peak current enhanced by a factor of 24 from
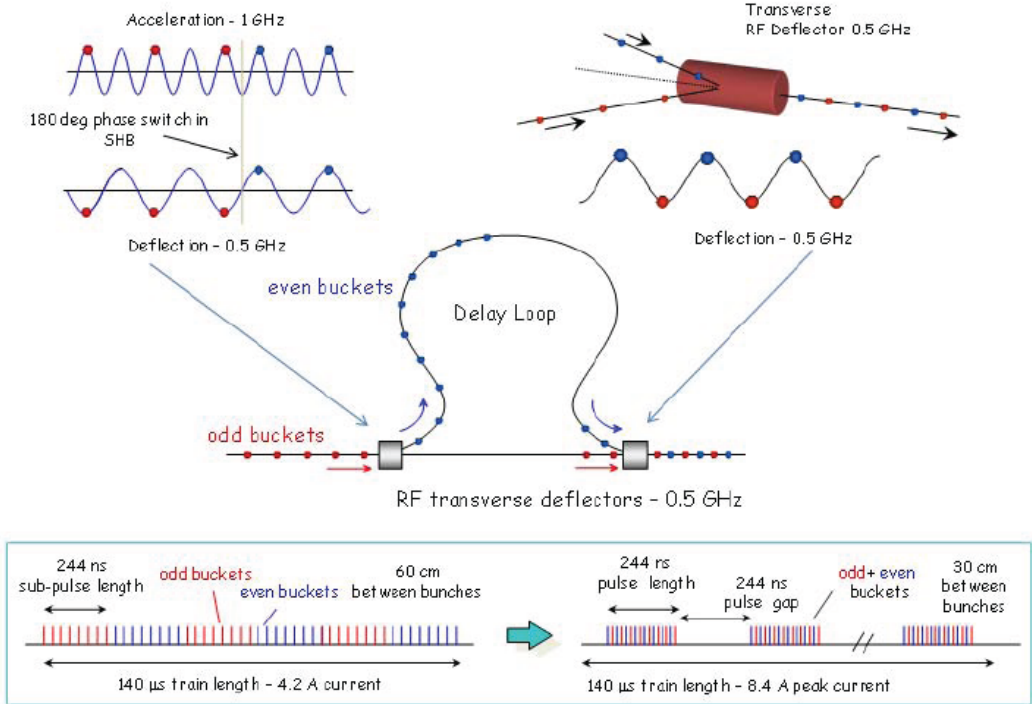
Figure 1.2: Principle of bunch combination of the CLIC delay loop.
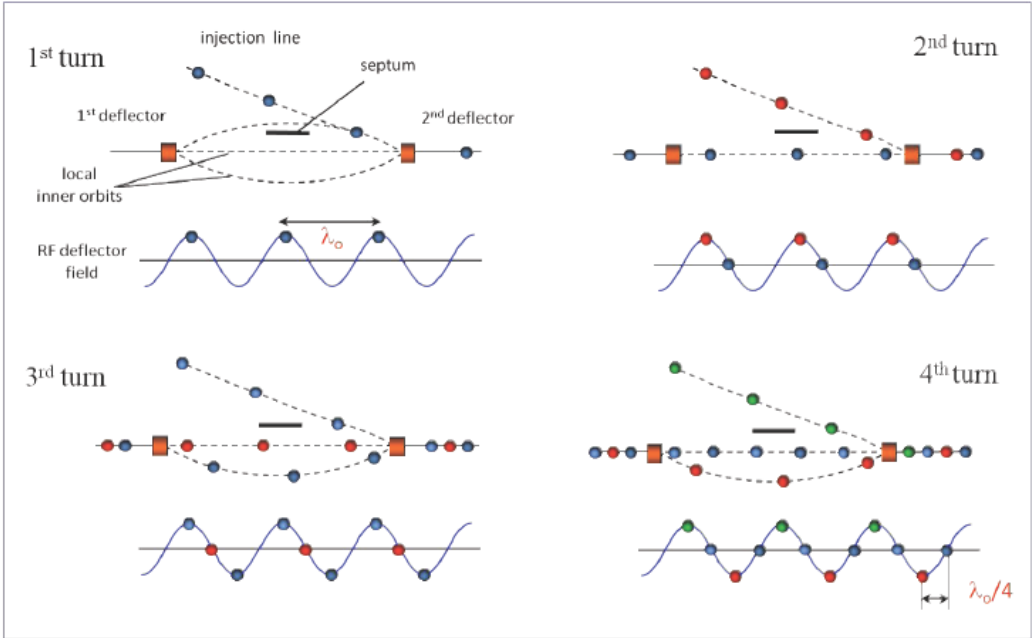
Figure 1.3: Principle of bunch combination in the CLIC combiner ring with a combination factor four.

4.2 A to 101 A. The drive beam will consist of 24 trains each 243.7 ns in length and a separation of 5.8 μs. A nominal bunch charge of 8.4 nC will remain unchanged.

CLIC will have a main beam injector complex consisting of the electron and positron sources producing polarised beams. Predamping and damping rings will be built to minimise a horizontal emittance. Bunch compressors after the damping rings and a booster linac will accelerate the main beams up to 9 GeV.

A power extraction section of CLIC will be divided into about 876 m long sectors each with 2,928 accelerating structures accelerating the main beam by 62.5 GeV. As was mentioned earlier the drive beam power is extracted using PETS in a way that one PETS provides RF power for two accelerating structures. The drive beam trains need a relatively low energy of 2.38 GeV, but a very high peak current of about 100 A along the pulse. About 65 % of their stored energy is converted into the RF power at the input of an acceleration structure (PETS to acceleration structure efficiency reaches 93.8 %), after which the drive beams are dumped at the end of the sectors. At this point a new drive beam train arrives to supply the following linac sector over the next 876 m with 2,928 accelerating structures. Each of the two main linacs consists of 24 such sectors. This two - beam acceleration scheme offers a good power efficiency and a conversion of power into RF is nearly lossless.

The CLIC innovative scheme has a set of key issues and challenges usually defined by the fact that parameter specifications happen to be above the present state of the art. The key issues have been established and arranged into four categories: feasibility, performance, cost and power issues [4]. All of them have to be addressed before the project can be proposed for approval. In the following section the fundamental CLIC challenges such as a luminosity challenge and an RF power production in PETS will be discussed.

1.2 Luminosity

The luminosity $\mathcal{L}$ of CLIC can be written as [2, 5]:

$$\mathcal{L} \propto H_D \frac{N^2}{\sigma_x^* \sigma_y^*} n_b f_r,\tag{1.1}$$

where H_D is the luminosity enhancement factor representing the combined effect of a "hour-glass" (the change of a beta function in the longitudinal direction over the collision region) and the disruption enhancement (the force that the two colliding beams exert on each other); N is the number of particles per bunch; σ_x^* and σ_y^* are the horizontal and vertical bunch sizes at the interaction point (IP); n_b is the number of bunches per pulse; f_r is the linac repetition rate.

One may see that the smaller the beam cross-section the higher the luminosity. In order to deliver very small beams to the IP, the transverse parameters of the beams have to be precisely monitored.

1.3   Beam-beam effects

Electron-positron linear colliders require a collision of intense $e^+ e^-$ beams to reach a high luminosity. This gives rise to intense electromagnetic beam fields that strongly affect the motion of the particles in the beams. There are two categories of strong-field beam-beam effects: disruption effects and beamstrahlung effects. The former are classical effects associated with the bending of the particle trajectories. The latter are related to the radiation triggered by the bending and similar to synchrotron radiation. The disruption effect causes a modification of the beam size and thus the effective luminosity, the beamstrahlung effect causes a spread of the centre of mass energy.

After collision the beam spectrum is highly influenced by the beamstrahlung photons emitted per electron or positron during the collision in the field of the opposite beam. This effect is characterised by the beamstrahlung parameter Υ, given by [2]:

$$\Upsilon = \frac{N \gamma r_e}{(\sigma_x^* + \sigma_y^*)\sigma_z},\qquad(1.2)$$

where $\gamma = E_b/E_0$ is the beam energy normalised by the rest energy of electron ($E_0 = 511$ keV), r_e is the classical electron radius (2.8179×10^{-15} m); σ_z is the longitudinal beam size at the IP. At low beam energies, which is applicable to the 500 GeV CLIC the beamstrahlung parameter $\Upsilon \ll 1$. For the 3 TeV CLIC the beamstrahlung parameter $\Upsilon \gg 1$. The control of the bunch longitudinal parameters while minimising the beamstrahlung is crucially important.

All disruption effects can be described by two parameters which are defined using the unperturbed beam parameters at the IP. The Lorentz-invariants which are dimensionless disruption parameters in the x and y directions can be represented as [5]:

$$\mathcal{D}_{x,y} \equiv \frac{2 r_e N \sigma_z}{\gamma \sigma_{x,y}^* (\sigma_x^* + \sigma_y^*)}. \tag{1.3}$$

$\mathcal{D} \ll 1$ corresponds to the weak disruption or the weak focusing, while $\mathcal{D} > 1$ is the strong disruption regime where the beam dynamics becomes nonlinear. The divergence parameter can be defined as [5]:

$$A_{x,y} \equiv \frac{\sigma_z}{\beta_{x,y}^*}, \tag{1.4}$$

where $\beta_{x,y}^*$ are two components of the β function at the IP. The $A_{x,y}$ parameter measures the hour-glass effect due to the inherent divergence (emittance) of incoming beams.

The transverse beam size at the IP is strongly reduced and proportional to the β function:

$$\sigma_{x,y}^* \propto \sqrt{\beta_{x,y}^*(s)}. \tag{1.5}$$

Due to the focusing of the beam the β function depends on the longitudinal position s from the IP and can be approximated as:

$$\beta_{x,y}(s) = \beta_{x,y}^* \left(1 + \left(\frac{s}{\beta_{x,y}^*} \right)^2 \right). \tag{1.6}$$

Substituting equation (1.5) into equation (1.6) the bunch size near the IP can be defined as follows:

$$\sigma_{x,y}(s) = \sigma_{x,y}^* \sqrt{\left(1 + \left(\frac{s}{\beta_{x,y}^*} \right)^2 \right)}. \tag{1.7}$$

The variation of the transverse beam size follows a function which looks like a hourglass, that is why this variation is called the hourglass effect. When the bunch length is comparable to or larger than the β function at the IP ($\sigma_z \geq \beta^*$) the hour-glass effect

contributes into the loss of luminosity. One of the ways to minimise the hour-glass effect is to produce very short beams at the IP, which is not a trivial task. In order to deliver the short beams for the collision at the CLIC IP, it is very important to monitor their longitudinal parameters continuously during the beams generation and transfer for over 25 km.

1.4 Power production in PETS

The RF power generated by a beam passing through a periodic structure can be expressed as follows [6]:

$$P = I^2 L^2 F_b^2 \omega_0 \frac{R/Q}{4V_g}, \tag{1.8}$$

where I is the beam current, L is the active length of the structure, F_b is the single bunch form factor, ω_0 is the bunch frequency, R is the impedance per metre of length, Q is the quality factor and V_g is the group velocity. The single bunch form factor directly depends on the peculiarities of the bunch charge distribution, therefore the monitoring and optimisation of the longitudinal parameters of the drive beam is crucially important for an effective RF power production in PETS.

1.5 CLIC parameters

The specific choice of the CLIC parameters is the result of a trade-off between conflicting requirements. High accelerating fields limit the extension of the facility, but reduce the RF to beam efficiency. High RF frequency structures are preferable for a high RF-to-beam efficiency. They reduce the amount of required RF power at the structure input for the high field acceleration, but generate strong wakefields. Beam quality preservation during acceleration in a strong wakefield environment limits the beam current and imposes tight tolerances on the beam alignment and stability. The major CLIC parameters are shown in table 1.1 [7].

The values of the acceleration gradient $G_{unl/l}$ and the main linac RF frequency f_{RF} were chosen based on the studies of the CLIC overall performance. In order to maximise

Table 1.1: CLIC main parameters, as of January 2012.

Parameter	Symbol	Value	Unit
Luminosity	$\mathcal{L}$	5.9	$10^{34}cm^{-2}s^{-1}$
Luminosity (in 1 % of energy)	$\mathcal{L}_{99\%}$	2	$10^{34}cm^{-2}s^{-1}$
Unloaded/loaded gradient	$G_{unl/l}$	120 / 100	MV/m
Main linac RF frequency	f_{RF}	11.994	GHz
Nominal vertical IP beta function	β_y^*	68	μm
Number of particles per bunch	N	3.72×10^9	
Bunch separation	$\triangle_b$	0.5	ns
Number of bunches per train	N_b	312	
Linac repetition rate	f_{rep}	50	Hz
Beam power	P_b	14	MW
Vertical emittance (geometric)	ε_y	20	nm rad
Vertical IP core beam size	σ_y^*	~ 0.9	nm
Bunch length at the IP	σ_z	44	μm
RF to Drive Beam efficiency	$\eta_{b,RF}$	93	%
Transfer efficiency PETS to Accel. Struct.	$\eta_{pets,a.s.}$	93.8	%

the luminosity at the IP, the beam is focused as strongly as possible ($\beta_y^* = 68 \ \mu$m). The large number of electrons per bunch ($N = 3.72 \times 10^9$), the short interval between the bunches $\triangle_b$ and the number of bunches per train N_b are chosen to improve the RF to drive beam efficiency. The linac repetition rate f_{rep} was adopted for a synchronisation of the RF power source with the wall plug power. The above parameters result in 14 MW beam power per 1.5 TeV beam.

An acceptable level of the backgrounds during the collision at the IP and the required luminosity $\mathcal{L}_{99\%}$ imply extremely small geometric vertical emittance $\varepsilon_y = 20$ nm rad (currently beyond the present state of the art, however close to the required performance of the latest generation synchrotron light sources). Strong focusing and the small vertical emittance result in extremely small vertical beam size at the IP ($\sigma_y^* = 1$ nm) which requires tight beam alignment and stability in sub-nanometer range.

The design value of the bunch length at the IP was defined to be 44 μm (147 fs). It requires a longitudinal diagnostic with a resolution of $\sim$ 10 - 20 fs. Potential longitudinal diagnostic candidates which can deliver this scale of resolution will be discussed in chapter 2, section 2.2.
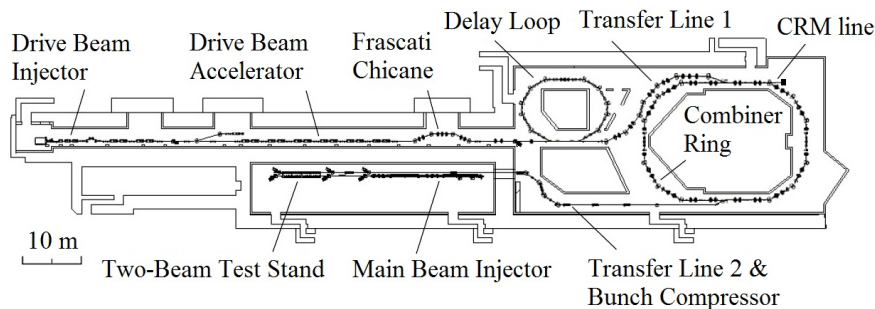
Figure 1.4: CTF3 layout with the main sections indicated.

1.6 CLIC Test Facility (CTF3)

CTF3 is an important test and demonstration facility for many vital components of CLIC. Its main goal is to prove the feasibility of an innovative two-beam acceleration scheme and to produce an effective source of RF power at 12 GHz. The scheme of the facility is shown in figure 1.4 [8].

A 1.6 μs long drive beam pulse is generated by 140 kV, 9 A thermionic triode gun. A time structure of the pulse is obtained in the bunching system which consists of three 1.5 GHz sub-harmonic bunchers, one 3 GHz pre-buncher and one 3 GHz tapered phase velocity travelling wave buncher. The phase of the sub-harmonic bunching cavities is switched rapidly by 180° every 140 ns as needed for the phase coding operation. Obtained bunches are separated by 20 cm and have a charge of 2.3 nC per bunch.

The drive beam injector is completed by two 3 GHz fully-loaded travelling wave structures, increasing the beam energy up to 20 MeV. Solenoidal focusing is used along the injector, a magnetic chicane with collimators downstream of the injector is used to eliminate low energy beam tails produced during the bunching process. In the drive beam accelerator the beam is accelerated up to 120 MeV (the present state of the art, 150 MeV is a design value) using 3 GHz RF travelling wave accelerating structures. Full beam loading is applied during the acceleration stage resulting in the RF to beam efficiency of around 93 %. The RF power is supplied by klystrons with a power ranging from 35MW to 45MW and compressed by a factor 2 to provide 1.5 μs pulses over 30 MW at each structure input. In order to achieve a compressed rectangular output pulse, an RF phase modulation of a klystron input needs to be performed. To compensate the

variation of the output RF phase which leads to the modulation of the beam energy, a minor RF frequency offset is introduced. The required detuning is about 130 kHz. The residual RF phase sag which is a second order effect is compensated by anti-phase operation of alternate klystrons [9].

A Coherent Diffraction Radiation (CDR) setup is installed in the Combiner Ring Measurements line of CTF3. This location allows for detection of CDR as well as Coherent Synchrotron Radiation (CSR) by the same detection system. A detailed explanation of the setup will be given in chapter 6.

1.6.1 Phase coding of bunches in the Delay Loop and the Combiner Ring

One of the most important feasibility issues at CTF3 is demonstration of a frequency multiplication by a novel bunch interleaving technique [10]. In CTF3 a 1.4 μs long bunch train with 20 cm distance between bunches is converted into sequence of short bunch trains with a bunch spacing of 2.5 cm (12 GHz). This is done in two stages, first by the factor two in the delay loop and then by the factor four in the combiner ring. The detailed explanation of this procedure is given in section (1.1) in application to CLIC. In order to maintain a short bunch length in the rings they must be isochronous.

After the linac the first stage of the pulse compression and frequency multiplication is two RF deflectors operating at 1.5 GHz and the delay loop with a circumference of 42 m.

The 84 m Combiner Ring is used for the second stage of the pulse compression and frequency multiplication by the factor four. It is achieved by two RF deflectors which perform the interleaving of the injected bunches in between the circulating ones. The deflectors operate at 3 GHz. After the combiner ring the drive beam pulse is a 140 ns long, has a 28 A beam current, a 2.3 nC bunch charge and a 12 GHz time structure (or 2.5 cm bunch spacing) from the initial beam with a current of 3.5 A and a bunch spacing of 20 cm. The list of the CTF3 parameters explained above is shown in table 1.2 [11].

Table 1.2: CTF3 main parameters, as of January 2012.

Parameter	Value	Unit
Drive beam		
Acceleration frequency	3	GHz
Energy	120	MeV
Number of accelerating structures	16	
Average current after linac	3.5	A
Beam pulse length	1.4	μs
Delay loop length	42	m
Combiner ring length	84	m
Average beam current after compression	28	A
Bunch length in the linac	1.3	mm
Bunch length in the DL and CR	2.5	mm
Bunch length after compression	0.5	mm
Bunch spacing before compression	20	cm
Bunch spacing after compression	2.5	cm
Transverse size of the beam in the CRM line (σ)	~ 1	mm
Normalised emittance in the CRM line	≤ 100	π mm mrad
Probe beam		
RF pulse length	140	ns
Acceleration frequency	12	GHz
Acceleration gradient	100	MV/m
Initial beam energy	180	MeV

1.6.2 Energy spread minimisation

A very short bunch length is required after recombination for efficient 12 GHz power production. For short bunches the impedance of the combiner ring as well as the CSR become very important issues leading to the energy loss and the increase of the energy spread. The energy losses give rise to the relative phase errors between bunches via non-perfect ring isochronicity, resulting in deterioration of the timing between both individual bunches and merging trains. The energy spread leads to the bunch lengthening and phase space distortion. Both the energy spread and the energy losses can significantly affect efficiency of the RF power transfer in PETS.

In order to minimise these effects and achieve the energy spread below 1 %, the bunch length has to be increased from its value of 1.3 mm in the linac to the maximum of 2.5 mm in the delay loop and the combiner ring by using the magnetic chicane positioned at the end of the linac [9]. For an efficient power production after the recombination, the individual bunches are finally compressed in length to about 0.5 mm in the magnetic bunch compressor. They are then injected into the Test Beam Line (TBL) or the Two-Beam Test Stand (TBTS) which are both located in the CLIC Experimental Area (CLEX). The bunch length manipulations before and after the recombination rings require precise monitoring of the longitudinal bunch profile.

1.6.3 Two-beam operation and experiments

One of the key demonstration purposes of CTF3 is the two-beam operation in which RF power is produced efficiently from the drive beam and transferred into the high gradient accelerating structures in the main beam (probe beam in CTF3). For this purpose in the CTF3 CLEX area the Two Beam Test Stand (TBTS) and the probe beam linac called CALIFES(Concept d'Accélérateur Linéaire pour Faisceaux d'Electrons Sondes) are installed to imitate the CLIC two-beam scheme. The TBTS is the only facility where CLIC type structures can be tested with beam, it consists of two parallel beam lines fed with the drive and probe beams. The deceleration and power generation structure, installed in the drive beam, feeds RF power to the accelerating structure in the probe beam.

The probe beam is generated in the 24 m long CALIFES linac which is positioned in the same experimental hall as the TBTS. It was developed to deliver single bunches and bunch trains at 1.5 GHz bunch repetition rate and the energies up to 180 MeV.

A first result of the two beam acceleration in the accelerating structure was obtained in 2011, however only 3 MeV of acceleration was achieved due to low RF input power [11].

1.6.4 Test Beam Line

The Test Beam Line (TBL) will be the first demonstration of the decelerator for CLIC. In the TBL about 54 % of the energy will be extracted from a 28 A electron beam. The line consists of 16 cells each containing a 0.8 m long PETS, one quadrupole on mover and one inductive beam position monitor. The main purposes of the TBL are: to show a stable power production in 16 PETS and to correlate the RF power output with the energy losses and theoretical predictions, to demonstrate a stable beam while converting more than 50 % of the beam energy to 12 GHz RF power and finally act as a test bench for the decelerator beam-based alignment schemes [12].

Chapter 2

The state of the art in longitudinal diagnostics

2.1 Longitudinal diagnostics at CTF3

A schematic diagram of the bunch length diagnostics at CTF3 is shown in figure 2.1 [13]. Several methodologies are implemented at CTF3 and they can be divided into two main subclasses: time domain methods and frequency domain methods. The time domain methods include a streak camera and an RF deflecting cavity, the frequency domain methods include an RF-pickup and a Coherent Diffraction Radiation experiment which is currently under development and will be discussed in this thesis in great detail. Now we shall concentrate on the techniques which are in everyday use.

2.1.1 Streak camera

Here we shall consider the streak cameras at CTF3. Light emitted as either Synchrotron Radiation (SR) produced in the arcs of the delay loop and combiner ring dipole magnets, or as an Optical Transition Radiation (OTR, see chapter 3, section 3.4) produced at the end of the drive beam linac is guided to the optical laboratories outside the radiation environment of the machine. In order to achieve a good time resolution in a streak camera, photons are converted into electrons and then accelerated and deflected using a time-synchronized high voltage electric field. The deflecting field converts a
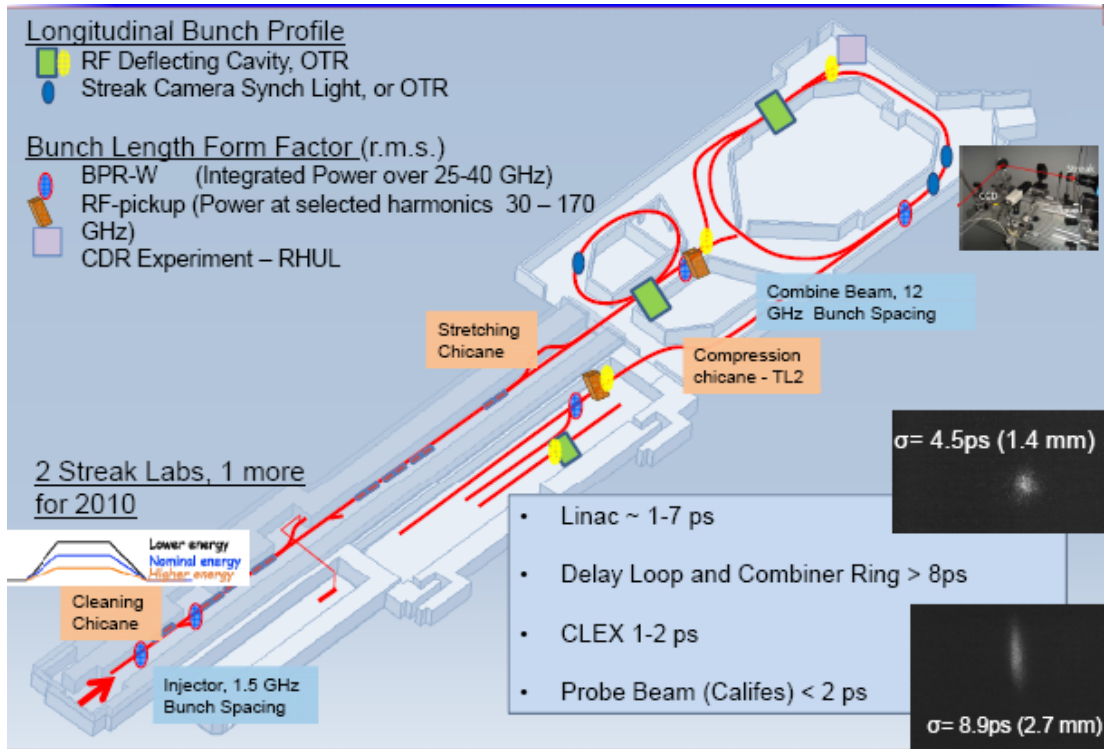
Figure 2.1: Schematic diagram of the longitudinal diagnostics at CTF3.

time information into a spatial information. The signal from the deflected electrons is amplified with a micro channel plate, then converted into photons using a phosphor screen and finally detected by a CCD array which converts light into a voltage signal (see figure 2.2) [14].

In the CTF3 streak cameras an adjustable picosecond timing delay of $\triangle_t = 10$ ps with an intrinsic jitter of less than 1 ps allows for a precise calibration of the streak cameras and the flexibility to measure individual bunches along the full pulse train. A sweep speed of 10 ps/mm is used for single bunch length measurements with a calibration of 0.122 ± 0.004 ps/pixel [15].

Figure 2.3 demonstrates the measured profiles and the corresponding σ values for bunches in the delay loop and at the end of the CTF3 linac for two different beam conditions. The measurements were performed by the authors of [14]. The highest sweep speed of 10 ps/mm was used. The measurement on the left was performed using the SR in the second quarter of the delay loop, a bunch with $\sigma = 8.9$ ps was measured. The measurement on the right was performed using the OTR detected from the TR
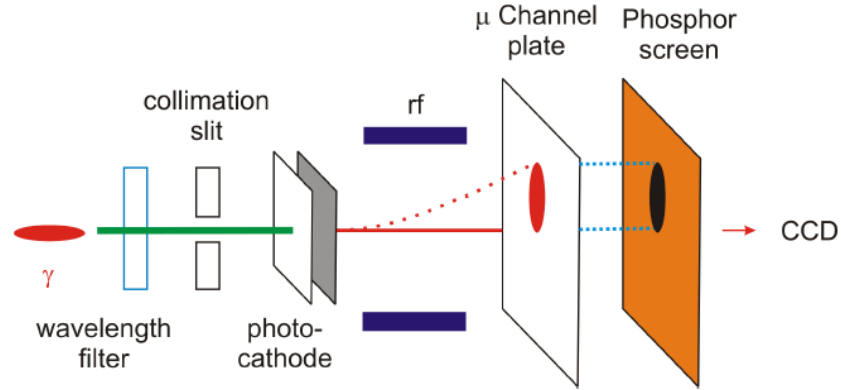
Figure 2.2: Working principle of a streak camera.

screen positioned at the end of the linac, a bunch with $\sigma = 4.5$ ps was measured.

The resolution of a streak camera is determined by the quality of the optical transport system, finite sweep speeds, photoelectron energy spread and the resolution of the CCD camera in use. The best resolution so far was achieved by the Hamamatsu FESCA-200 streak camera with a resolution of 200 fs [16]. The usage of SR in a streak camera makes this diagnostics non-destructive, however in straight sections of an accelerator TR screens have to be used and therefore the diagnostic becomes destructive.
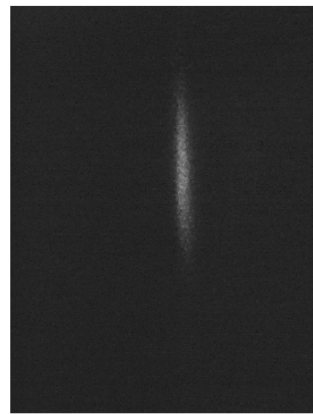
Synchrotron radiation from MTV0361.
Measured $\sigma = 8.9$ ps.
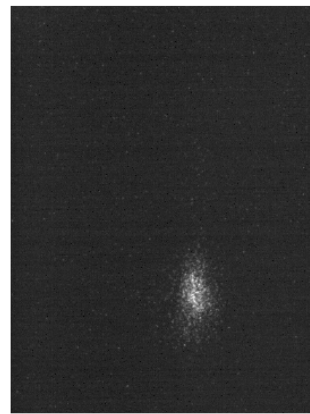
Optical transition radiation from MTV0550.
Measured $\sigma = 4.5$ ps.

Figure 2.3: The single-bunch longitudinal beam profiles measured by the streak cameras in the delay loop and the transfer line 1.

2.1.2 RF deflector

Bunch length measurements can also be performed using the 1.5 GHz transverse RF deflector at the entrance to the delay loop and the OTR screen installed downstream of the RF deflector. As bunches pass through the deflector, they induce a field which has a strong correlation between the particles longitudinal position in the bunch and the transverse position after the kick produced by the deflector. The measurement of the transverse beam profile after the kick gives the direct information about the bunch length.

During measurements the beam bypasses the delay loop. The RF deflector is phased in such a way that the beam arrives close to the RF zero crossing. In this configuration the head and the tail of each bunch are kicked in opposite directions (see figure 2.4(a)) and the images from the odd and even bunches fully overlap. In order to distinguish between the odd and even bunches, the phase of the RF deflector is set to be slightly off zero crossing to image two beam spots separately on one screen (see figure 2.4(b)) [17].

Once the beam spots are separated a horizontal corrector magnet is used in order to move one beam spot to the centre of the screen, which is done for maximisation of the light collection from the optical line. Two quadratic r.m.s. dimensions measured when the RF deflector is on and when the RF deflector is off are subtracted to calculate the bunch length [18]:

$$\sigma_{z_{r.m.s.}} = \frac{1}{CAL} \sqrt{\sigma^2_{x_{r.m.s.}(RFon)} - \sigma^2_{x_{r.m.s.}(RFoff)}} \tag{2.1}$$

where CAL is the calibration constant which can be experimentally measured (units: mm(screen)/mm(longitudinal)). Using this formula the bunch length can be approximated. A resolution of 15 fs which is the best resolution for this technique so far was achieved by the LOLA cavity at SLAC [19]. In the context of CLIC the usage of RF deflectors is limited due to the destructiveness of this technique and the extensive infrastructure requirements, i.e. a significant beam-line space is required as for example the LOLA cavity is 3.6 m long and also installation of a TR screen is needed.
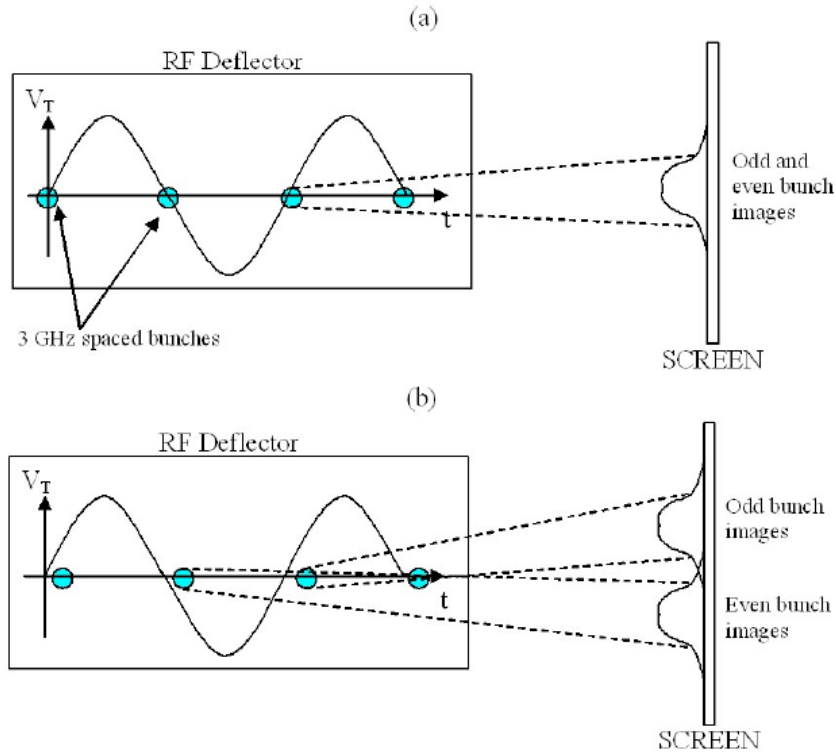
Figure 2.4: Schematic view of the RF deflector influence on the bunches at the zero-crossing (a) and slightly off the zero crossing (b).

2.1.3 RF pickup

Another technique used at CTF3 for a bunch length estimation is an RF pickup (see figure 2.5) [20]. The RF pickup detection system is designed to measure the amplitude of the RF signals from the beam simultaneously in four frequency bands: 26.5 - 40 GHz, 45 - 69 GHz, 75 - 90 GHz and 142 - 170 GHz. The frequencies above a cut-off of 21.1 GHz are transported in the waveguides to the detection station where they are emitted by horn antennas.

As shown in figure 2.5 two down-mixing stages are required to measure high frequency RF signals. The first stage has a fixed local oscillator frequency for each band, namely 26.5 GHz, 56.5 GHz, 75 GHz and 157 GHz. The second down mixing stage is common for each two of the four detection bands, it uses two synthesizers with a variable frequency range from 2 to 14 GHz. The measurements of the beam harmonics of 30 GHz, 33 GHz, 36 GHz and 39 GHz are performed using K-band detection, the
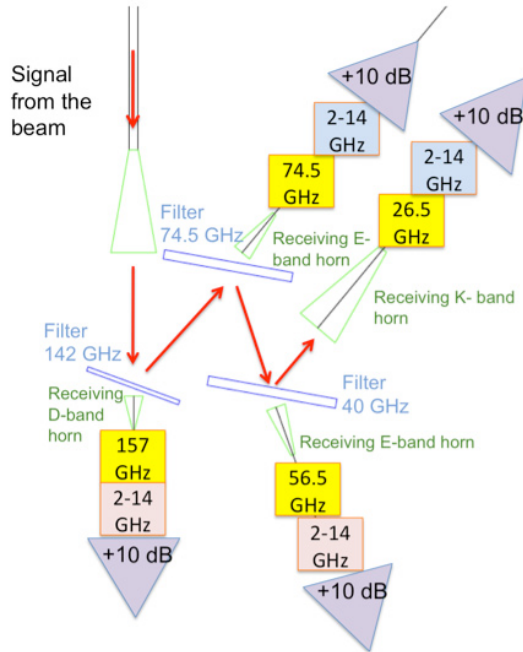
Figure 2.5: Schematic layout of RF pickup detection system.

beam harmonics of 60 GHz, 63 GHz, 66 GHz and 69 GHz are measured using the E-band detection stage and the beam harmonics of 78 GHz, 81 GHz, 84 GHz and 87 GHz are measured with the E-band detection stage. The D-band detection stage provides signals only for very short beams. The signals are amplified by +10 dB after the second downmixing stage.

For each machine condition corresponding to a particular phase setting of the last klystron in the linac, the mean height of the peak corresponding to each beam harmonic is measured and used for the bunch length determination. The amplitude of each beam frequency is measured as a function of the klystron phase and then used in the fitting procedure to extract the bunch length. The longitudinal distribution of electrons in the bunch is assumed to be a single Gaussian. Sub-ps time resolution can be achieved using this technique, however its main disadvantage is usage of an a-priori known charge distribution in data analysis.

2.2 Electro-optic and Coherent Radiation techniques

For CLIC it is essential to achieve a longitudinal diagnostic resolution of ~ 20 fs. The diagnostic has to be non-invasive and robust. Well developed beam diagnostic tools such as a streak camera and an RF deflector cannot be used due to their invasiveness.

One of the alternatives to the diagnostics described above is a coherent radiation (CR) technique. It is based on emission of beam induced radiation from screens of different geometries. Depending on the design of the screen and the type of radiative process, the technique can be destructive or non-destructive. The main advantage of the CR method is absence of the intrinsic theoretical resolution limit on the bunch shape that can be reconstructed.

An electro-optic (EO) technique is another methodology for longitudinal bunch profiling. It enables characterisation of the beam longitudinal characteristics in the time domain. It is based on the direct measurement of the Coulomb field of a charged particle or alternatively a certain radiative process, e.g Coherent Transition Radiation or Coherent Diffraction Radiation (see chapter 3).

The electro-optic method measures the birefringence induced by the transient Coulomb field moving past a non-linear optical crystal, such as ZnTe or GaP. Refractive index of these crystals depends linearly on the electric field of the THz radiation. A polarised laser pulse experiences a phase retardation depending on the electric field strength and the crystal thickness. The induced phase retardation can be measured with a polariser-analyser pair [21].

A 60 fs resolution using EO technique was achieved at the soft x-ray free-electron laser at FLASH where the EO signals were observed using a gallium-phosphide (GaP) crystal. This resolution was very close to the physical limit imposed by the crystal properties [22]. In the experiment performed by A.D. Debus the duration of laser-wakefield accelerated bunches was measured by a ZnTe-based electro optic setup and a 45 fs laser [23]. The knowledge of the electron energy spectrum and the geometry of the CTR source used in the experiment allowed to partially overcome the resolution limit of the crystal and infer an electron bunch duration below 38 fs. At the moment applicability of EO technique is mainly limited by the EO material properties and the

stability of a laser with a very short pulse duration.

Chapter 3

Coherent Radiation techniques

3.1 Coherent Radiation

The physical origin of Coherent Radiation (CR), historical aspects of bunch length measurements using CR based techniques, existing methodologies and challenges for future accelerator diagnostics will be discussed in this chapter.

There is a variety of physical effects which can occur as the result of interaction between a charge particle and a target positioned at a distance from the charge or on its way, and due to the particle trajectory bending in the magnetic field. In this chapter four effects will be discussed: Synchrotron Radiation (SR), Transition Radiation (TR), Diffraction Radiation (DR) and Smith-Purcell Radiation (SPR). CR is produced when a wavelength of radiation emitted by any of the mentioned processes is comparable to or larger than a bunch length.

A graphical illustration of coherency and incoherency of radiation is presented in figures 3.1 and 3.2 [24].
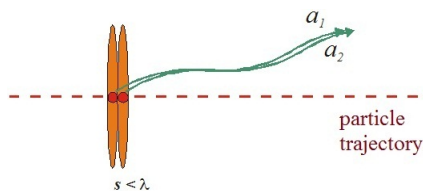
Figure 3.1: Coherent radiation generation from the two electrons.
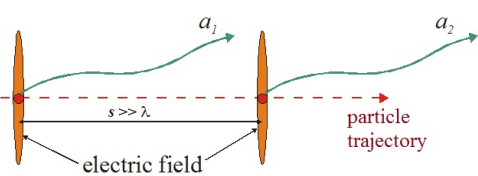
Figure 3.2: Incoherent radiation generation from the two electrons.

Consider two electrons emitting radiation (any type can be discussed). Figures 3.1 and 3.2 are simplified and there is no radiative medium in the pictures, a_1 and a_2 are the electric field amplitudes. When the distance between the electrons is comparable to or smaller than the radiation wavelength, i.e. the electrons radiate in phase, the intensity of the radiation at the observation plane is defined as a sum of the amplitudes:

$$I_{coherent} = |a_1 + a_2|^2 = |2a|^2 = 4|a|^2. \tag{3.1}$$

Extrapolating this case to N electrons:

$$I_{coherent} = |a_1 + a_2 + ... + a_N|^2 = N^2|a|^2. \tag{3.2}$$

When the distance between the electrons is much larger than the radiation wavelength, so they are not in phase any more, the radiation intensity can be written as:

$$I_{incoherent} = |a_1|^2 + |a_2|^2 = 2|a|^2. \tag{3.3}$$

and in the case of N electrons $I_{incoherent} = N|a|^2$.

The spectrum of the radiation generated by the bunch of charged particles can be expressed as follows [25]:

$$S_{tot}(\omega) = S_p \left[N_p + N_p(N_p - 1)F(\omega) \right], \tag{3.4}$$

where S_p is the single particle spectrum, which depends on the radiation frequency and the observation angles or spatial coordinates, N_p is the number of particles in the bunch, $F(\omega)$ is the amplitude of the longitudinal bunch form factor. The part of the sum proportional to N_p corresponds to the incoherent part of the spectrum, the second part which is proportional to $N_p(N_p - 1)$ describes the coherent part of the spectrum. When CR is produced the radiation intensity is enhanced by $\sim N_p$, compared to incoherent radiation. If a bunch consists, for example, of 10^{10} particles one should expect an intense photon flux with a certain spectrum which can be used for variety of applications, including beam diagnostics.

In equation (3.4) only the longitudinal component of the form factor is considered

which comes from the fact that for $\lambda \gg 2\pi\sigma_0 \sin\theta$, where σ_0 is the transverse dimension of the beam and θ is the radiation emission angle, the transverse component of the form factor behaves as a constant close to unity [26]. In the relativistic case $\sin\theta \sim 1/\gamma$ where γ is the Lorentz factor. For CTF3 $\sigma_0 \simeq 1$ mm and the beam energy $\gamma = 235$. This results in the condition that for $\lambda \gg 2\pi\sigma_0/\gamma = 0.03$ mm the transverse form factor may be considered as unity. For wavelengths in the mm region this condition is fulfilled and therefore equation (3.4) is valid for the calculation of the longitudinal form factor.

The amplitude of the form factor $F(\omega)$ can be obtained as a modulus squared of a Fourier transform applied to the longitudinal charge distribution $\rho(z)$ in the bunch [25]:

$$F(\omega) = \left| \int_0^\infty \rho(z) exp\left(i\frac{\omega}{c}z\right) dz \right|^2, \tag{3.5}$$

In order to understand the form factor geometry one may consider the Gaussian bunch with the length σ_z. The expression for $F(\omega)$ can be calculated in the analytical form:

$$F(\omega) = \left| \frac{1}{\sqrt{2\pi}\sigma_z} \int_{-\infty}^\infty exp\left(-\frac{z^2}{2\sigma_z^2}\right) exp\left(i\frac{\omega}{c}z\right) dz \right|^2$$

$$= exp\left(-\frac{\omega^2\sigma_z^2}{c^2}\right) = exp\left(-k^2\sigma_z^2\right), \tag{3.6}$$

where $k = 2\pi/\lambda$ is the wavenumber. Equation (3.6) was calculated using the following integral from the tables of integrals [27]:

$$I(a,b) = \int_{-\infty}^\infty exp(-ax^2)exp(bx)dx = exp\left(\frac{b^2}{4a}\right)\sqrt{\frac{\pi}{a}}, \tag{3.7}$$

where $a = 1/2\sigma_z^2$ and $b = \sqrt{i\omega/c}$.

Figure 3.3 demonstrates the form factors calculated for three different bunch lengths: one, two and three millimetres, and a bunch population of 10^{10} particles. A logarithmic scale was chosen to demonstrate a level of incoherent radiation at $log(S(\omega)/S_p(\omega)) = 10^{10}$. The vertical dashed lines indicate the wavelengths equal to the corresponding bunch lengths, it is clear that the coherency of radiation arises when the radiation wavelength is larger than the bunch length and consequently the form factor amplitude

significantly increases.
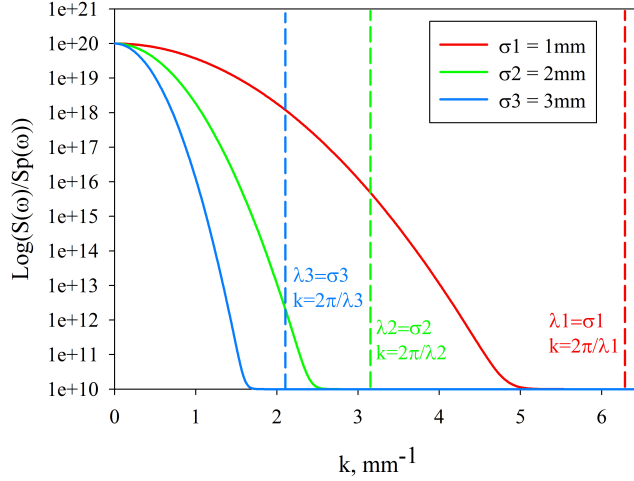
Figure 3.3: Form factor amplitudes calculated for three different bunch lengths: 1 mm, 2 mm and 3 mm.

From equation 3.4 the coherent part of the radiation spectrum can be expressed as follows:

$$S_{coh}(\omega) = N_p^2 S_p(\omega) F(\omega). \tag{3.8}$$

Over twenty years after the first observation of CR a significant progress was made in understanding of its physical origin and practical use. The CR mechanism is the same for leptons and hadrons, however bunch length diagnostics based on the CR are used for short (typically not longer than tens of picosecond) electron and positron bunches. The main limiting factor for the CR diagnostics of long bunches is the increase of the radiation wavelength and shielding of the emitted radiation by surrounding hardware.

From equation (3.4) one may see that the coherent and incoherent parts of the spectrum differ by the factor $(N_p - 1)$, which is a significant difference when a large number of particles in the bunch is considered. For this reason experiment-wise we are interested in measuring the coherent spectrum of radiation. The basic principle of CR diagnostics establishes a relation between a radiation emission spectrum and a single electron spectrum. Once a frequency dependence of the radiation intensity has been

obtained over a significant spectral range, there is a possibility to apply, for example, Kramers-Kronig analysis (see chapter 5, section 5.3). It is used to recover the phase information of electrons in the bunch and the bunch shape. This technique was specifically developed to reconstruct fine structures of a bunch based on the knowledge of a radiation spectrum over a broad frequency range, which inevitably brings a technical challenge of measuring such a spectrum. Nevertheless, in order to provide an accurate bunch profile reconstruction, one may consider using extrapolation functions towards larger and smaller frequencies. This possibility will be discussed in chapter 5.3.

Diagnostics based on CR are usually low-cost and may operate in a wide range of bunch lengths and charges. This method allows to measure very short bunches with the lengths in the femtosecond region. The shorter the bunches one wants to characterise the shorter wavelengths have to be measured.

Currently CR based diagnostics are not fully robust as bunch profile reconstruction from a spectral measurement is not an easy task. It is more straightforward if one already has an a - priori information about the bunch length, in this case conventional methods of bunch length calculation can be applied. For example one may use an a priori known spectrum of a gaussian or a multi-gaussian bunch and compare it with a measured spectrum, but this methodology will not give exact information about the fine structure and asymmetries in the bunch.

3.2 Synchrotron Radiation

A Synchrotron Radiation (SR) appears when a charged particle beam is bent in a magnetic field. The power generated by the particle with the energy γ moving along the curvature of the radius ρ can be expressed by the following formula [25]:

$$P_\gamma = \frac{1}{6\pi\varepsilon_0} \frac{q^2 c}{\rho^2} \gamma^4, \tag{3.9}$$

where q is the charge of the particle, ε_0 is the vacuum permittivity and c is the speed of light. The power is proportional to the fourth power of the particle energy and inversely proportional to the second power of the bending radius, therefore the larger the energy of the particle and the smaller the radius the more SR radiation is

generated. An intense coherent SR (CSR) can be produced in the far-infrared and THz regions in storage rings where short bunches are circulating.

The first theoretical description of the CSR from electron bunches was made by J.S. Nodvick and D.S. Saxon [25]. The authors showed that if the wavelength of CSR is comparable to or larger than the bunch length, than the radiation intensity demonstrates a square dependence on the beam current. In 1989 CSR was observed for the first time by T. Nakazato et al. [28].

3.2.1 CSR in beam diagnostics

The CSR generated in a bending magnet in a circular accelerator may be used for beam diagnostics. One of the experimental investigations of the CSR as a tool for longitudinal beam diagnostics was performed in [29]. A longitudinal bunch profile was characterized by measuring the CSR spectrum with a Martin-Puplett interferometer. The experiment was performed at the linac-driven Vacuum Ultraviolet Free Electron Laser (VUV-FEL) at DESY, which was producing short pulses of intense soft X-ray radiation. The Kramers-Kronig relation was used for the reconstruction of the longitudinal bunch profile. The resolution of the technique was identified as 140 fs and was limited by the absorption edge of the quartz window that was used for the radiation transfer towards the detection system.

In circular machines SR is generated "naturally" and there is no need for insertion devices to detect it. However, the CSR spectrum is rather difficult to predict as it might be distorted while propagating in a vacuum chamber. It is also practically impossible to extract the CSR from coherent backgrounds such as wakefields and coherent Diffraction Radiation generated from various components of an accelerator.

3.3 Transition Radiation

Transition Radiation (TR) is produced by the passage of charged particles through the interface between media with different dielectric constants. It is caused by the collective response of the matter surrounding the particle trajectory to readjust to the electromagnetic field of the charged particle. It was first considered by Frank

and Ginzburg [30] and has been studied both theoretically and experimentally very extensively in recent decades.

For a particle with charge q passing through the interface between a perfect conductor and vacuum the angular distribution of the spectral energy can be expressed as [30]:

$$\frac{d^2W_{TR}}{d\omega d\Omega} = \frac{\beta^2 q^2}{\pi^2 c} \frac{sin^2\theta}{(1 - \beta^2 cos^2\theta)^2},$$ (3.10)

where θ is the angle between the electron trajectory and the emitted radiation, ω is the angular frequency of the radiation, c is the speed of light, $\beta = v/c$ where v is the electron velocity. For relativistic electrons ($\beta \sim 1$) the emission is sharply peaked in the region of small θ and shows a maximum for $\theta \sim 1/\gamma$, where γ is the Lorentz factor.

In figure 3.4 a schematic layout of the TR generation from the target is shown [24]. The electron with the field confined withing the region $\sim \gamma\lambda$ is moving towards the target tilted by 45 degrees with respect to the particle propagation direction. When the particle traverses the target, the TR is generated in two main directions: the direction of the particle initial propagation, forward Transition Radiation (FTR), and the direction of the specular reflection from the target, backward Transition Radiation (BTR). The radiation is confined within narrow cones with the opening angle $\theta \sim 1/\gamma$.
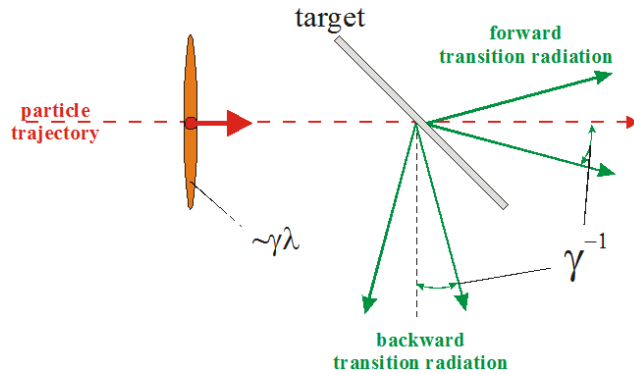
Figure 3.4: Scheme of Transition Radiation generation from the target.

In 1991 U. Happek et al. observed coherent Transition Radiation (CTR) generated by the passage of mm-long bunches of electrons through a thin metallic foil. The radiation was observed in the far-infrared part of the spectrum. The beam was produced

by the 300 MeV linac of the Cornell Electron Storage Ring [31]. The intensity, the polarisation, the spectral and angular distributions of CTR were measured and its coherent nature was identified.

3.3.1 CTR in beam diagnostics

CTR is another physical effect that can be used for beam diagnostic purposes. The first measurements of a bunch length using CTR were made by two different groups in 1994 [32, 33]. The techniques were based on the precise measurements of the CTR spectrum. Nowadays the CTR technique is widely used as a transverse and longitudinal beam diagnostic tool in many machines, its main advantages are an instantaneous emission and large emission angles achieved by rotation of a screen. The main disadvantage of using TR is its invasiveness to a machine operation.

In all coherent radiation techniques the detected radiation has a polychromatic angular (spatial) distribution. In order to measure the radiation spectrum a precise spectrometer operating in a wide frequency band is required. In [34] Wesch with colleagues developed a multi-channel THz and infrared spectrometer for femtosecond single-shot electron bunch diagnostics using CTR. The spectrometer was equipped with five consecutive dispersion gratings and 120 parallel readout channels, it could be operated in short wavelengths mode (5 - 44 μm) as well as in long wavelengths mode (45 - 430 μm).

3.4 Diffraction Radiation

Now we shall discuss Diffraction Radiation (DR). This phenomenon occurs when a charged particle moves in the vicinity of a target and causes a dynamic polarisation of the target material. For relativistic particles the methodology of the DR calculation is based on Huygen's principle of plane wave diffraction. Approximate calculations for diffraction problems are valid when the wavelength λ incident on an obstruction is small in comparison with the characteristic dimension a of the obstruction and the deflection angles from the initial direction of propagation are small [35]:

$$\lambda \ll a, \tag{3.11}$$

$$\theta \ll 1. \tag{3.12}$$

As long as the radiation process can be considered as the process of the virtual photons reflection, the conditions (3.11) and (3.12) have to be maintained. The application of the Huygens principle to the calculation of DR has some peculiarities, because unlike a plane electromagnetic wave a particle field depends on the distance from the particle trajectory.

Consider the field of a fast moving charged particle at a point $\mathbf{r}(vt, \rho)$, where ρ is the distance from the trajectory and vt is the distance along the trajectory. The transverse component of the field can be expresses as [35]:

$$E_\perp = \gamma \frac{q\rho}{(\rho^2 + v^2 t^2 \gamma^2)^{3/2}}, \tag{3.13}$$

and for relativistic particles:

$$E_\parallel \ll E_\perp, \tag{3.14}$$

$$\beta = \frac{v}{c} \simeq 1. \tag{3.15}$$

If the Fourier component of $E_\perp$ is examined over time it is seen that $E_{\perp\omega}$ is becoming small at $\rho > \lambda\gamma$, which means that the Fourier components of the particle field are spatially limited in the circle of the radius $\rho \sim \lambda\gamma$. One may conclude that the charged particle is able to feel the obstruction only if $a \leq \lambda\gamma$, otherwise the radiation is suppressed [35].
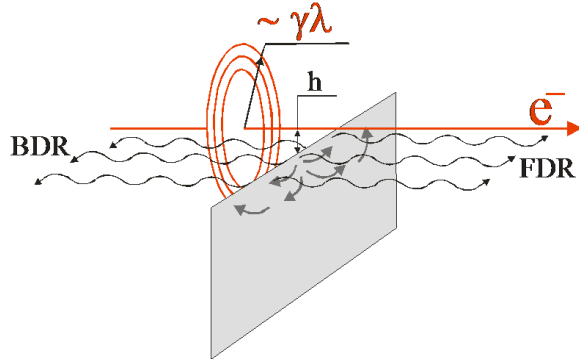
Figure 3.5: Scheme of Diffraction Radiation generation from the target.

Figure 3.5 demonstrates a schematic layout of the DR generation from a target of finite dimensions [24]. The charge moves at a distance h from the target (impact parameter). In order to generate the DR, the impact parameter should satisfy the condition $h < \lambda\gamma$. When the Coulomb field of the particle interacts with the target material, the surface currents are produced which become the source of DR. The radiation propagates in two main directions: forward direction, and backward direction or direction of specular reflection from the target. The forward direction corresponds to forward DR (FDR), the direction of specular reflection corresponds to backward DR (BDR).
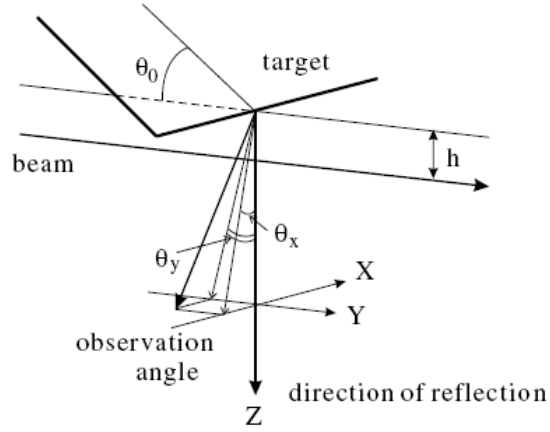
Figure 3.6: Geometry of BDR near a semi-infinite screen.

An analytical expression for BDR produced from a semi-infinite screen was derived in [36]. When a charged particle travels in the vicinity of a semi-infinite plane at an incident angle of 45 deg., the BDR is emitted at 90 deg. from the particle trajectory. In the case of a relativistic electron the angular distribution of BDR is given by:

$$\frac{d^2W_{DR}}{d\omega d\Omega} = \frac{\alpha}{4\pi^2} exp\left(-\frac{\omega}{\omega_c}\sqrt{1+\gamma^2\Theta_x^2}\right)\frac{\gamma^{-2}+2\Theta_x^2}{(\gamma^2+\Theta_x^2)(\gamma^{-2}+\Theta_x^2+\Theta_y^2)}, \qquad (3.16)$$

where α is the fine structure constant; $\omega_c = \gamma\beta c/2h$ where h is the shortest distance between the particle and the target edge (impact parameter) and c is the speed of light, β is the particle velocity in terms of the speed of light and γ is the Lorentz

factor; Θ_x and Θ_y are the radiation emission angles shown in figure 3.6 [37]. The exponential dependence of DR on the impact parameter and the wavelength of radiation is a characteristic feature of this radiative process.

The DR can be generated by the passage of charged particles through the screens of various geometries, most well studied include a slit between screens and a circular hole in a screen. In this thesis the CDR from two targets positioned one after another to one side of an electron beam will be calculated in chapter 4.1.

The CDR as a tool for beam diagnostics has all the advantages of well studied CTR, but most importantly the diagnostics based on CDR are non-invasive.

3.4.1 Experimental observations of ODR

In the experiment carried out by I.E. Vnukov et. al. [38] the properties of optical Diffraction Radiation (ODR) were investigated. A schematic layout of the experimental setup is shown in figure 3.7.
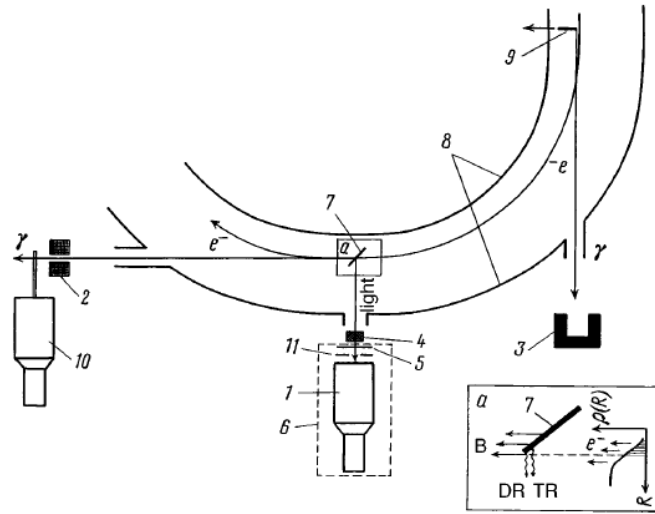
Figure 3.7: Experimental setup at the Tomsk synchrotron: 1 Photomultiplier, 2,11 collimators, 3 graveyard, 4 mirror, 5 light filter, 6 detection system, 7 target, 8 accelerator chamber, 9 scraper, 10 scintillation counter.

The experiment was performed using the 200 MeV electron beam of the Tomsk synchrotron. A 1-mm thick polished aluminium wafer (7) was used as a target. The bremsstrahlung in the forward direction was detected with a scintillator counter (10),

51
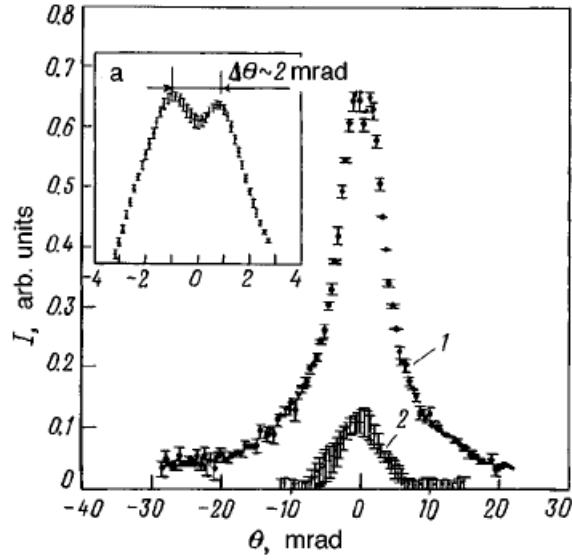
Figure 3.8: BTR and BDR from the target in the optical wavelength region. The BTR (1- the scraper is taken out from the beam pipe)and the BDR (2 - the scraper is at 1mm in the beam pipe) from the target in the optical wavelength region.

the optical radiation was measured by the detection system (6) which consisted of a photomultiplier (1), a light filter (5) and a collimator (11). A thick scraper (9) translatable in the radial direction was placed upstream of the main target (7) to cut off some part of the beam when the DR was observed. The bremsstrahlung from the scraper was dumped by an absorber (3). By covering some portion of the electron beam with the scraper, the bremsstrahlung and the TR yields were suppressed and the ODR from the target was detected.

Figure 3.8 demonstrates the orientational dependencies of the ODR intensity as a function of the target rotation for different positions of the scraper [38]. The angle $\theta = 0$ corresponds to the specular reflection of the radiation from the target. The curve 1 was measured with the scraper removed and therefore mainly the TR was contributing in the distribution of the optical radiation. Despite the large divergence of the beam one can see a dual mode shape of the very top of the peak, which is typical for TR ($\triangle\theta \sim \gamma^{-1} = 2.5mrad$). The curve 2 was measured when the large portion of electrons in the beam was cut off by the scraper and did not reach the main target. The ODR made a substantial contribution in the measured distribution, which demonstrated an

uni-modal shape and was in agreement with the theoretical calculations in [36].
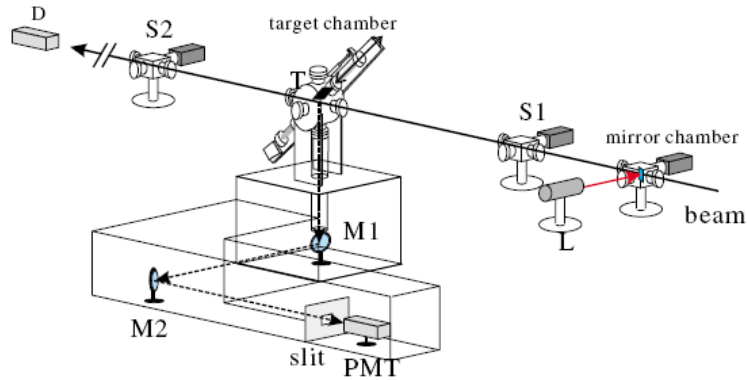
Figure 3.9: ODR setup at ATF-KEK: T: target; L: alignment laser; S1,S2: screen monitors; M1: rotatable mirror; M2: fixed mirror; D: Cherenkov counter.
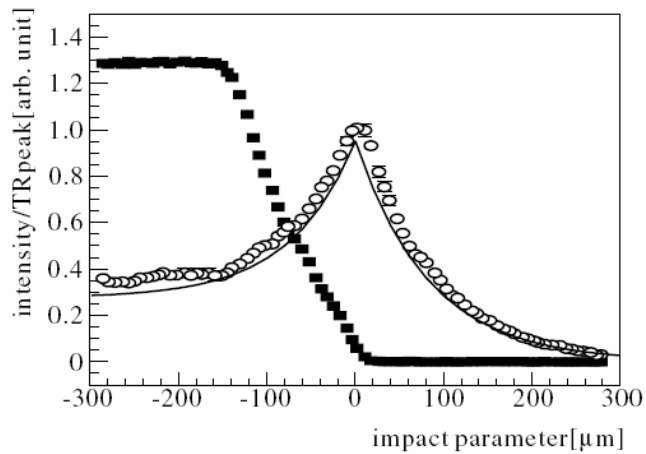
Figure 3.10: Impact parameter dependence of the intensities. The black squares: the γ ray intensity; the blank circles: the relative light yield; solid curve: the theoretical dependence.

In [37] the properties of the ODR from a single edge target were studied using the experimental setup at the Accelerator Test Facility at KEK, Japan. A schematic diagram of the set-up is shown in figure 3.9 [37]. The target (300 μm thick silicon wafer coated with aluminium) was positioned at 45 degrees with respect to the beam propagation direction and at a certain distance (impact parameter) from the beam. Light from the target was directed through the system of mirrors towards the PMT detector

with the spectral response from 300 to 650 nm. A slit with adjustable horizontal and vertical sizes was positioned in front of the detector. The beam was operated in a single bunch mode at 1.28 GeV and with 1.56 Hz repetition frequency.

In the experiment the light yield was measured as a function of the impact parameter at the mirror reflection angle from the target. The obtained result is shown in figure 3.10 where the light yield was normalised by the optical Transition Radiation (OTR) intensity. The black squares correspond to γ rays produced via Bremsstrahlung when the beam was hitting the target. The blank circles show the relative light yield as a function of the impact parameter. For the positive values of the impact parameter the ODR is produced. The solid curve in figure 3.10 is a theoretical curve derived from the theory developed in [36]. This theory allowed for calculation of both ODR and OTR yields taking into account the edge effect for the OTR.

The authors confirmed that ODR was detected when the beam did not hit the target. The impact parameter dependence of the light yield was consistent with the theoretical calculations. It was concluded that ODR was detected from the single edge target.

3.4.2 Experimental observations of CDR

The first experimental investigations of CDR were performed earlier in 1995 [39] by Shibata et al. Using a 150 MeV electron beam, the CDR was generated by a circular aperture in the millimetre and submillimetre wavelength regions.

A schematic layout of the experimental setup is shown in figure 3.11 [40]. The beam was moving through the center of the circular aperture in the disk covered with an aluminium foil. The radiation was emitted from the aperture and reflected by the mirror M1 towards the mirror M2 which was positioned 40 mm below the electron trajectory, then it was directed through the quartz window W towards a grating type far-infrared spectrometer with the wavelength response from 0.1 to 5mm. The radiation was detected at the angles θ (-9.2°, 9.2°) by a liquid Helium cooled Si bolometer.

In the experiment the angular distributions of the superposition of the forward CDR from the radiator S and the backward CTR emitted from the mirror M1 were measured for different apertures of the radiator S. The superposition of the CTR from the foil
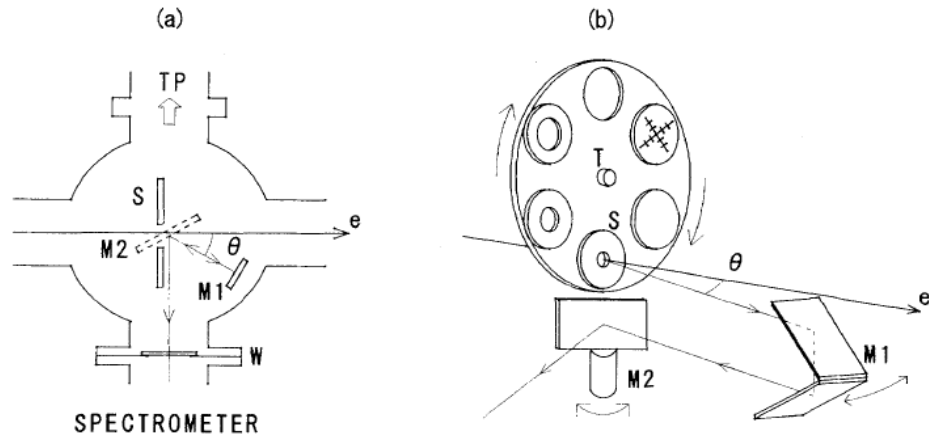
Figure 3.11: Scheme of the experimental setup: (a) top view, (b) bird's eye view. S is the radiator, M1 is the reflector, M2 is the mirror, W is the quartz window, T is the disk with circular apertures in it.

without an aperture and the backward CTR from the radiator S was also measured to identify the limiting case of the CDR when the diameter of the aperture is negligibly small. The radiation intensity was modulated as a function of the aperture size and the experimental results demonstrated a qualitative agreement with the theoretical calculations.

The spectrum of the forward CDR from a 10 mm aperture at $\theta = 0$ was obtained and the quadratic proportionality of the radiation intensity to the beam current was confirmed. The bunch form factor was calculated from the observed spectrum (see figure 3.12(a)) [40]. The values of the form factor range over three orders of magnitude, in the mm wavelengths region it is distributed irregularly around the value of unity, but according to the theory at large wavelengths it has to converge to unity. There is also a small peak at $\lambda = 0.15$ mm. The charge distribution and the phase of electrons in the bunch were reconstructed using the Kramers-Kronig technique. In order to apply this technique to the experimental data, the measured form factor was modified. The irregularities were replaced with the extrapolated lines in the regions of $\lambda > 1mm$ and $\lambda < 0.15mm$ (dashed line in figure 3.12(a)).

The reconstructions of the bunch profile are shown in figure 3.12(b). The solid profile corresponds to the form factor extrapolated toward large wavelengths only. The
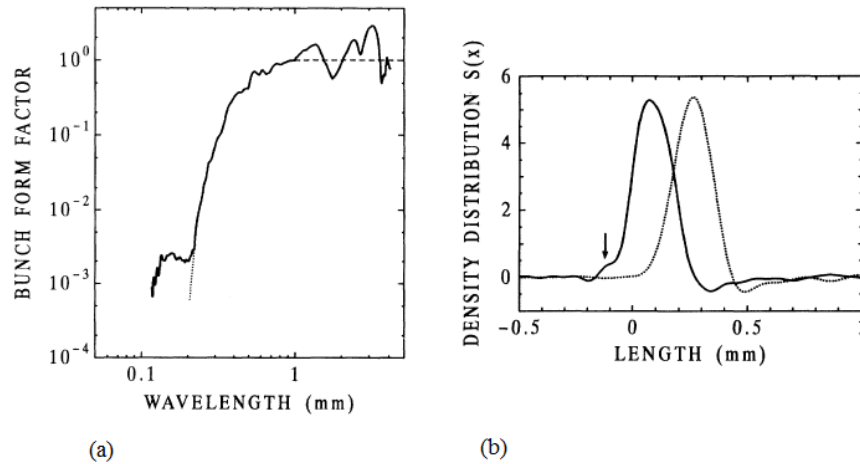
Figure 3.12: Longitudinal bunch profile reconstruction.(a) The bunch form factor, reconstructed from the measured spectrum. The dotted line is the extrapolation to be used in the Kramers-Kronig analysis. (b) The longitudinal bunch profile. The dotted curve is the longitudinal profile, when the small peak at $\lambda = 0.15mm$ in the from factor is ignored.

dotted profile corresponds to the form factor extrapolated to both large and small wavelengths. The distributions are approximated well by a Gaussian with a FWHM width of 0.2 mm. The spatial resolution was estimated from the bump structure (marked with an arrow in figure 3.12(b)) as 0.1mm, i.e. the temporal resolution is 0.3 ps. The resolution is roughly equal to the shortest wavelength of the observed spectrum. It was confirmed that the presented measurement agreed well with the measurements performed using CSR [41] and CTR [42].

In [43] by Castellano et al. measurements of CDR from a slit of variable width were performed in the millimetre and sub-millimetre wavelength ranges for short electron bunches. The experiment was performed at the TESLA Test Facility super-conducting linac operating in a single-bunch mode. The radiation was produced by 225 MeV electrons on the surface of a diffraction screen oriented at 45 deg. with respect to the beam axis and was extracted from the vacuum pipe at 90 deg. through a quartz window. Signals were analyzed by a Martin-Puplett interferometer.

A schematic diagram of the experiment is shown in figure 3.13 [43]. The DR screen was placed in the focus of a 200-mm focal length metallic parabolic mirror which con-

verted the diverging radiation fan into a nearly parallel beam. A wire grid polariser allowed for transmission of the vertical polarisation component of the radiation. The polarisation splitter split the incoming beam into two orthogonal polarisation components propagating in two different arms of the interferometer. The detectors measured the vertical and horizontal polarisation components of the radiation.
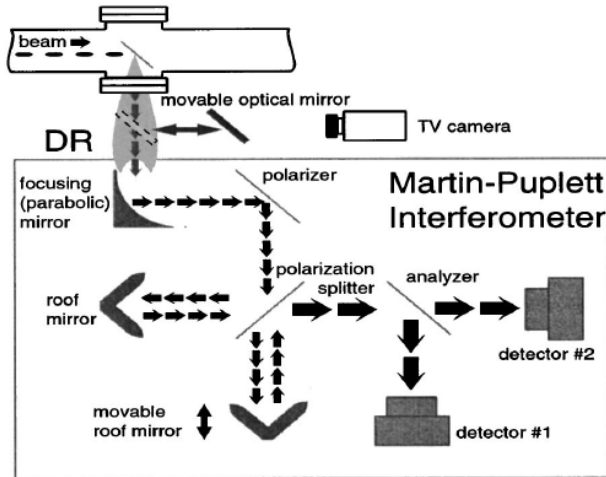
Figure 3.13: Schematic diagram of the experiment by Castellano et al. at TESLA Test Facility.

In the experiment the interferograms of two radiation polarisation components were measured by two detectors for several slit widths in the range of 0 - 10 mm. The interferograms showed a detector signal as a function of the optical path difference in two arms of Martin-Puplett interferometer. The normalised autocorrelation curves were obtained from the interferometric measurements by taking a residual of the interferograms obtained for different polarisation components and dividing it by their sum. It was done to eliminate the noise caused by the beam current fluctuations. The CDR spectra were obtained from the autocorrelation curves by performing a Fourier transform. The spectra demonstrated a weak dependence on the slit widths. The longitudinal parameters of the beam were reconstructed by fitting the autocorrelation curves with the theoretical autocorrelation functions and choosing the best fit. The bunch density distribution was assumed to be rectangular with the sides smoothed by a convolution with a Gaussian.

3.5 Smith-Purcell Radiation

Finally, we shall consider Smith-Purcell Radiation (SPR). It was predicted by Frank in 1942 [44] and Salisbury in 1949 [45], they showed that electromagnetic waves should be emitted when a charged particle is moving near a metallic diffraction grating. In 1953 Smith and Purcell experimentally showed that when an electron passes close to a metallic diffraction grating it induces a charge on the grating surface which gives rise to a radiation spatially distributed in a certain way. The fundamental wavelengths were defined by the following relation which is now called the dispersion relation for the SPR [46]:

$$\lambda = d(\beta^{-1} - \cos\theta), \tag{3.17}$$

where λ is the wavelength of the observed radiation, d is the grating period, θ is the radiation emission angle and $\beta = v/c$ is the speed of the charged particle in terms of the speed of light. The most common SPR radiator is a grating, however in recent years the Smith-Purcell radiation originating from photonic crystals and from one and two-dimensional systems of spherical macro-particles has been widely investigated [47, 48, 49].

According to the theoretical study by Toraldo di Francia [50] the intensity of SPR, U, generated as a result of the charged particle passage in the vicinity of the grating depends exponentially on the impact parameter h (the shortest distance between the particle and the grating):

$$U \sim \exp\left(-\frac{4\pi h}{\lambda\beta\gamma}\right). \tag{3.18}$$

In the case of a low energy electron beam ($\beta \ll 1$, $\gamma \simeq 1$) in order to generate SPR the beam has to travel very close to the surface of the grating, because the radiation intensity drops sharply when the impact parameter increases. It makes observation of SPR with low energy beams technically challenging. For relativistic electrons, however, (($\beta \simeq 1$, $\gamma \gg 1$)) the intensity U does not change drastically with the change of the impact parameter due to the fact that the transversal component of the particle

58

electric field is enhanced by the factor γ. This makes the use of relativistic electrons for generation of SPR more feasible.

3.5.1 Experimental observations of SPR

In 1995 Ishi et al. detected coherent Smith-Purcell radiation (CSPR) generated by the passage of short electron bunches with an energy of 42 MeV above the surface of a metallic grating [51]. The radiation was observed in the region of 0.5 to 4 mm and the intensity of SPR was proportional to the beam current squared.

The CSPR as a tool for longitudinal beam diagnostics was studied by G. Doucas et al. using 5 ps, 45 MeV electron bunches of the Free Electron Laser for Infrared Experiments (FELIX) facility in the Netherlands [52]. The authors measured the CSPR angular distribution using an array of 11 detectors over the angular range of 40° - 140° relative to the electron beam direction (see figure 3.14) [52]. The detectors were mounted outside a vacuum chamber on a support structure. Three different gratings with the periodicities of 0.5, 1.0 and 1.5 mm were used. Each period consisted of two facets, the first with a blaze angle α and the second facet perpendicular to the first one. The blaze angles were 40°, 35° and 30° respectively. The gratings were mounted on a carousel system inside the vacuum chamber.
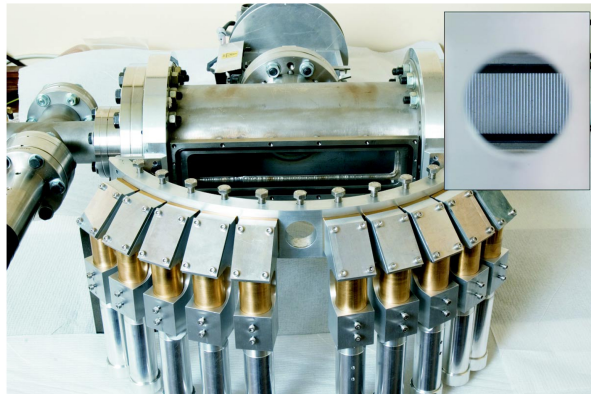
Figure 3.14: Coherent SPR diagnostic station with 11 detectors.

The bunch shape determination process was performed in several steps. The first step was the calculation of the differential energy radiated as SPR based on the knowledge of the beam and grating parameters and assumed temporal profile. The physical

basis for the calculation was a "surface current" treatment of the emission process. The energy was then averaged over the solid angle accepted by the system and after further analysis the power expected to enter the detectors at a given wavelength was calculated. Figure 3.15 shows the data points obtained using the procedure described above for all three gratings. The data have been fitted with a Gaussian and a slightly asymmetric triangular profile, the authors suggested a procedure when a Fourier transform of a number of profiles have been calculated in order to derive the expected output (SPR intensity for a given wavelength) for those profiles. The data points were derived from three different gratings. The curves in figure 3.15 are the composites created by superposition of three separate curves, one for each grating [52]. The possibility of a simple Gaussian shape was excluded, because if that was the case the power would have dropped below the detectable level at a wavelength of about 1 mm. Within the accuracy of the experiment the measured wavelength distributions was proven to be consistent with an approximately triangular profile with 90% of the bunch particles contained inside 5.5 ps.
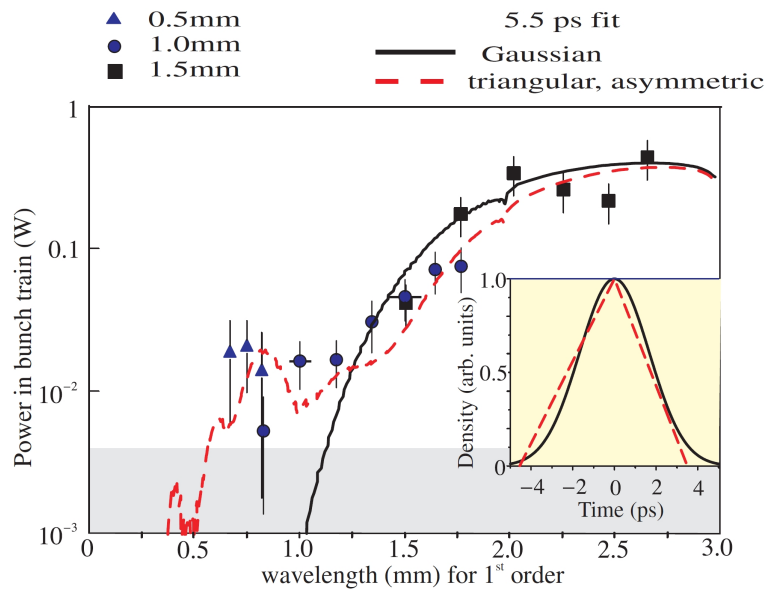
Figure 3.15: The form factor measured using three different gratings. The calculated bunch profile.

This experiment clearly showed that CSPR based diagnostics are suitable for bunch

length measurements, however the theory of SPR is not as advanced as for DR and calculation of a single electron spectrum is a challenging task. There are several theories but their predictions are rather different and for the moment there is no developed theory that explains all experiments and suitable in the wide range of electron parameters [53].

In another CSPR experiment the same group demonstrated the bunch length profiling at Stanford Linear Accelerator (SLAC) [54]. A single bunch electron beam had a repetition frequency of 10 Hz and an energy of 28.5 GeV with approximately 1×10^{10} electrons per bunch. The scheme of the experiment was similar to the one shown in figure 3.14. In the experiment the spectral measurements of CSPR for different grating periods were taken. The bunch profile reconstruction was performed using the Kramers-Kronig analysis. In both experiments no cross-checks with other diagnostics were presented, but in [54] the authors indicated that the results are close to those obtained using the LOLA cavity.

Another diagnostic technique based on CSPR is being developed at DESY (Hamburg, Germany) and Paul Scherrer Institute (Villigen, Switzerland). The main idea of the experiment is to use two detectors and an inclined grating in order to simplify the diagnostic scheme. Smith-Purcell radiation from an inclined grating is called Resonant Diffraction Radiation (RDR) and it was calculated for the first time in [55]. Later it was proposed to use coherent RDR for bunch length diagnostics [56]. The suggested scheme is shown in figure 3.16 [57].

The electron bunch travels with the impact parameter h in the vicinity of the grating. In order to minimize the contribution of the Wood-Rayleigh like anomalies, a very thin strip-grating with vacuum gaps will be used. The radiation will be measured by two detectors. While the grating is parallel to the electron trajectory both detectors measure radiation with wavelengths almost equal to the grating period according to the Smith-Purcell dispersion relation. However if the grating is inclined the radiation lines shift in the opposite directions: one detector measures longer wavelengths while the second measures shorter ones. If the grating period is chosen to be close to the coherent threshold, the line intensity measured by the detectors changes considerably while tilting the grating. Thus, by measuring the dependence of the detector signal on
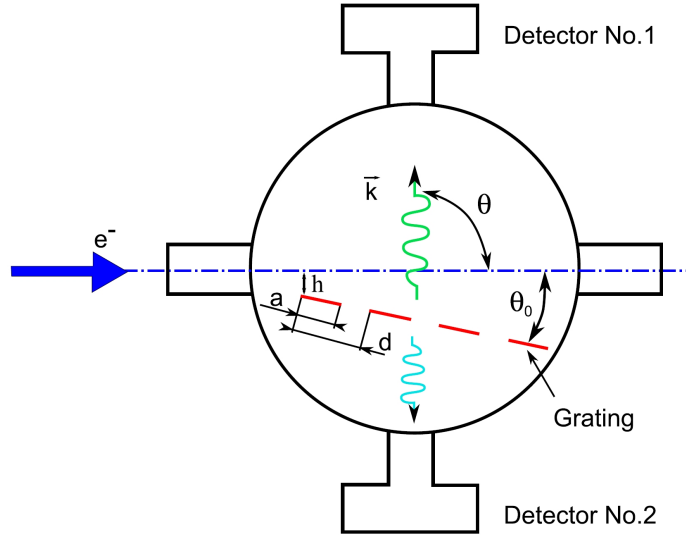
Figure 3.16: Scheme of the coherent RDR radiation generation by the inclined target.

the inclination angle, it is possible to estimate the bunch length if one has an a-priori information about the bunch profile. In the proposed scheme the accessible wavelengths are not limited by the number of detectors, therefore the number of data points available for a bunch shape reconstruction should be sufficient. The proof-of-principle experiment will be carried out in the first half of 2012 at Paul Scherrer Institute [57].

3.6 Motivation for the CDR experiment at CTF3

The monitoring and control of the longitudinal bunch profile is crucially important for the high luminosity at the CLIC IP and also for the effective power production in PETS. Therefore the development of a sufficiently fast and robust longitudinal bunch profile measurement system is essential. A low cost of the technique is also very important due to the large number of stations required for CLIC. A frequency domain technique based on the detection of Coherent Diffraction Radiation (CDR) spectrum is a promising candidate for a longitudinal diagnostic of very short bunches down to the femtosecond region.

An overview of the beam diagnostic techniques that use different types of coherent radiation was presented in chapter 3. Further in this thesis we will concentrate our

discussion only on CDR. To be more specific, the generation of the CDR from two aluminium targets positioned to one side of a beam will be investigated theoretically and experimentally. An applicability of the CDR to the longitudinal beam diagnostics will be discussed as well. The CDR is generally very advantageous for beam diagnostics due to the following reasons:

- non-invasive nature;

- large emission angles for low background measurements;

- high radiation intensity due to a quadratic dependence on a beam charge;

- instantaneous emission allows for time-resolved measurements to be performed;

- well advanced Diffraction Radiation theory based on the Classical Electrodynamics;

- no theoretical resolution limit on bunch length diagnostics.

A CDR spectrum can be used for a direct measurement of a bunch form factor and thereafter for a bunch shape reconstruction using the Kramers-Kronig analysis. In the experimental setup at CTF3 the radiation is generated from two targets positioned to one side of the beam. The main advantages of a two-target configuration are the following:

- suppression of backgrounds originating upstream of the experimental setup by the upstream target;

- the upstream target is additional source of CDR;

- possibility of multiple reflection suppression by installing an absorber in the upstream cross of the experimental setup;

- transverse kick compensation by positioning the targets at 45 deg. with respect to the beam propagation direction.

Both targets are installed at 45 deg. with respect to the beam propagation direction. By positioning the targets this way a transverse kick compensation is achieved. Imagine
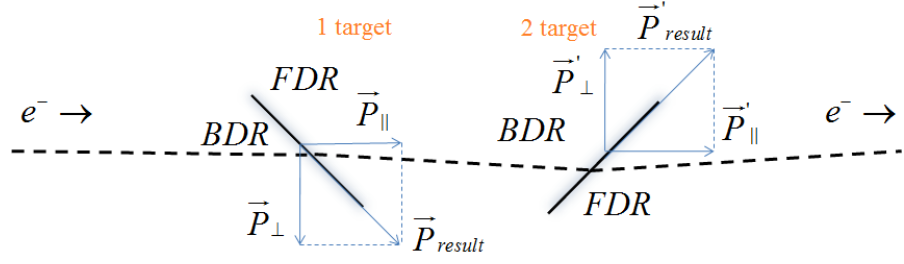
Figure 3.17: Transverse kick compensation in the dual target scheme.

that the second target only is installed in the six way cross, the FDR is produced from the downstream surface of the target and the BDR from the upstream surface. The impulse of the photons emitted from the upstream surface produces a kick onto the beam in the tarnsverse plane affecting the beam trajectory. When the first target is in the upstream cross a transverse kick onto the beam in the opposite direction is produced, as seen in figure 3.17. $\vec{P}_\perp$ is the impulse produced by the BDR emitted from the upstream surface of the first target, $\vec{P}_\parallel$ is the impulse produced by the FDR from the downstream surface of the first target and $\vec{P}_{result}$ is the resultant impulse. For the second target the corresponding values are $\vec{P}'_\perp$, $\vec{P}'_\parallel$ and $\vec{P}'_{result}$. The values of $\left|\vec{P}'_{result}\right|$ and $\left|\vec{P}_{result}\right|$ cancel out each other in the transverse plane which results in a minimal perturbation of the beam.

Chapter 4

CDR from a dual-target system

A two-target scheme shown in figure 4.1 was proposed for the generation of CDR. It required in-depth theoretical studies to investigate the properties of the radiation originating from the targets and to be able to predict a single electron spectrum required for a bunch profile reconstruction. In a theoretical model the targets are positioned in the infinite space and a beam of charged particles moves at a certain distance from them. The targets are positioned to one side of the beam and at 45 deg with respect to the beam direction of propagation, in order to compensate a transverse kick generated by the first target onto the beam. The first target serves as a barrier for the coherent backgrounds, such as CSR generated upstream of the experimental setup.

For the calculation we shall use the classical theory of Diffraction Radiation based on the Huygens principle of plane wave diffraction. The classical DR theory describes BDR only, however for a metallic foil and a millimetre wavelength range we can use an ideal conductor approximation. In this case BDR characteristics coincide with FDR ones [35]. A particle field is introduced as a superposition of its virtual photons, and when they are reflected off a target surface they are converted into the real ones and propagate either in the direction of a specular reflection (BDR) or along a particle trajectory (FDR). The main parameters used in the model are presented in table 4.1.

In the theoretical model a process of CDR generation is considered in several steps. Firstly, the emission of FDR from the first target, its propagation towards the second target, a reflection from it and propagation towards the observation plane. Secondly,

Table 4.1: CTF3 and CDR experiment parameters.

Beam energy (γ)	235	
Bunch charge	2.3	nC
Bunch spacing frequency	3	GHz
Target dimensions (projected)	40x40	mm
Observation wavelength (λ), unless stated otherwise	5	mm
First target impact parameter (h_1) (upper pos.)	30	mm
First target impact parameter (lower pos.)	10	mm
Second target impact parameter (h_2)	10	mm
Distance between the targets (d)	0.27	m
Distance from the second target to the obs. plane (a)	2	m

the emission of BDR from the second target and its propagation towards the observation plane. The first stage of the process is more complex and requires integration of the charged particle electric field over the surface of the first target taking into account propagation of the radiation between the targets, and also integration over the surface of the second target which takes into consideration a diffraction effect.
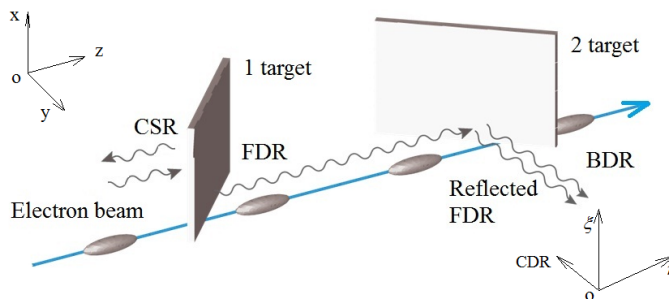
Figure 4.1: Schematic view of the Dual Target System at CTF3. FDR - Forward Diffraction Radiation; BDR - Backward Diffraction Radiation; CSR - Coherent Synchrotron Radiation.

In order to obtain the expression for the CDR at the observation plane from both targets, the expressions for the FDR from the first target and the BDR from the second target have to be combined, introducing the photon phase terms which define interference between the radiations. In the calculations that follow in this chapter the simplified geometry is used. We consider the projected width and height of the targets on the Oxy and $O\xi\eta$ planes, therefore a 45 deg. rotation angle of the targets is not

taken into account in the path length of the interfering radiation. In figure 4.1 which shows the positions of the targets in the experimental setup the targets are positioned at 45 deg. with respect to the radiation propagation direction, so for a target with a width of 60 mm and a height of 40 mm the projected dimensions will be 40 mm of width and 40 mm of height.

The major results of the model development and analysis were published in [58].

4.1 Characteristics of the CDR

4.1.1 BDR from the second target

In this subsection we discuss the radiation from the second target alone. Consider an electron moving along the z-axis. Each point of the target surface can be represented as an elementary source of radiation (see figure 4.2). Two polarisation components of the DR can be represented as a superposition of the waves from all elementary sources at a distance $\mathbf{r}_2$ from the target [35]:

$$E_{r_2}^2 = -\frac{1}{4\pi^2} \iint E'(x_2, y_2) \frac{e^{ik|\mathbf{r}_2|}}{|\mathbf{r}_2|} dx_2 dy_2, \tag{4.1}$$

$E'(x_2, y_2)$ is the amplitude of the radiation source positioned on the target surface, (x_2, y_2) are the coordinates of the radiation source on the second target surface, $|\mathbf{r}_2|$ is the distance from the radiation source to the observation point.

The amplitude $E'(x_2, y_2)$ can be represented as a Fourier transform of the incident particle field [35]:

$$
\begin{aligned}
E'(x_2, y_2) &= -\frac{ie}{2\pi^2} \iint \frac{k'_{x,y} exp\left[i(k'_x x_2 + k'_y y_2)\right]}{k_x'^2 + k_y'^2 + k^2\gamma^{-2}} dk'_x dk'_y \\
&= \frac{ek}{\pi\gamma} \frac{x_2, y_2}{\sqrt{x_2^2 + y_2^2}} K_1\left(\frac{k}{\gamma}\sqrt{x_2^2 + y_2^2}\right),
\end{aligned}
\tag{4.2}
$$

where k is the wave number, λ is the wavelength of the DR, γ is the Lorentz-factor, $k'_{x,y}$ are the components of the virtual photon wave vector, K_1 is a modified Bessel function of the first order.
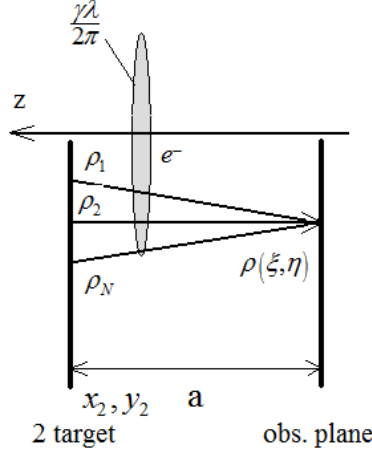
Figure 4.2: BDR generation geometry, a is the distance between the target and the observation plane, $\rho_1, \rho_2...\rho_N$ are elementary radiation sources, $\rho(\xi, \eta)$ is the resultant amplitude from all elementary sources on the observation plane.

The phase term of the photons propagating from the target to the observation plane can be written as [59]:

$$\frac{exp(ik|\mathbf{r_2}|)}{|\mathbf{r_2}|} = \frac{exp(ik\sqrt{a^2 + (x_2 - \xi)^2 + (y_2 - \eta)^2})}{\sqrt{a^2 + (x_2 - \xi)^2 + (y_2 - \eta)^2}}, \quad (4.3)$$

where a is the distance between the target and the observation plane.

ξ and η are the coordinates of the observation plane. The parameters $(\xi - x_2)/a$ and $(\eta - y_2)/a$ determine the angles of the photon emission by the elementary radiation sources. In the ultra-relativistic case they are of order of $\gamma^{-1} \ll 1$. Therefore we can apply a Fresnel approximation and the phase term of the photons propagating from the target to the observation plane can be written as [59]:

$$\frac{exp(ik|\mathbf{r_2}|)}{|\mathbf{r_2}|} \approx \frac{exp(ika)}{a} exp\left[\frac{ik}{2a}(x_2^2 + y_2^2) - \frac{ik}{a}(x_2\xi + y_2\eta) + \frac{ik}{2a}(\xi^2 + \eta^2)\right]. \quad (4.4)$$

The first term in the square brackets of equation (4.4) corresponds to the first order Fresnel correction which is used in the near field or at the distance from the source of radiation $a \leq \gamma^2\lambda/2\pi$. The second term corresponds to Fraunhofer diffraction when the distance from the radiation source is assumed to be so large ($a \gg \gamma^2\lambda/2\pi$),

that the radiation field can be considered as a superposition of the plane waves of different amplitudes emitted by each elementary source on the target. Substituting equation (4.4) and (4.2) into equation (4.1) one can obtain the expression for the two polarisation components of the DR from the second target:

$$
\begin{aligned}
E_{r_2}^2(\xi, \eta) & = -\frac{1}{4\pi^2} \frac{ek}{\pi\gamma} \frac{exp(ika)}{a} \iint \left(\frac{\frac{x_2}{\sqrt{x_2^2 + y_2^2}}}{\frac{y_2}{\sqrt{x_2^2 + y_2^2}}} \right) K_1 \left(\frac{k}{\gamma} \sqrt{x_2^2 + y_2^2} \right) \\
& \times exp \left[\frac{ik}{2a} \left((x_2 - \xi)^2 + (y_2 - \eta)^2 \right) \right] dx_2 dy_2,
\end{aligned}
\tag{4.5}
$$

where x_2 and y_2 are the coordinates on the second target surface.

The DR spatial distribution in a general form can be determined as:

$$
\frac{d^2 W^{DR}}{d\omega d\Omega} = 4\pi^2 k^2 a^2 \left(|E_x^{DR}|^2 + |E_y^{DR}|^2 \right),
\tag{4.6}
$$

where E_x^{DR} and E_y^{DR} are the horizontal and vertical polarisation components of the DR respectively.

Substituting equation (4.5) into equation (4.6) and taking into account that $e^2/\hbar c = \alpha = 1/137$, the spatial-spectral distribution of the BDR from the second target can be obtained as follows:

$$
\begin{aligned}
\frac{d^2 W^{DR}}{d\omega d\Omega} & = \frac{4}{137\lambda^4\gamma^2} \left[\iint \left(\frac{\frac{x_2}{\sqrt{x_2^2 + y_2^2}}}{\frac{y_2}{\sqrt{x_2^2 + y_2^2}}} \right) K_1 \left(\frac{k}{\gamma} \sqrt{x_2^2 + y_2^2} \right) \right. \\
& \left. \times exp \left[\frac{ik}{2a} \left((x_2 - \xi)^2 + (y_2 - \eta)^2 \right) \right] dx_2 dy_2 \right]^2.
\end{aligned}
\tag{4.7}
$$

Figure 4.3 shows the horizontal polarisation component of the CDR emitted from the second target. The distribution has a dual mode shape with the central minimum at $\eta = 0$. The vertical polarisation component of the radiation, shown in figure 4.4, has a single mode shape and the intensity of the calculated radiation is an order of magnitude larger than of the horizontal polarisation component. The shape of the final distribution is defined by the vertical polarisation of CDR (see figure 4.5).
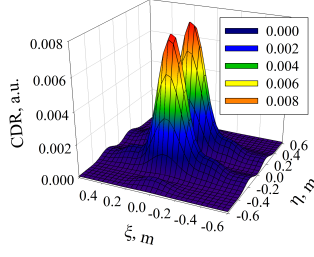
Figure 4.3: The horizontal polarisation component of the CDR from the second target, $h_2 = 10$ mm.
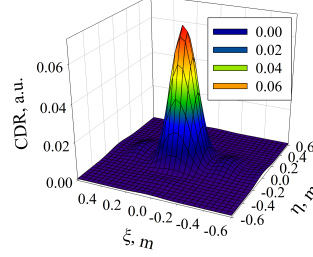
Figure 4.4: The vertical polarisation component of the CDR from the second target, $h_2 = 10$ mm.
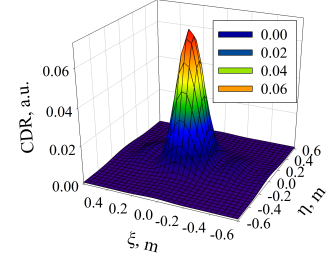
Figure 4.5: The final CDR distribution from the second target, $h_2 = 10$ mm.

The CDR maxima in figures 4.5 and 4.4 are positioned at ($\xi = 30$ mm, $\eta = 0$ mm), which corresponds to the projection of the second target centre onto the observation plane $O\xi\eta$.

4.1.2   Diffraction of FDR from the first target at the second target

The FDR from the first target, that propagates towards the second target and reflects from it, is calculated assuming that for the considered wavelength and a metallic foil the FDR and BDR are identical. The first stage of the process (electric field of the FDR produced at the first target and propagating towards the second one) can be represented in analogy with section 4.1.1:

$$
\begin{aligned}
E_{r_1}^{1\to2}(x_2, y_2) &= -\frac{1}{4\pi^2}\frac{ek}{\pi\gamma}\frac{exp(ikd)}{d}\iint \left(\begin{array}{c}\frac{x_1}{\sqrt{x_1^2+y_1^2}}\\\frac{y_1}{\sqrt{x_1^2+y_1^2}}\end{array}\right)K_1\left(\frac{k}{\gamma}\sqrt{x_1^2+y_1^2}\right)\\
&\times exp\left[\frac{ik}{2d}\left((x_1-x_2)^2+(y_1-y_2)^2\right)\right]dx_1dy_1,
\end{aligned}
\tag{4.8}
$$

where x_1, y_1 are the coordinates on the first target surface and d is the distance between the targets.

The diffraction of the FDR at the second target surface and further propagation of the diffracted radiation towards the observation plane give us the final result. It can be calculated simply by multiplication of equation (4.8) by the phase term of the diffracted photons propagating from the second target to the observation plane (see

equation (4.4)).

For the FDR at the observation plane one may obtain:

$$
\begin{aligned}
E_{r_1}^1(\xi, \eta) &= -\frac{1}{4\pi^2} \frac{ek}{\pi\gamma} \frac{exp(ik(d+a))}{ad} \frac{k}{2\pi i} \iiiint \left(\frac{\frac{x_1}{\sqrt{x_1^2+y_1^2}}}{\frac{y_1}{\sqrt{x_1^2+y_1^2}}} \right) K_1 \left(\frac{k}{\gamma} \sqrt{x_1^2 + y_1^2} \right) \\
&\times exp\left[\frac{ik}{2d} \left((x_1 - x_2)^2 + (y_1 - y_2)^2 \right) + \frac{ik}{2a} \left((x_2 - \xi)^2 + (y_2 - \eta)^2 \right) \right] \\
&\times dx_1 dy_1 dx_2 dy_2.
\end{aligned}
\tag{4.9}
$$

In order to simplify the integration and reduce the calculation time we shall rearrange the exponential terms in equation (4.9) in a way, that allows dividing the integration over two surfaces at the same time into integration over $x_2 y_2$ and integration over $x_1 y_1$. After the exponential terms have been rearranged, the FDR from the first target diffracted at the second one can be expressed as follows:

$$
\begin{aligned}
E_{r_1}^1(\xi, \eta) &= -\frac{1}{4\pi^2} \frac{ek}{\pi\gamma} \frac{exp(ik(d+a))}{ad} \frac{k}{2\pi i} \iint \left(\frac{\frac{x_1}{\sqrt{x_1^2+y_1^2}}}{\frac{y_1}{\sqrt{x_1^2+y_1^2}}} \right) K_1 \left(\frac{k}{\gamma} \sqrt{x_1^2 + y_1^2} \right) \\
&\times exp\left[\frac{ik}{2(a+d)} \left((x_1 - \xi)^2 + (y_1 - \eta)^2 \right) \right] G(x_1, y_1, \xi, \eta) dx_1 dy_1,
\end{aligned}
\tag{4.10}
$$

where

$$
\begin{aligned}
G(x_1, y_1, \xi, \eta) &= \iint exp\left[\frac{ik}{2} \left(\sqrt{\frac{a+d}{ad}} x_2 - \sqrt{\frac{ad}{a+d}} \left(\frac{x_1}{d} + \frac{\xi}{a} \right) \right)^2 \right] \\
&\times exp\left[\frac{ik}{2} \left(\sqrt{\frac{a+d}{ad}} y_2 - \sqrt{\frac{ad}{a+d}} \left(\frac{y_1}{d} + \frac{\eta}{a} \right) \right)^2 \right] dx_2 dy_2.
\end{aligned}
$$

For further calculations we rearrange the terms and replace the integration over x_2 and y_2 with the combination of Fresnel's integrals. This allows us to use a rational approximation of the Fresnel's integrals in order to reduce the calculation time and increase the performance of the code (see appendix A). The final result for equation (4.10)

can be written as:

$$
\begin{aligned}
E_{r_1}^1(\xi,\eta) &= \frac{ie\exp\left[ik(a+d)\right]}{4\pi^2\lambda\gamma(a+d)} \iint \left(\frac{\frac{x_1}{\sqrt{x_1^2+y_1^2}}}{\frac{y_1}{\sqrt{x_1^2+y_1^2}}}\right) K_1\left(\frac{k}{\gamma}\sqrt{x_1^2+y_1^2}\right) \\
&\times \left(\left[\cos\left[\frac{k}{2(a+d)}\left((x_1-\xi)^2+(y_1-\eta)^2\right)\right](T_1T_2-T_3T_4)\right.\right. \\
&\left.- \sin\left[\frac{k}{2(a+d)}\left((x_1-\xi)^2+(y_1-\eta)^2\right)\right](T_1T_4+T_3T_2)\right] \\
&+ i\left[\cos\left[\frac{k}{2(a+d)}\left((x_1-\xi)^2+(y_1-\eta)^2\right)\right](T_1T_4+T_3T_2)\right. \\
&\left.\left.+ \sin\left[\frac{k}{2(a+d)}\left((x_1-\xi)^2+(y_1-\eta)^2\right)\right](T_1T_2-T_3T_4)\right]\right) \\
&\times dx_1 dy_1,
\end{aligned}
\tag{4.11}
$$

where $T_1 = T_1(x_1,\xi), T_2 = T_2(y_1,\eta), T_3 = T_3(x_1,\xi), T_4 = T_4(y_1,\eta)$ (see appendix B) are the terms containing Fresnel's integrals.
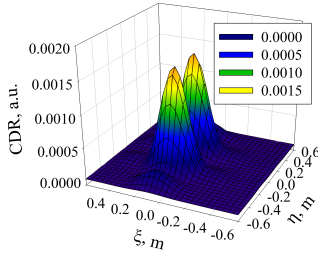
Figure 4.6: The horizontal polarisation component of the CDR from the first target, $h_1 = h_2 = 10$ mm.
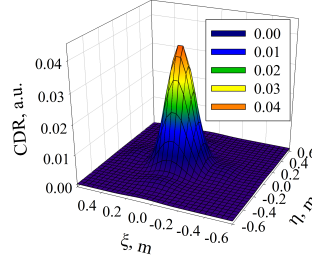
Figure 4.7: The vertical polarisation component of the CDR from the first target, $h_1 = h_2 = 10$ mm.
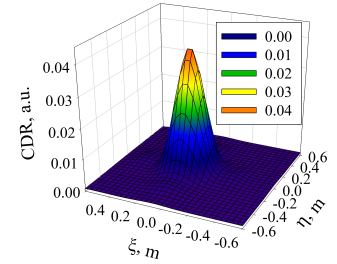
Figure 4.8: The final CDR distribution from the first target, $h_1 = h_2 = 10$ mm.

Figures 4.6, 4.7 and 4.8 demonstrate the CDR distributions from the first target at the observation plane. In the model both targets are positioned at 10mm from the beam, the FDR propagates from the first target towards the second one, reflects from the second target and then it is registered at the observation plane. In figure 4.6 a dual mode shape distribution demonstrates the horizontal polarisation component of the radiation. It is more suppressed than the distribution in figure 4.3 due to the fact that not entire distribution is reflected from the second target. In addition, the radiation

from the upstream target travels a longer distance which results in a decrease of the calculated intensity.

In figure 4.7 the vertical polarisation component of the radiation is presented. It has a single mode shape. The suppression of the radiation intensity compared to figure 4.4 in the case of the second target alone can be explained by the reasons described above. The dominance of the vertical polarisation component in terms of the radiation intensity and overall shape of the final spatial distribution (see figures 4.7 and 4.8) is observed again as in the case of the second target.

4.1.3 DR interference

Once the two radiation components are obtained, one can derive the expression for the DR distribution from the two targets. In order to understand how the FDR from the first target and the BDR from the second target interfere, one should come back to the initial conditions of the considered problem. The only surfaces in the theoretical model which are able to emit DR are the downstream surface of the first target and the upstream surface of the second target. When the FDR is produced from the first target it travels towards the second target, therefore the phase advance of the photons produced at the first target with respect to the photons produced at the second target has to be introduced. Or alternatively the phase delay of the photons from the second target with respect to the first target has to be considered. Based on the mentioned suggestions the following formula can be used:

$$
\begin{aligned}
\frac{d^2W_r^{DR}}{d\omega d\Omega} \;=\; & 4\pi^2 k^2 a^2 \left[\left(ReE_{r_1}^1 - Re\left[E_{r_2}^2 \exp\left(\frac{ikd}{\beta}\right) \right] \right)^2 \right. \\
& \left. + \left(ImE_{r_1}^1 - Im\left[E_{r_2}^2 \exp\left(\frac{ikd}{\beta}\right) \right] \right)^2 \right],
\end{aligned}
\tag{4.12}
$$

where $E_{r_1}^1$ and $E_{r_2}^2$ are the FDR from the first target and the BDR from the second target respectively; $\beta = v/c$ is the speed of an electric charge in terms of the speed of light. The $\exp\left(ikd/\beta\right)$ defines the phase delay of the photons moving from the first target to the second one with respect to the electron beam.

In order to test the suggested formula one may consider a situation when the distance between the targets converges to zero ($d \to 0$):

$$Re\left[E_{r_2}^2 \exp\left(\frac{ikd}{\beta}\right)\right] \to ReE_{r_2}^2 \quad ; \quad Im\left[E_{r_2}^2 \exp\left(\frac{ikd}{\beta}\right)\right] \to ImE_{r_2}^2 \tag{4.13}$$

$$ReE_{r_1}^1 \to ReE_{r_2}^2 \quad ; \quad ImE_{r_1}^1 \to ImE_{r_2}^2 \tag{4.14}$$

This means that the first and the second targets merge into each other, not producing the surfaces capable of emitting radiation. In the context of this discussion it is important to remind the reader that projected dimensions of the targets onto the Oxy plane are considered. The final distribution is therefore:

$$\begin{aligned}
\frac{d^2W_r^{DR}}{d\omega d\Omega} \quad \to \quad & 4\pi^2 k^2 a^2 \left[\left(ReE_{r_2}^2 - ReE_{r_2}^2\right)^2 \right. \\
& \left. + \left(ImE_{r_2}^2 - ImE_{r_2}^2\right)^2\right] \to 0
\end{aligned} \tag{4.15}$$

Another interpretation of formula 4.12 can be studied. Consider propagation of the field E_1 from the first target which travels the distance $a + d$ to the observation plane, and the field E_2 from the second target travelling the distance a to the observation plane. The field at the observation plane can be derived from equations 4.5 and 4.10 as a superposition of the two fields:

$$\begin{aligned}
E(\xi, \eta) \quad = \quad & E_1 exp\left(ik(a+d) + \frac{ik}{2(a+d)}(\xi^2 + \eta^2)\right) \\
& -E_2 exp\left(ik\left(a + \frac{d}{\beta}\right) + \frac{ik}{2a}(\xi^2 + \eta^2)\right),
\end{aligned} \tag{4.16}$$

where E_1 and E_2 are the fields generated from the target surfaces, (ξ, η) are the coordinates on the observation plane and all the phase terms are independent of the integration over the target surfaces. Modifying equation (4.16) further, one obtains:

$$E = E_1 - E_2 exp\left[ikd\left(\frac{1}{\beta} - 1\right)\right] exp\left[\frac{ik}{2}(\xi^2 + \eta^2)\left(\frac{1}{a} - \frac{1}{a+d}\right)\right]. \qquad (4.17)$$

Taking into account that in the experiment at CTF3 the distance between the targets, d, is smaller compared to the distance between the second target and the observation plane, a ($d = 0.27$ m and $a = 2$ m):

$$\frac{1}{a} - \frac{1}{a+d} = \frac{d}{a(a+d)} \approx \frac{d}{a^2}, \qquad (4.18)$$

and considering an asymptotic form of β for large γ:

$$\beta \simeq 1 - \frac{1}{2}\gamma^{-2}, \qquad (4.19)$$

equation 4.17 can be modified as follows:

$$
\begin{aligned}
E(\xi, \eta) &\simeq E_1 - E_2 exp\left[\frac{ikd}{2}\left(\gamma^{-2} + \frac{\xi^2}{a^2} + \frac{\eta^2}{a^2}\right)\right] \\
&= E_1 - E_2 exp\left[\frac{ikd}{2}(\gamma^{-2} + \theta_x^2 + \theta_y^2)\right],
\end{aligned}
\qquad (4.20)
$$

where $\theta_x = \xi/a$ and $\theta_y = \eta/a$ are the photon emission angles.

Introducing the parameter d_c one may obtain:

$$E \simeq E_1 - E_2 exp\left(i\frac{d}{d_c}\right), \qquad (4.21)$$

where d_c is a parameter called the coherence length of radiation. It is defined by the following expression:

$$d_c = \frac{\lambda}{\pi}\frac{1}{(\gamma^{-2} + \theta_x^2 + \theta_y^2)}. \qquad (4.22)$$

If an electron emits two photons at a distance comparable to or smaller than the radiation coherence length, they interfere. An alternative definition is that the electron field and the radiation photon are completely separated at a distance much larger than

the radiation coherence length. Considering small emission angles, for the wavelength $\lambda = 5$ mm and the beam energy $\gamma = 235$ the radiation coherence length is $d_c \simeq 88$ m. The distance between the targets is $d = 0.27$ m, which gives the value of the parameter $d/d_c \simeq 3 \times 10^{-3}$.

Another important limiting factor has to be mentioned here, which is a pre - wave zone effect. At distances $d > \gamma\lambda/2\pi$ from an electron, its field amplitude is significantly suppressed. The radiation is emitted with a divergence of an order of γ^{-1}. In order to reduce the contribution from the radiation source into the radiation spot size, it is important to choose the distance from the target obeying the following condition [59]:

$$\frac{a}{\gamma} \gg \frac{\gamma\lambda}{2\pi} \Rightarrow a \gg \frac{\gamma^2\lambda}{2\pi}. \tag{4.23}$$

The pre - wave zone effect manifests itself in a distortion of the radiation spatial distribution at distances comparable or smaller than $\gamma^2\lambda/2\pi$. From a theoretical point of view in an experiment one should position a detector as far as possible from the source of radiation to apply a Fraunhofer diffraction approximation, however in a millimetre wavelength region hardware constraints usually limit this possibility. For the CDR experiment at CTF3 the parameter $\gamma^2\lambda/2\pi \simeq 44$ m. It was not feasible to place the detector that far from the targets. The distance from the targets to the detection system is approximately 2 m and all measurements were performed in the pre - wave zone.

The CDR spatial distribution can be calculated for different configurations of the experimental setup. For the dual-target system one is interested in understanding how the radiation distribution changes while the upstream target is gradually moving with respect to the fixed downstream target position. In the theoretical model the targets are positioned in the infinite space, therefore not providing a possibility to take into account the surrounding hardware, nevertheless the calculated distributions will be able to show the general properties of the radiation geometry. In figures 4.9, 4.10 and 4.11 the CDR spatial distributions were calculated for three configurations of the experimental setup.

In figure 4.9 the impact parameter of the first target is $h_1 = 60$ mm and the impact
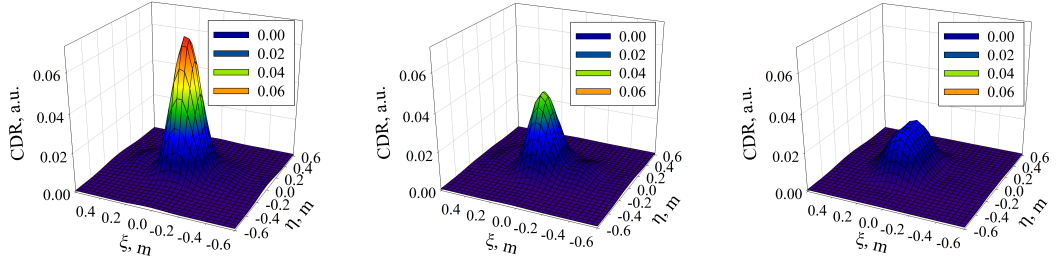
Figure 4.9: The CDR from the two targets: $h_1 = 60$ mm, $h_2 = 10$ mm.

Figure 4.10: The CDR from the two targets: $h_1 = 30$ mm, $h_2 = 10$ mm.

Figure 4.11: The CDR from the two targets: $h_1 = 10$ mm, $h_2 = 10$ mm.

parameter of the second target is $h_2 = 10$ mm, in this case the influence of the first target on the final distribution is suppressed. The shape and intensity of the calculated CDR are very similar to the radiation distribution from the second target alone (see figure 4.5), which is primarily due to the fact that the radiation generated from the first target is very small. In figure 4.10 the upstream target is positioned closer to the line of a beam propagation ($h_1 = 30$ mm; $h_2 = 10$ mm) resulting in the higher radiation intensity generated from the first target. In this case the calculated radiation intensity is reduced due to destructive interference, however the overall shape of the radiation remains the same compared to the distribution in figure 4.9. For the final configuration both targets are positioned at 10 mm from the beam. The distribution in figure 4.11 has even more reduced radiation intensity compared to the first (figure 4.9) and the second (figure 4.10) configurations of the experimental setup, and the shape of the distribution becomes more peculiar transforming itself into a dual hump distribution. Nevertheless, the radiation intensity remains at a measurable level and can be detected in an experiment.

As was previously mentioned CDR occurs at the wavelengths longer or comparable to the bunch length. In the the CTF3 combiner ring the bunch lengths vary in the region of 12 to 20 ps. It is important to investigate how the radiation distribution changes for different wavelengths in the region corresponding to the bunch lengths observed at CTF3. In figure 4.12 the CDR distributions from the two targets positioned at 10mm from the beam as functions of the horizontal coordinate at the observation plane are presented for the six different wavelengths in the region of 3 to 8 mm. The vertical

coordinate is fixed at $\xi = 30mm$, which corresponds to the centres of the targets projected onto the observation plane.
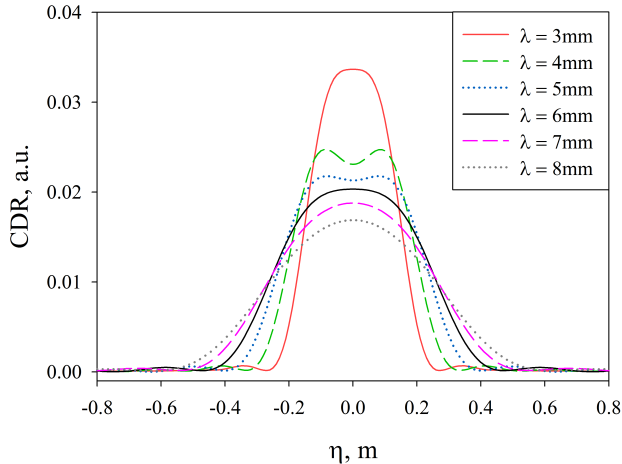
Figure 4.12: The CDR distributions from the dual-target system: $h_1 = h_2 = 10$ mm. The vertical coordinate at the observation plane is fixed at $\xi = 30$ mm.

Figure 4.12 demonstrates an increase of the radiation intensity while the wavelength decreases. The shape of the distribution also changes, demonstrating a more peculiar dual hump distribution for the wavelengths $\lambda = 4$ mm and $\lambda = 5$ mm. We will come back to this effect later on, but now we shall consider another configuration of the targets.

Figure 4.13 shows the CDR distributions at the observation plane for the vertical coordinate fixed at $\xi = 30mm$, the distributions were calculated for the same wavelengths as previously, but now the following target configuration was used: the first target is 30 mm away from the beam and the second target is 10 mm away from the beam. All the distributions have a single peak at $\eta = 0$ mm and the peak intensity increases when wavelengths become smaller. The maximum calculated intensity is larger by approximately a factor two, compared to the distributions in figure 4.12. There are no peculiarities in the shape of the distributions for $\lambda = 4$ mm and $\lambda = 5$ mm.

These two wavelengths are of a particular interest for this theoretical investigation, because the detectors DXP12 and DXP15 which are used in the experiment demonstrate a flat response in the wavelengths regions 3.33 - 5 mm and 4 - 6 mm respectively.
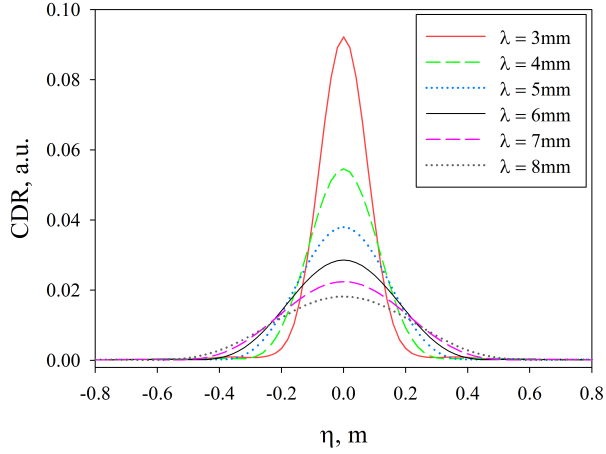
Figure 4.13: The CDR distributions from the dual-target system: $h_1 = 30$ mm, $h_2 = 10$ mm. The vertical coordinate at the observation plane is fixed at $\xi = 30$ mm.

The wavelengths 4 and 5 mm are the central wavelengths of these regions. From the radiation distributions calculated for the first and the second targets separately, for a wavelength $\lambda = 5$ mm we have learnt that the intensity of the horizontal polarisation component is much smaller compared to the vertical polarisation. Since the detectors used in the experiment are polarisation sensitive, they were oriented to measure the vertical polarisation component of CDR.

In order to investigate this fact further the intensities of the vertical and horizontal polarisation components of CDR have to be compared for both configurations of the targets and both wavelengths. Figures 4.14 and 4.15 demonstrate this comparison. The distributions in figure 4.14 were calculated for the configuration when the influence of the upstream target on the distribution is suppressed ($h_1 = 30$ mm, $h_2 = 10$ mm). The vertical polarisation component dominates in terms of calculated intensity, the horizontal polarisation is approximately five times smaller. Situation changes when the upstream target is assumed to be closer to the beam ($h_1 = h_2 = 10$ mm) (see figure 4.15), in this case a destructive interference is observed and the intensity of the vertical polarisation drops considerably. The intensity of the horizontal polarisation, however, stays on approximately the same level. This reduces the difference between the maximum intensities of the horizontal and vertical polarisations and affects the

shape of the final distributions of the CDR for $\lambda = 4$ and 5 mm, which were shown in figure 4.12.
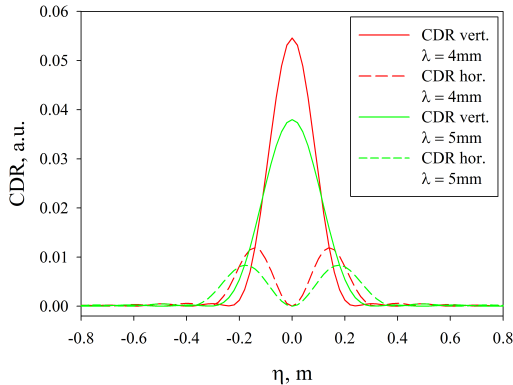
Figure 4.14: The distributions of the horizontal and vertical polarisation components of the CDR calculated for the wavelengths $\lambda = 4$ mm and 5 mm. Impact parameters of the targets: $h_1 = 30$ mm, $h_2 = 10$ mm.
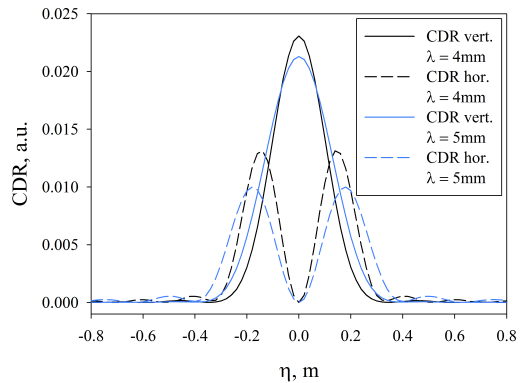
Figure 4.15: The distributions of the horizontal and vertical polarisation components of the CDR calculated for the wavelengths $\lambda = 4$ mm and 5 mm. Impact parameters of the targets: $h_1 = 10$ mm, $h_2 = 10$ mm.

In order to optimise the experimental setup in terms of positioning the targets at a certain distance from the beam, another important aspect of the CDR spatial distribution should be investigated. In order to register CDR at all, the impact parameter of the targets should be smaller or comparable to $\gamma\lambda/2\pi$, which can be derived from the Diffraction Radiation theory. For the wavelength and the beam energy we are considering in this work this parameter is of the order of ~ 0.19 m, therefore even if the upstream target is at 60 mm from the beam the CDR from the target should still be observable. The fact that $\gamma\lambda/2\pi \sim 0.19$ m creates a major problem of the wakefields originating upstream of the experimental setup, suppression of which is achieved by the first target.

It is interesting to investigate a change in the radiation geometry while the second target is moving away from the beam and the position of the upstream target is fixed, it can be achieved by calculating the CDR distribution as a function of the second target rotation and impact parameter. This distribution gives direct information about how the radiation is distributed at the observation plane. At the experimental setup similar measurements can be performed by taking the combination of the rotation and trans-

lation scans of the CDR detected from the second target. The measured distributions can be compared directly with the calculated ones (see chapter 7, section 7.1).

In figure 4.16 the vertical polarisation component of the CDR from the two-target configuration is presented, the targets are positioned at the different distances from the beam: the first target is 30 mm away from the beam and the second target is travelling in the range of 10 - 30 mm away from the beam. This configuration is similar to the positioning of the targets in the experimental setup. In the experiment only one polarisation component can be measured at a time. The distribution in figure 4.16 has a single peak. The peak intensity decreases when the second target is moved further away from the beam or rotated at a large angle. When the upstream target is positioned closer to the beam with the impact parameter $h_1 = 10$ mm (see figure 4.17) the intensity of the radiation is suppressed by approximately 50% and the destructive interference between the targets is observed for the given set of parameters (see table 4.1).
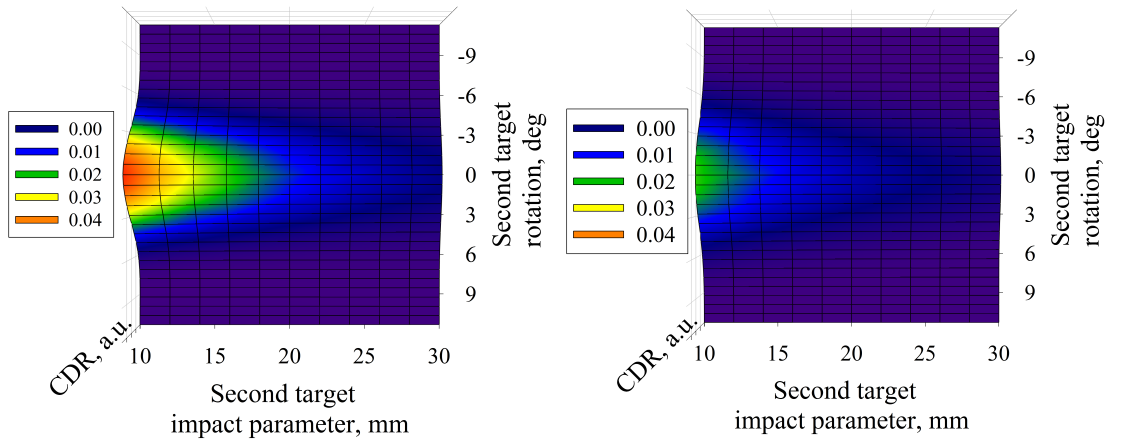
Figure 4.16: The vertical polarisation of the CDR distribution as a function of the second target impact parameter and rotation; $h_1 = 30$ mm.

Figure 4.17: The vertical polarisation of the CDR distribution as a function of the second target impact parameter and rotation; $h_1 = 10$ mm.

Figures 4.18 and 4.19 demonstrate the horizontal polarisation component of the CDR distribution for the same configurations of the targets as for the vertical polarisation component. It is clearly seen from the figures that the radiation distributions have a dual mode shape, which manifests itself in the two separate peaks of the radiation intensity. However when the first target is at 10 mm from the beam the radiation intensity is increased by approximately 20%. Coming back to figures 4.14 and 4.15, one

may conclude that for $\lambda = 5$ mm the intensity of the horizontal polarisation component of CDR, in fact, increases when the upstream target is positioned closer to the beam.

In this theoretical model we discuss the passage of a single electron close to the two-target system. If one considers a bunch of electrons, the distributions presented in figures 4.18 and 4.19 may be distorted because electrons in the bunch have different phases and contribute in the distribution of CDR in a different way which causes a shift of the radiation intensity peaks. In chapter 7 the spatial distributions of the horizontal polarisation of CDR which were measured using the experimental setup at CTF3 will be shown and compared with the present theoretical model.
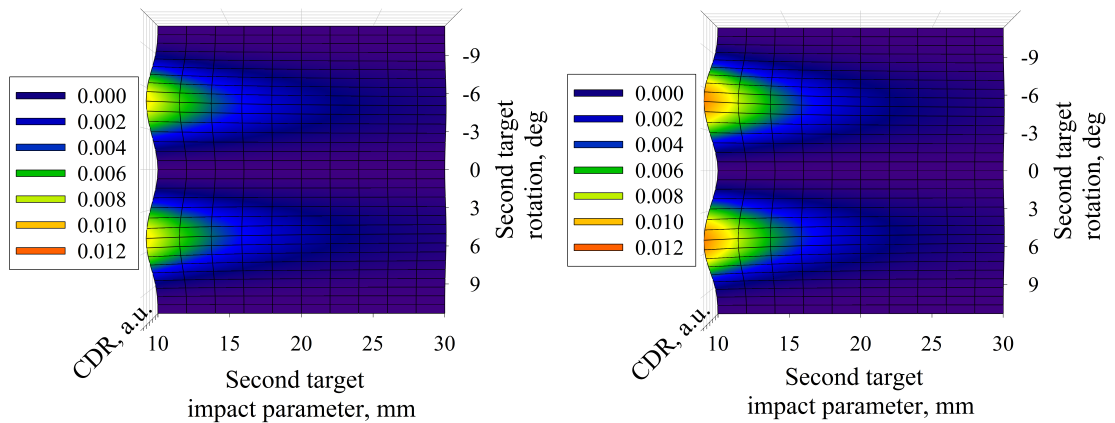
Figure 4.18: The horizontal polarisation of the CDR distribution as a function of the second target impact parameter and rotation; $h_1 = 30$ mm.

Figure 4.19: The horizontal polarisation of the CDR distribution as a function of the second target impact parameter and rotation; $h_1 = 10$ mm.

So far we have been investigating a dependence of the CDR intensity on wavelength. The horizontal and vertical polarisations at $\lambda = 5$ mm behave differently. In order to investigate this closely, the CDR emission as a function of the distance between the targets should be discussed. We shall come back to figures 4.14 and 4.15 which showed the CDR distributions for two different configurations of the targets and two wavelengths. In figure 4.15 the horizontal (angular) coordinate $\eta = 0.19$ m corresponds to the right peak of the horizontal polarisation of the CDR calculated for $\lambda = 5$ mm. By calculating the intensity of the CDR at this coordinate as a function of the distance between the targets for two different target configurations, one may obtain a dependence which characterises zones of constructive and destructive interference between

the targets. The same dependence can be calculated for the vertical polarisation of CDR.

Figure 4.20 shows the intensity of the horizontal polarisation of CDR at ($\xi = 0.03$ m; $\eta = 0.19$ m) as a function of the distance between the targets for two different configurations of the targets.
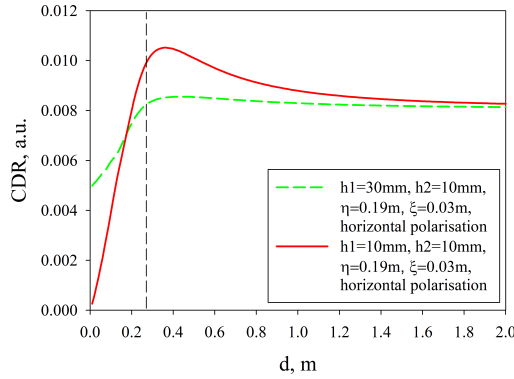
Figure 4.20: The intensity of the horizontal polarisation of CDR at ($\xi = 0.03$ m; $\eta = 0.19$ m) as a function of the distance between the targets.
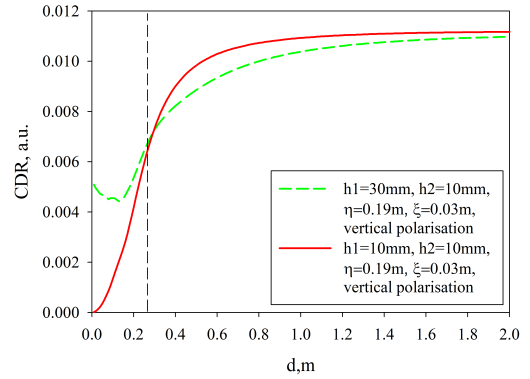
Figure 4.21: The intensity of the vertical polarisation of CDR at ($\xi = 0.03$ m; $\eta = 0.19$ m) as a function of the distance between the targets.

The green dashed curve corresponds to $h_1 = 30$ mm and $h_2 = 10$ mm, it serves as a reference to the red curve which represents the intensity of the interference between the targets when they are at the same distance from the beam, i.e. $h_1 = h_2 = 10$ mm. The black dashed line marks the distance $d = 0.27$ m between the targets. It is seen that the horizontal polarisations of the CDR from the targets interfere constructively, which results in the increase of the radiation intensity when the first target is positioned closer to the beam. This result is also represented by the 2D distributions shown in figure 4.18 and 4.19. As for the vertical polarisation, at the same angular coordinate and for the same distance between the targets the radiations from the targets interfere nether destructively or constructively (see figure 4.21). Both horizontal and vertical polarisations demonstrate a similar dependence on the distance between the targets, however in figure 4.21 the FDR and BDR interfere destructively at the distances $d < 0.27$ m whereas in figure 4.20 the zone of destructive interference is in the region of $d < 0.2$ m.

In the case of the vertical polarisation the same methodology should be applied for the angular coordinate $\eta = 0$, as the vertical polarisation has a central peak at this coordinate (see figure 4.14). In figure 4.22 the vertical polarisation of the CDR is calculated at ($\xi = 0.03$ m; $\eta = 0$ m). At $d = 0.27$ m the radiations from the targets interfere destructively (this result is also shown in the 2D distributions presented in figures 4.16 and 4.17) and the zone of destructive interference begins at the distances $d < 0.5$ m.
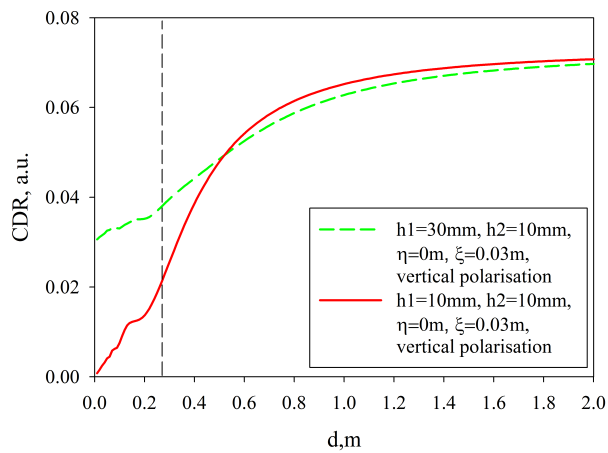
Figure 4.22: The intensity of the vertical polarisation of CDR at ($\xi = 0.03$ m; $\eta = 0$ m) as a function of the distance between the targets.

For all three cases described above, the intensity of the interference between the targets converges to zero when the distance between the targets decreases, which is a fundamental condition that has to be fulfilled for the two-target geometry.

4.2 Summary

The CDR distributions were calculated for two polarisation components of the radiation and for different configurations of the two-target system. The main purpose of the developed model is calculation of a single electron spectrum, knowledge of which is essential for the bunch profile reconstruction procedure. The process of CDR emission was considered in several steps. The simulations were based on the classical theory of Diffraction Radiation. A thin foil approximation was used, the target dimensions,

the distance between the targets and the distance between the second target and the observation plane were fixed.

A comprehensive analysis of the CDR geometry was performed. The CDR from the first target diffracted at the second one and the CDR from the second target were studied separately. The main features of the CDR spatial distributions were identified: the vertical polarisation has a single peak at a mirror reflection angle from the second target, the horizontal polarisation component has dual mode shape and significantly less intense than the vertical polarisation.

A dominance of the vertical polarisation component in the final distribution was confirmed, however for some wavelengths the final distribution changes under the influence of the horizontal polarisation component which is modulated as a function of wavelength. It was confirmed that due to the destructive interference the radiation from the targets positioned at the same distance from the beam is suppressed, but still measurable. The studied features of the CDR distributions will be used in the analysis of experimental data.

Chapter 5

Theoretical work towards longitudinal diagnostics

The main purpose of the experimental setup at CTF3 is to measure the spectrum of the CDR originating from the two targets and to use this spectrum for a bunch shape reconstruction. The main properties of coherent radiation were discussed in detail in chapter 3. Several methodologies can be used for the longitudinal parameters reconstruction. Conventional techniques based on an a-priori information about the bunch profile do not reconstruct the fine details of a real bunch charge distribution precisely. One of the novel bunch profiling techniques, the Kramers - Kronig analysis, will be discussed in this chapter.

Before this technique can be applied an amplitude of a bunch form factor has to be measured over a broad range of frequencies. The form factor can be retrieved from the spectrum of CDR if a single electron spectrum of the two-target configuration is known.

5.1 Spectral measurements using a Michelson interferometer.

At the experimental setup at CERN the CDR is detected using a Michelson interferometer. A schematic layout of this type of interferometer is shown in figure 5.1. The

radiation source which is in our case is the CDR from the dual-target configuration emits radiation propagating towards the beam splitter, where it is divided into two components. The first component is reflected from the fixed mirror, the second component is reflected from the moveable mirror and then they are recombined at the splitter and registered by the detector.
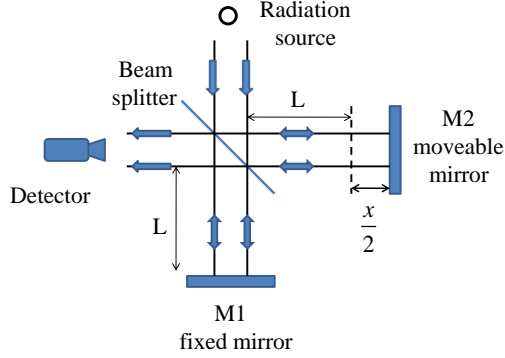
Figure 5.1: Schematic layout of a Michelson Interferometer.

The electromagnetic waves in two arms of the interferometer can be represented as:

$$E_1(f, x) = \frac{E_0(f)}{2}; \tag{5.1}$$

$$E_2(f, x) = \frac{E_0(f)}{2} exp\left[i\frac{2\pi f}{c}x\right]. \tag{5.2}$$

Here $E_0(f)$ is the amplitude of the initial wave emitted by the source, x is the path difference of the wave propagating from the movable mirror and f is the frequency of the initial wave.

The resultant amplitude at the detector can be obtained as a result of the superposition between $E_1(f, x)$ and $E_2(f, x)$:

$$E(f, x) = E_1(f, x) + E_2(f, x) = \frac{E_0(f)}{2}\left(1 + exp\left[i\frac{2\pi f}{c}x\right]\right). \tag{5.3}$$

The intensity distribution will be:

$$
\begin{aligned}
I(f, x) &= E^2(f, x) = E(f, x)E^*(f, x) \\
&= \frac{E_0^2(f)}{4}\left(1 + exp\left[i\frac{2\pi f}{c}x\right]\right)\left(1 + exp\left[-i\frac{2\pi f}{c}x\right]\right).
\end{aligned}
\tag{5.4}
$$

Finally, the intensity of the recombined electromagnetic wave can be expressed as:

$$
I(f, x) = S(f)\left[1 + cos\left(\frac{2\pi f}{c}x\right)\right],
\tag{5.5}
$$

where $S(f) = E_0^2(f)/4$ is the radiation spectrum.

Equation 5.5 represents a superposition of two individual monochromatic waves. Suppose the spectrum of radiation is generated by a polychromatic source, in order to measure this spectrum an integration over all frequencies has to be performed and the interferogram is obtained as:

$$
\begin{aligned}
I(x) &= \int_0^\infty S(f)\left(1 + cos\left(\frac{2\pi f}{c}x\right)\right)df \\
&= \int_0^\infty S(f)df + \int_0^\infty S(f)cos\left(\frac{2\pi f}{c}x\right)df.
\end{aligned}
\tag{5.6}
$$

The integration in equation 5.6 is performed in the infinite limits, however any realistic spectrum is finite and a frequency response of any detector is finite. Real integration limits are defined by the spectral content of an observed radiation and the spectral efficiency of a detector.

When $x = 0$ the interference between all frequencies is constructive and the central maximum of the interferogram is:

$$
I(0) = 2\int_0^\infty S(f)df.
\tag{5.7}
$$

Equation (5.6) can be rewritten in the following form:

$$
I(x) = \frac{1}{2}I(0) + \int_0^\infty S(f)cos\left(\frac{2\pi f}{c}x\right)df.
\tag{5.8}
$$

When $x = \infty$ frequencies add both constructively and destructively and the second term in equation (5.8) converges to zero yielding:

$$I(\infty) = \frac{1}{2}I(0). \tag{5.9}$$

Subtracting the $I(\infty)$ radiation intensity component from the interferogram the following expression is obtained:

$$
\begin{aligned}
I(x) - I(\infty) &= \int_0^\infty S(f) \cos\left(\frac{2\pi f}{c} x\right) df \\
&= \frac{1}{2} \int_{-\infty}^\infty S(f) exp\left(i\frac{2\pi f}{c} x\right) df.
\end{aligned} \tag{5.10}
$$

Applying an inverse Fourier transform to equation (5.10) the spectrum of the observed radiation is obtained as [60]:

$$S(f) = \frac{1}{\pi} \int_{-\infty}^\infty [I(x) - I(\infty)] exp\left(-i\frac{2\pi f}{c} x\right) dx. \tag{5.11}$$

This procedure involves sampling at each position of the movable mirror. The resolution of the interferogram, δ, is defined by the maximum path difference of the radiations in two arms of the Michelson interferometer, x_m [61]:

$$\delta = \frac{1}{x_m}. \tag{5.12}$$

The sample interferograms calculated for the polychromatic sources in the regions of 50 - 75 GHz and 60 - 90 GHz are shown in figures 5.2 and 5.3. The detectors which are used in the experiment at CTF3 demonstrate a flat frequency response in these frequency regions and therefore the theoretical calculations can be later compared with the experiment. In figures 5.2 and 5.3 the maximum path difference is 60 mm, resulting in the interferogram resolution $\delta = 0.017$ mm^{-1}. The time delay corresponding to the maximum path difference is $T_m = x_m/c = 200$ ps and the spectral resolution is $\delta_S = 1/T_m = 5$ GHz.
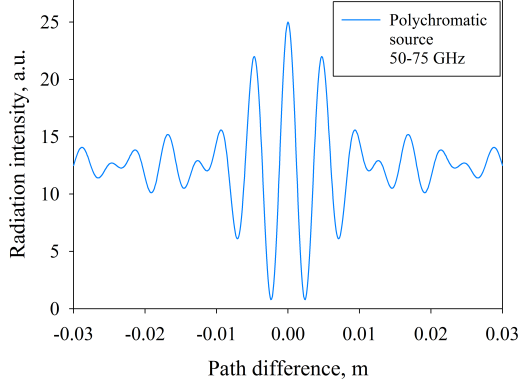
Figure 5.2: The interferogram of the polychromatic source in the frequency region of 50 - 75 GHz.
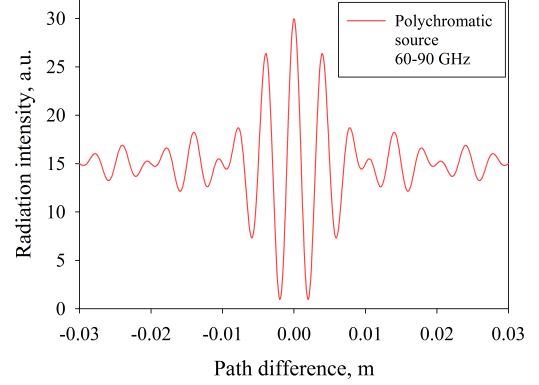
Figure 5.3: The interferogram of the polychromatic source in the frequency region of 60 - 90 GHz.

5.2 Single electron spectrum

Now we shall come back to the discussion about the spectrum of CDR. The following approximation for the coherent spectrum of radiation can be used [25]:

$$S_{coh}(\omega) \simeq N^2 S_e(\omega) F(\omega). \tag{5.13}$$

N is the number of electrons directly measured in an experiment. In order to obtain information about the form factor $F(\omega)$ one should first calculate the single electron spectrum $S_e(\omega)$.

By integrating the DR distributions (chapter 4, subsection 4.1.3) over a detector aperture the single electron spectrum can be obtained:

$$
\begin{aligned}
S_e(\omega) \;=\; 4\pi^2 k^2 a^2 \int & \left[\left(Re E_{r_1}^1(\xi,\eta) - Re\left[E_{r_2}^2(\xi,\eta) \exp\left(\frac{ikd}{\beta} \right) \right] \right)^2 \right. \\
& \left. + \left(Im E_{r_1}^1(\xi,\eta) - Im\left[E_{r_2}^2(\xi,\eta) \exp\left(\frac{ikd}{\beta} \right) \right] \right)^2 \right] d\Omega,
\end{aligned}
\tag{5.14}
$$

where $E_{r_1}^1$ is the CDR from the first target, diffracted at the second one, $E_{r_2}^2$ is the CDR from the second target and

$$d\Omega = \sin\theta d\theta d\varphi = d\theta d\varphi. \tag{5.15}$$

The radiation is calculated at any angle θ from $0 \deg$ to $90 \deg$. θ and φ determine the angles of photon emission by an arbitrary elementary source on the target surfaces. In terms of the coordinates on the observation plane, equation (5.15) can be rewritten as:

$$d\Omega = \frac{1}{a^2}d\xi d\eta. \tag{5.16}$$

By substituting equation (5.15) into equation (5.14) the expression for the single electron spectrum can be obtained:

$$
\begin{aligned}
S_e(\omega) &= 4\pi^2 k^2 \iint \left[\left(ReE_{r_1}^1(\xi,\eta) - Re\left[E_{r_2}^2(\xi,\eta)\exp\left(\frac{ikd}{\beta}\right)\right]\right)^2 \right. \\
&\quad \left. + \left(ImE_{r_1}^1(\xi,\eta) - Im\left[E_{r_2}^2(\xi,\eta)\exp\left(\frac{ikd}{\beta}\right)\right]\right)^2 \right] d\xi d\eta. \tag{5.17}
\end{aligned}
$$

Figure 5.4 shows the single electron spectra for three different configurations of the system [58]. The blue curve: both targets are at the same distance from the beam ($h_1 = h_2 = 10$ mm); the red curve: the first target impact parameter is $h_1 = 12$ mm, the second target impact parameter is $h_2 = 10$ mm; the black curve: the first target is even further from the beam ($h_1 = 14mm$, $h_2 = 10mm$).

The intensity of detected radiation decreases due to the destructive interference when the upstream target is gradually inserted into the beam pipe. The spectra were calculated for the detector with 20 x 20 mm aperture. In order to obtain the spectral data points a DR distribution was integrated over a grid of discrete points within the area of 20 x 20 mm at the observation plane.

Figure 5.5 shows the spectrum of CDR when the targets are at the same distance from the beam. It is clear that the shown spectrum features the trailing structures which have interferometric nature. The spectral intensity is one order of magnitude smaller than of the spectrum presented in figure 5.6 which is caused by the destructive
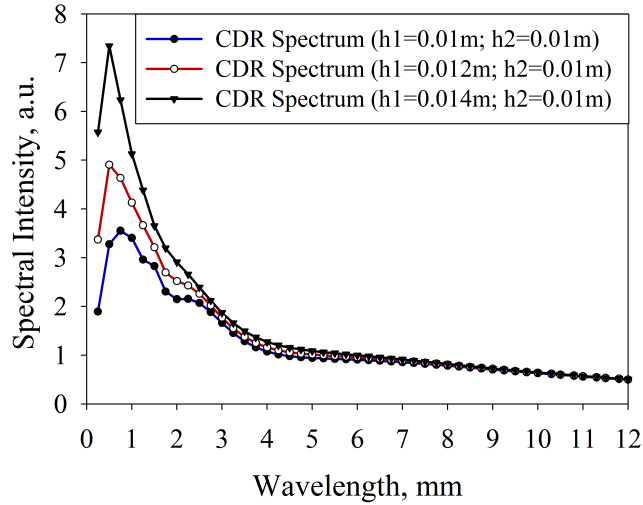
Figure 5.4: The DR spectra for the three different configurations of the setup: $h_1 = 0.01$ m, $h_2 = 0.01$ m; $h_1 = 0.012$ m, $h_2 = 0.01$ m; $h_1 = 0.014$ m, $h_2 = 0.01$ m. The spectra were calculated for the detector with 20 x 20 mm aperture.

interference. When the upstream target is lifted up in the beam pipe its influence on the spectrum should be significantly suppressed as well as the spectrum should become similar to the one target configuration spectrum. This effect is clearly seen in figure 5.6 as the spectral intensity goes up and the trailing structures vanish.

In all figures the spectra demonstrate a suppression of the spectral intensity at smaller and larger wavelengths. The radiation intensity demonstrates a strong dependence on wavelength when the following condition is fulfilled:

$$\frac{2\pi h}{\gamma \lambda} \simeq 1. \tag{5.18}$$

This means that the Coulomb field of a charged particle becomes comparable to the distance h between the charge and the targets. From equation (5.18) one can calculate a characteristic wavelength at which a small wavelengths suppression of the spectrum begins. At the wavelengths less than $\lambda = 2\pi h/\gamma \simeq 0.27$ mm (calculated for $h = 10$ mm) a significant intensity suppression is achieved. At large wavelengths, suppression of the spectra occurs due to the finite size of the targets. This effect was well described in [62].
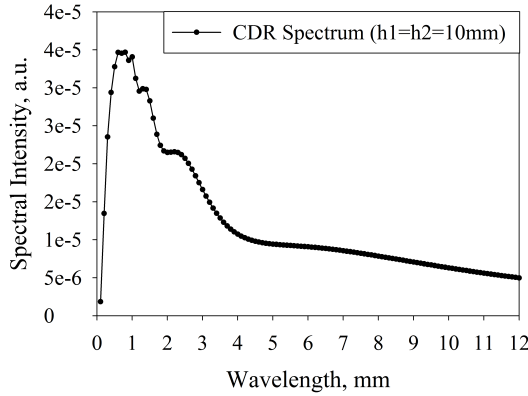
Figure 5.5: The DR spectrum when both targets are 10 mm away from the beam. The spectrum was calculated for the detector with 20x20 mm aperture.
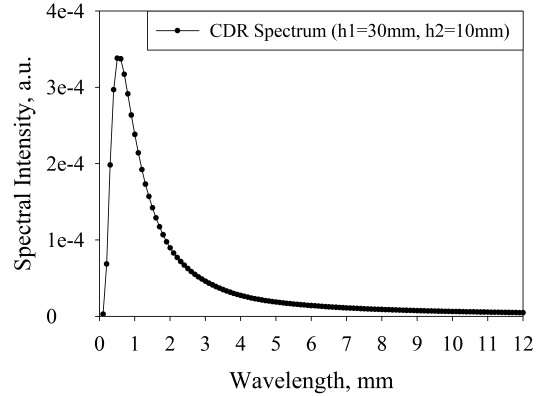
Figure 5.6: The DR spectrum when the upstream target is at 30 mm and the downstream target is at 10mm from the beam. The spectrum was calculated for the detector with 20 x 20 mm aperture.

5.3 Kramers-Kronig analysis

The resulting spectrum that can be derived from interferometric measurements is related to the bunch form factor and can provide information about the longitudinal bunch profile. Once the frequency dependence of the radiation intensity has been obtained over a significant spectral range there is a possibility to use the Kramers-Kronig relation. It is applied to the spectral form factor to find the minimal phase and then the bunch shape can be obtained by taking a Fourier transform of the form factor amplitude. The analysis performed in this section makes use of extrapolations into frequency regions that are not covered by the detectors used in the experiment. The Kramers-Kronig technique can be applied specifically for asymmetric bunch shapes.

The coherent spectrum of the bunch of N_e electrons is given by the product of the single electron spectrum $S_e(\omega)$ defined at frequencies ω, and the bunch form factor $F(\omega)$ containing information about the bunch spatial dimensions (see equation 5.13). For relativistic charged particles when the radiation is propagated in the forward direction, the form factor $F(\omega)$ can be obtained as a modulus squared of a Fourier transform applied to the longitudinal charge distribution $\rho(z)$ [25]:

$$F(\omega) = \left| \int_0^\infty \rho(z) exp\left(i\frac{\omega z}{c}\right) dz \right|^2, \tag{5.19}$$

where z is the longitudinal coordinate.

The reconstruction of the longitudinal profile by the inverse Fourier transformation is not possible because only the amplitude of the form factor can be measured in the experiment, not its phase. To obtain the missing phase information from the measured data an analytical method based on the Kramers-Kronig analysis was proposed in [63]. The Kramers-Kroing relation connects real and imaginary parts of an analytic function. The complex form factor can be defined as:

$$\widehat{F}(\omega) = \int_0^\infty \rho(z) exp\left(i\frac{\omega z}{c}\right) dz \equiv \sqrt{F(\omega)} exp\left(i\psi(\omega)\right). \tag{5.20}$$

The form factor amplitude and the phase factor are related by the Kramers-Kronig relation in a way that if the function $F(\omega)$ is measured at all frequencies than the phase factor $\psi(\omega)$ can be obtained as follows [64]:

$$\psi(\omega) = -\frac{2\omega}{\pi} \int_0^\infty \frac{\ln(\sqrt{F(x)}/\sqrt{F(\omega)})}{x^2 - \omega^2} dx, \tag{5.21}$$

where x is integration variable in the units of frequency. With $\psi(\omega)$ known the normalized longitudinal bunch distribution function can be determined as:

$$\rho(z) = \frac{1}{\pi c} \int_0^\infty \sqrt{F(\omega)} \cos\left(\psi(\omega) - \frac{\omega z}{c}\right) d\omega. \tag{5.22}$$

In practice measurement of $F(\omega)$ over the entire frequency interval is not feasible, but if the coherent spectrum covers a significant frequency range there is a possibility to extrapolate the spectrum to zero and to larger frequencies. In this section the Kramers-Kronig relation will be applied to the reconstruction of a double-gaussian charge distribution. Further in this section we apply discretisation to all formulas. It will both help to avoid discontinuities in the denominator of the phase function (see equation 5.21) and simulate an experimental measurement of the form factor data points defined at a certain wavenumber range.

Suppose we have the region (k_{n_0}, k_N) where the form factor is defined or measured at each discrete point. This region of wavenumbers is within the larger region of values (k_0, k_M) which provides a sufficient coverage of all features of the form factor. In order to define a fitting function over (k_0, k_M) an interpolation function between the known or measured form factor data points (k_{n_0}, k_N) has to be developed and the extrapolation functions in (k_0, k_{n0}) and (k_N, k_M) shall be introduced.

In order to interpolate between the form factor data points the following function was applied [65]:

$$F_{int}(k_m) = \frac{\sum\limits_{n=n_0}^{N} F(k_n)\, exp\left(-\frac{(k_n - k_m)^2}{2\sigma^2}\right)}{\sum\limits_{n=n_0}^{N} exp\left(-\frac{(k_n - k_m)^2}{2\sigma^2}\right)}, \tag{5.23}$$

where $F(k_n)$ is the form factor data, σ is the smoothing parameter which was practically chosen by studying a variety of asymmetric bunch shapes and achieving the best extrapolations, $\sigma = \frac{\Delta k_n}{3}$ where $\Delta k_n = k_n - k_{n-1}$. k_n are the data points where the form factor is defined, k_m are the data points where the interpolation function is defined, k_n and k_m are shifted by $\triangle k_n/4 = \triangle k_m/4$.

In [66] an extrapolation function towards small wave numbers was suggested as $F_{small} \sim e^{-\alpha k^2}$ where α is chosen to smoothly join the data points. The extrapolation procedure should satisfy the following conditions: $F_{small} \to 1$ as $k \to 0$ and match the data at the smallest wavenumber. The following extrapolation function was suggested:

$$F_{small}(k_m) = exp(-\eta k_m^2), \tag{5.24}$$

where η is defined from the condition that the extrapolation function should match the interpolation function at the smallest wave number:

$$F_{small}(k_{n0}) = F_{int}(k_{n0}). \tag{5.25}$$

The large wave numbers extrapolation was proposed as [65]:

$$F_{large}(k_m) = exp(-\beta k_m^2 + \gamma k_m) + exp(-\delta k_m^2), \tag{5.26}$$

where β, γ, δ are obtained from the system of equations:

$$\begin{cases} F_{large}(k_N) & = & F_{int}(k_N) \\[2mm] \dfrac{dF_{large}(k_m)}{dk_m}|_{k_N} & = & \dfrac{dF_{int}(k_m)}{dk_m}|_{k_N} \\[2mm] \dfrac{d^2 F_{large}(k_m)}{d^2 k_m}|_{k_N} & = & \dfrac{d^2 F_{int}(k_m)}{d^2 k_m}|_{k_N} \end{cases} \tag{5.27}$$

where k_N is the largest wave number.

$F_{fit}(k_m)$ is a function that combines the interpolation $F_{int}(k_m)$ between the form factor data points $F(k_n)$, the extrapolation to zero $F_{small}(k_m)$ and the extrapolation to large wave numbers $F_{large}(k_m)$:

$$F_{fit}(k_m) = \begin{cases} F_{small}(k_m) \;\; if \;\; m < n_0 \\[3mm] F_{int}(k_m) \;\; if \;\; m \geq n_0 \;\; and \;\; m \leq N \\[3mm] F_{large}(k_m) \;\; if \;\; m > N \end{cases} \tag{5.28}$$

where n_0 and N correspond to the first and the last point of the detector coverage range.

After applying discretisation to equation (5.21) the modified expression for the phase factor is obtained:

$$\psi(k_\tau) = -\frac{2k_\tau}{\pi} \sum_{m=0}^{M} \frac{\ln(\sqrt{F_{fit}(k_m)})/\ln(\sqrt{F_{fit}(k_\tau)})}{k_m^2 - k_\tau^2} \Delta k_m, \tag{5.29}$$

where M is the number of discrete points shifted with respect to k_n by $\Delta k_m/4$. $M = T$, T is the number of discrete points that are shifted by $\Delta k_\tau/2$ with respect to k_n, where $\Delta k_m = \Delta k_\tau = k_m - k_{m-1} = k_\tau - k_{\tau-1}$ are discretisation steps. $F_{fit}(k_m)$ and $F_{fit}(k_\tau)$ are determined at the points that are shifted by $\Delta k_m/4$ to avoid discontinuity in the denominator of equation (5.29).

Finally, the normalised longitudinal bunch distribution function can be written as:

$$S(z) = \frac{1}{\pi} \sum_{\tau=0}^{T} \sqrt{F_{fit}(k_\tau)} \cos(\psi(k_\tau) - zk_\tau)\Delta k_\tau, \qquad (5.30)$$

where z is the longitudinal coordinate.

Consider the following charge distribution in a bunch:

$$\rho(z) = \frac{exp(-z^2/2\sigma_1^2)}{4\sqrt{2\pi}\sigma_1} + \frac{3exp(-(z-z_0)^2/2\sigma_2^2)}{4\sqrt{2\pi}\sigma_2}, \qquad (5.31)$$

where $z_0 = 1.5$ mm, $\sigma_1 = 0.3$ mm, $\sigma_2=0.45$ mm. From equation (5.19) the form-factor of the suggested longitudinal charge distribution can be calculated as follows:

$$F(k) = \frac{1}{16}\left(exp(-\sigma_1 k^2) + 9exp(-\sigma_2 k^2) + 6exp\left(-\frac{k^2(\sigma_1^2 + \sigma_2^2)}{2}\right)cos(kz_0)\right). \quad (5.32)$$

Both the longitudinal profile and the corresponding form factor are shown in figure 5.7 and figure 5.8. The longitudinal profile has a double-gaussian shape with one central peak and one collateral peak. The influence of the collateral peak on the shape of the form factor is seen in figure 5.8. A form factor of a Gaussian longitudinal profile is an exponentially decreasing function. In the case of the charge distribution in equation (5.31) the form factor shape changes and it demonstrates more complex behavior towards large wavenumbers.
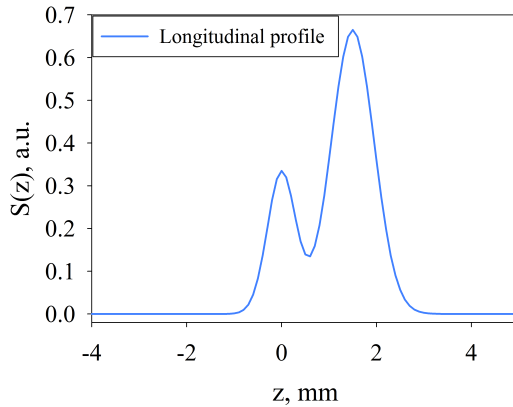
Figure 5.7: The longitudinal charge distribution of the bunch described by equation (5.31).
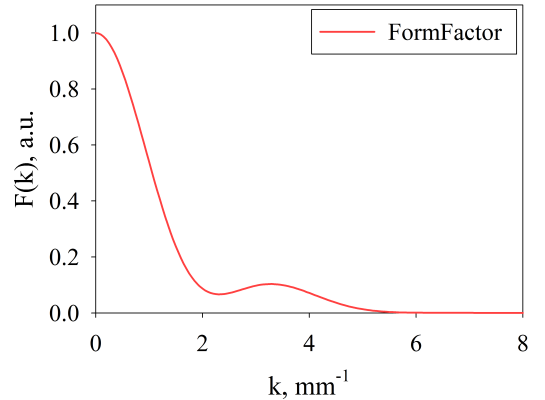
Figure 5.8: The form factor of the charge distribution in figure 5.7.

As was mentioned earlier, it is not feasible to have an infinitely broad spectral coverage of a detection system. Having developed the fitting functions for the longitudinal profile reconstruction, there is a possibility to use them for different scenarios of a detector spectral coverage.

If a spectral range measured in an experiment is too short, especially towards larger wavenumbers, the method does not reconstruct trailing structures that follow a dominant peak, or in other words it is not sensitive to asymmetries in the longitudinal charge distribution. Two examples of the longitudinal bunch profile reconstruction based on the knowledge of the form factor data points in two different frequency ranges are shown in figures 5.10 and 5.12.
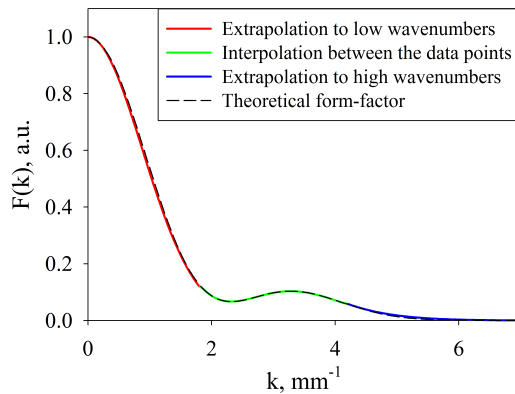
Figure 5.9: The form factor reconstruction by applying the extrapolation and interpolation procedures. The form factor is known in $k = 1.8 - 4.2 m^{-1}$.
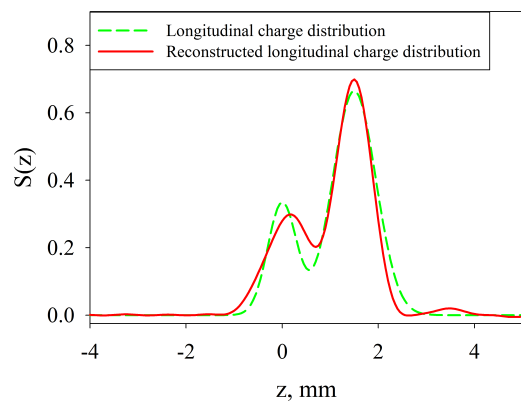
Figure 5.10: The reconstruction of the longitudinal profile of the bunch. The corresponding form factor is in figure 5.9.

Consider the first example when a chosen wavenumber range where the form factor is known is 1.8 - 4.2 mm^{-1}. In figure 5.9 the green curve is the interpolation function between the data points, assuming that they are known from an experiment; the red and blue curves are the extrapolations to the smaller and larger wavenumbers respectively; the dashed curve is the calculated form factor. Figure 5.9 clearly demonstrates that the suggested extrapolation procedures (see equations (5.24) and (5.26)) work very well. By applying equations (5.29) and (5.30) one may obtain the final longitudinal charge distribution of the bunch. Figure 5.10 demonstrates a comparison of the initial distribution with the reconstructed one using the Kramers-Kronig technique. The

calculated and the initial distributions agree well, but some mismatches are present due to the limited range of wavenumbers (0 - 7 mm^{-1}) where the numerical calculation was performed and inaccuracies in the interpolation and extrapolation techniques.
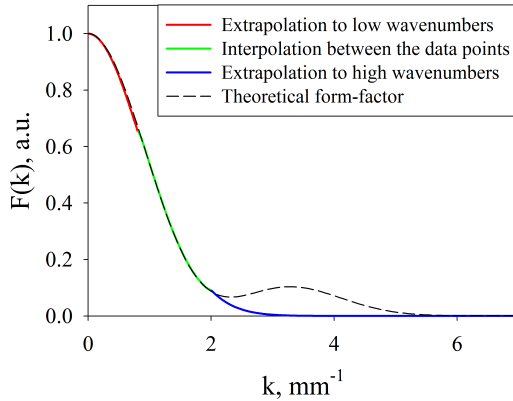
Figure 5.11: The form factor reconstruction by applying the extrapolation and interpolation procedures. The form factor is known in $k = 1$ - 2 mm^{-1}.
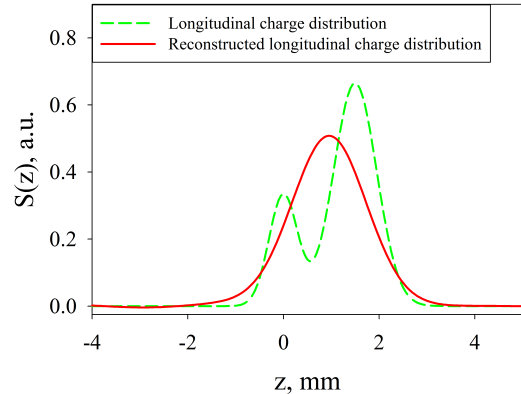
Figure 5.12: The reconstruction of the longitudinal bunch profile. The corresponding form factor is in figure 5.11.

In order to demonstrate the importance of a sufficient frequency coverage range of a detector, another reconstruction was performed, but with a shift of the known wavenumber range toward the smaller wavenumbers. Consider the data range of 1 - 2 mm^{-1}. As in the previous figure the green curve is the interpolation, assuming this part of the form factor is known from an experiment, the red and blue are the extrapolation functions and the dashed curve is the theoretical form factor. From figure 5.11 one may conclude that the simulated detector coverage range in the wavenumber domain is not sufficient to reconstruct the trailing structures of the form factor, which results in an inaccurate reconstruction of the final charge distribution in the bunch (see figure 5.12).

5.4 Summary

In this chapter the principles of coherent radiation spectral measurements using a Michelson interferometer were explained in detail. The spectrum of CDR contains information about the longitudinal profile of the bunch, however before this information can be extracted the single electron spectrum has to be calculated. The calculation

of the single electron spectrum was performed based on the theoretical model developed in chapter 4. The spectrum was obtained by integrating the radiation spatial distribution over a detector aperture and was calculated for different configurations of the dual-target system.

In order to reconstruct the longitudinal profile of the bunch, one needs to recover the missing phase information of the electrons in the bunch. When the spectral measurements are taken and the single electron spectrum is calculated, it is possible to calculate the form factor data points, however this does not provide the missing phase information. In this work the Kramers-Kronig technique was studied as a tool for the phase and longitudinal profile reconstruction. The problematic issues of having insufficiently broad sensitivity range of a detection system were discussed. It is important to point out that the phase retrieval problem cannot be solved by the Kramers-Kronig methodology completely, due to the fact that this technique assumes that the spectrum of radiation is an analytical function. Indeed it is not feasible to describe a real spectrum with analytical function and therefore the reconstruction of the bunch profile will not be unique.

In section 5.3 two different scenarios of the form factor spectral coverage were considered. It was pointed out that the bunch profile reconstruction can be accurate only if the form factor data points are obtained over a broad range of frequencies. The development of a detection system which would provide this ability is very important. One may consider usage of a grating spectrometer. If one grating is used, the spectrometer is only able to provide a coverage of very small part of the coherent radiation spectrum and the ratio of the longest to the shortest measured wavelength is approximately two. The latter is also known as a spectral octave. Therefore several gratings have to be used in order to provide a sufficient coverage of several octaves in the spectrum for an accurate bunch profile reconstruction.

Coherent Diffraction Radiation setup

In this chapter a Coherent Diffraction Radiation setup will be discussed in detail. Installation of the setup was carried out in two stages, the first part of the installation was performed by Maximilian Micheler who was responsible for the setup in 2008 - 2010 [67].

In January 2011 an upgrade of the experimental setup with the second target was performed by the author of this thesis. Several modifications to the interferometric system were introduced as well. All modifications and the detailed explanation of the upgrade will be presented in this chapter.

6.1   Location of the experiment

The experiment is installed at the CLIC Test Facility (CTF3) in the Combiner Ring Measurements (CRM) line, which is an extended straight section after the first bending magnet in the combiner ring (see figure 6.1). During the operation of the experiment, the electron beam had a train length of 200 ns to 300 ns, a bunch sequence frequency of 3 GHz and a nominal current of 3.5 A.

Figure 6.2 shows the devices upstream and downstream of the bending magnet CR.BHF0205, which is positioned at the beginning of the CRM line [68]. CR.QDF0160 and CR.QFF0190 are the quadrupole magnets which allow for the beam optics to be changed and are used to deliver a transversely circular electron beam to the CDR setup. The corrector dipole magnets, CR.DHF0200 and CR.DVF0200, allow for the trajectory
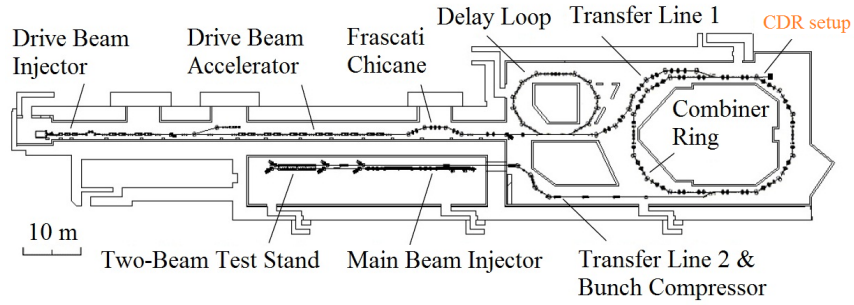
Figure 6.1: General Layout of the CTF3.
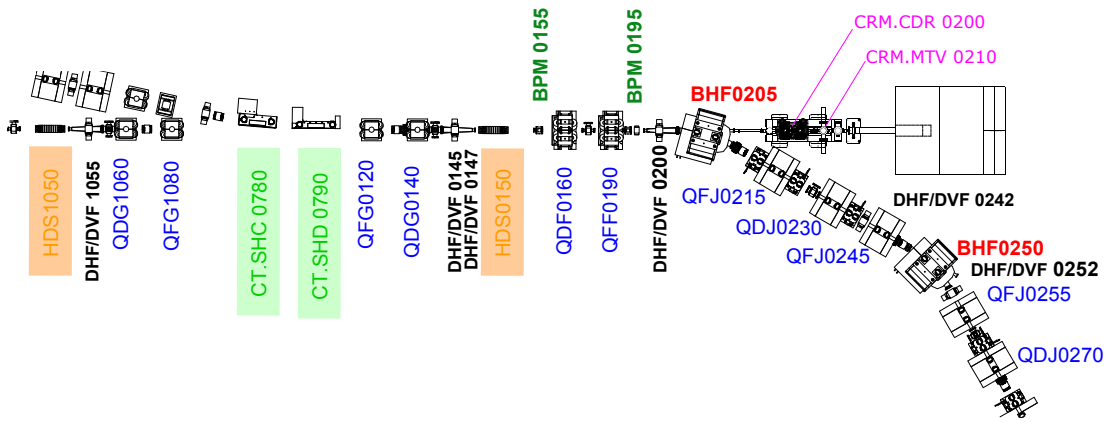
Figure 6.2: Magnets and beam instrumentation devices in CR and CRM line. Bending magnets (red), quadrupole magnets (blue), deflector magnets (black), BPMs (dark green), beam instrumentation devices including CDR setup (magenta), septa (green) and RF deflectors (orange).

into the CRM line to be adjusted. The beam position monitors, CR.BPM0155 and CR.BPM0195, provide beam current readings with a sampling rate of 5.2 ns.

There were several reasons why the CRM line was chosen as the location for the CDR setup. The CRM line provided enough room for the installation of an optical table alongside the beam line and also sufficient working space. Proximity of the beam instrumentation in the combiner ring (CR) and the transfer line 1 (TL1) to the CDR setup was of great importance as well. The CRM line is equipped with a vacuum valve and a vacuum pipe, which provided an autonomous vacuum environment and allowed for minor installations to be performed at the setup without breaking the vacuum in the rest of the machine. Coherent Synchrotron Radiation (CSR) generated in the bending magnet CR.BHF0205 can be reflected from the downstream target and used

as a parasitic probe source for testing the measurement system, data acquisition and CSR suppression scheme.

6.2 Description of the setup

A schematic diagram indicating the configuration of the experimental equipment is shown in figure 6.3. When the bending magnet at the beginning of the CRM line is switched off the beam propagates straight towards the beam dump, moving past the dual-target system. When the Coulomb field of the beam interacts with the targets, Forward Diffraction Radiation (FDR) is produced from the aluminium coated downstream surface of the first target and Backward Diffraction Radiation (BDR) is produced from the upstream surface of the second target. The FDR propagates in the same direction as the beam and reflects from the second target when it reaches the target surface. The BDR is produced in the direction of the mirror reflection from the second target. Finally, both the reflected FDR and the BDR travel together towards the diamond view port and then down to an optical table.
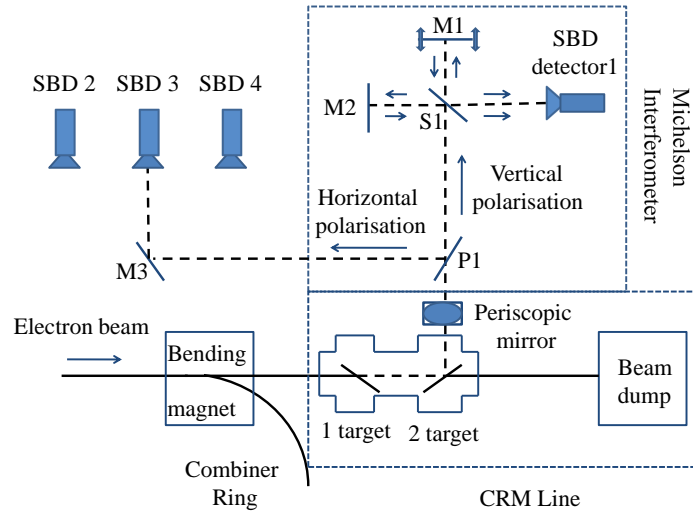
Figure 6.3: Schematic diagram of the experimental setup in the CRM line.

The optical table is positioned alongside the beam line, but it is lowered with respect to the beam horizontal plane to avoid the beam based backgrounds. The periscopic mirrors are used to translate the signal from the targets down to the optical

table where it is split into two polarisation components by the polariser (P1). The vertical polarisation component propagates towards the beam splitter in the Michelson interferometer where it is split into two components, the first one is reflected from the fixed mirror (M2) and the second one from the movable mirror (M1) and finally they are recombined at the splitter and then detected by the Schottky Barrier Diode 1 (SBD). The horizontal polarisation component travels towards the mirror M3 positioned beside the interferometer, then it is reflected from the mirror and registered by the SBD detectors 2, 3 or 4. The main characteristics of the detectors used in the experiment will be discussed in section 6.3.4. The signals from the detectors are read out for each train of bunches passing the two-target system. The setup DAQ will be discussed in section 6.3.5.

The vertical polarisation of CDR was chosen for the interferometric measurements based on the theoretical calculations, which showed that a higher radiation intensity should be detected compared to the horizontal component. The SBD detectors 2, 3 and 4 which are positioned beside the interferometer are used primarily for on-line bunch shape stability monitoring.

6.3 The setup upgrade

6.3.1 Vacuum components

Two coupled ultra-high vacuum (UHV) six-way crosses (VG Scienta, ZBX610RS) were installed in the CRM line. The outer diameter of the six-way cross flanges is 150 mm, the diameter of the six cylindrical ports is 95.7 mm and the length of each six-way cross is 270 mm.

In the initial configuration, in 2008, only the downstream cross contained a target mounted on a 4D manipulator and positioned at 45 deg with respect to the beam propagation direction. The BDR produced from the upstream surface of the target was observed in the interferometer.

In January 2011 a second target was installed in the upstream cross by the author of this thesis. The targets are silicon wafers coated with aluminum. They are placed to one side of the electron beam with impact parameters which can vary in the region

of 0 to 40 mm. The intensity of CDR depends on reflection properties of the targets. Aluminium was chosen as a coating for the targets as it has a high reflectivity in the far-infrared region.

The downstream target is attached to the shaft of a 4D UHV manipulator (VG Scienta, HPT Translator MRXZ0570). The manipulator is mounted on top of the downstream cross and provides precise remote control of the rotational and vertical translation axes. Two remaining dimensions can be controlled locally. The manipulator is equipped with the stepper motors which provide a single step precision of 0.004 deg. for rotation and 1μm for translation. The motors are driven and monitored with a BALDOR NextMove e100 motion controller via custom cable connections. To prevent radiation damage of the motion controller, it was moved out of the experimental hall. Each axis is equipped with a power supply for the motors, an encoder and two limit switches for each of which dedicated cabling was implemented.
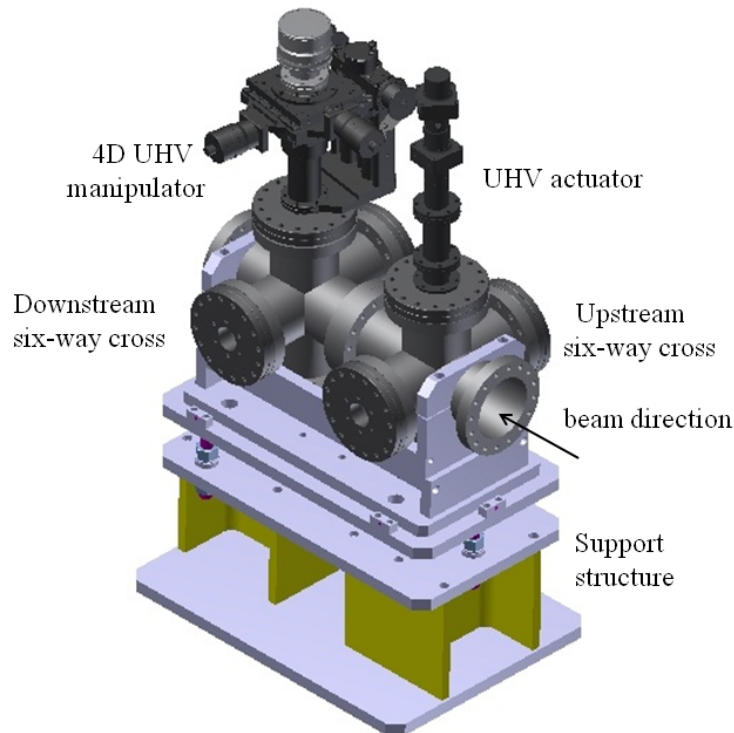
Figure 6.4: The assembly consisting of the two six-way crosses with the manipulators installed on top of them.

The upstream target is attached to the shaft of an UHV actuator (VG Scienta, ZLDS250M) which is mounted on top of the upstream cross and provides a remote control of the vertical translation axis. The manipulator is equipped with a stepper motor which is driven and monitored with the BALDOR NextMove e100 motion controller via custom cable connections. The translation is limited by the limit switches for which dedicated cabling was implemented. The whole assembly which consists of the two six-way crosses with the manipulators installed on top of them is shown in figure 6.4.

The translation range for both manipulators is 50 mm, however only 40 mm are used for the translation of the upstream target and 46 mm for the translation of the downstream target, reaching a lowest position of 10 mm and 6 mm below the centre of the six-way crosses for the upstream and downstream targets respectively.

An off-centre adaptor flange is installed in the downstream cross with 15 mm offset with respect to the center of the cross (see figure 6.7). The adapter flange has an outer diameter of 150 mm with a concentric bore of 38 mm in order to install a viewport. This installation was performed to minimise the backgrounds originating downstream of the setup.
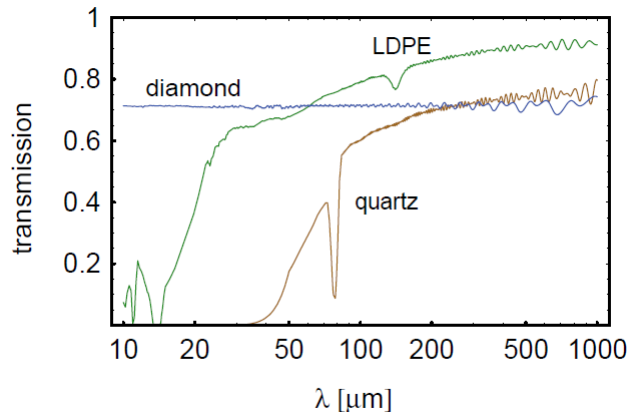
Figure 6.5: Intensity transmission coefficient as a function of wavelength for a 0.5 mm thick window made from CVD diamond, low-density polyethylene or single crystal quartz.

A vacuum window through which the radiation is detected is a 0.5 mm thick CVD diamond vacuum window with a viewing diameter of 30 mm, it is coupled to a 70mm

106

outer diameter UHV flange. Diamond exhibits a broadband transparency in the far-infrared and millimetre wavelength ranges. The intensity transmission coefficients as functions of wavelength for windows made from CVD diamond, low-density polyethylene and single crystal quartz are shown in figure 6.5 [69]. The window thickness of 0.5 mm is smaller than or comparable to the wavelengths observed in the experiment, and therefore minimises the view port absorption and the distortions of the transmitted radiation spectrum due to multiple reflections. In the upstream cross a quartz window is installed and used for alignment purposes only.

6.3.2 Installation of the second target

Installation of the second target was performed during a CTF3 shutdown in January 2011. Before the installation, the shaft connecting the second target actuator with the target holder had to be manufactured at Royal Holloway Physics department workshop. After all the components were ready, namely the actuator, limit switches, shaft, target holder and the target, they were preassembled and tested.
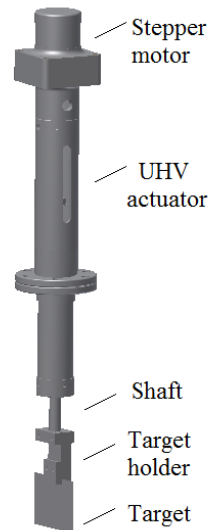
Figure 6.6: The ultra high vacuum actuator with the shaft, target holder, target and stepper motor attached.
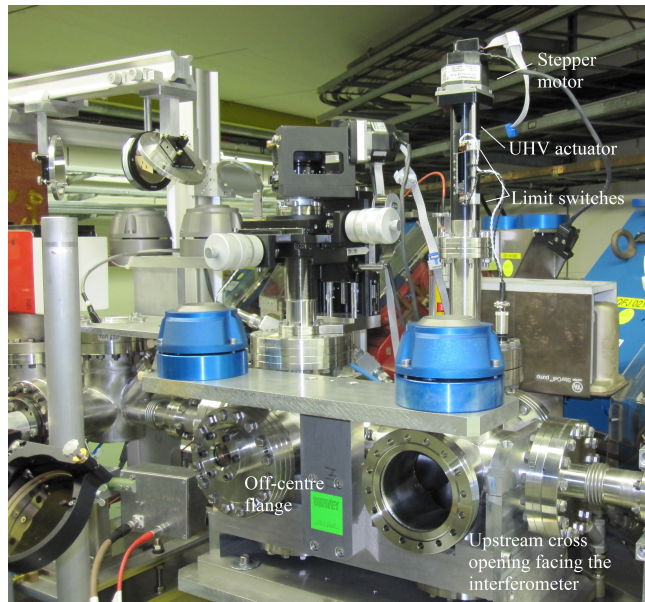
Figure 6.7: Installation of the second target. The coupled six-way crosses with the manipulators on top of them.

The upstream six-way cross openings on top and on the side facing the optical table

were opened. The assembly shown in figure 6.6 was placed on top of the upstream six-way cross. A quartz viewport was installed in the other opening and replaced a blank flange. Figure 6.7 demonstrates the experimental setup during the installation. The additional target was positioned at 45 deg. with respect to the beam propagation direction with the side coated with aluminium facing the downstream target to produce the FDR. Figure 6.8 demonstrates a newly installed target in the upstream cross, a reflected image of the downstream target on the surface of the upstream one is also visible.
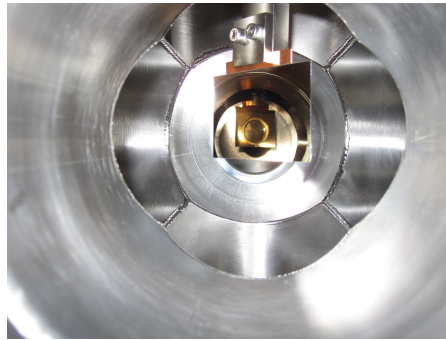
Figure 6.8: The second target installed in the upstream cross.

6.3.3 Interferometric system

The radiation originating from the targets is translated vertically by a periscope towards the optical table to avoid X-ray backgrounds from the horizontal beam plane. On the optical table a Michelson interferometer is installed (see figure 6.9). A reference working point is set at a height of 5 inch (127 mm) above the table surface.

On the optical table the translated signal is split into two polarisation components by the wire grid polariser which consists of 15 μm thick tungsten wires positioned with a spacing of 80 μm in a circular frame. The aperture of the polariser is 88 mm. The polariser allows the electric field $E_\perp$ perpendicular to the wires to be transmitted, while the field $E_\parallel$ parallel to the wires is reflected in the direction of a mirror reflection. Figure 6.10 demonstrates the transmission characteristic of the electric field component $E_\parallel$ parallel to the wires as a function of frequency [70]. It is clearly seen that the polariser separates $E_\perp$ and $E_\parallel$ very efficiently, especially for the frequencies below 100
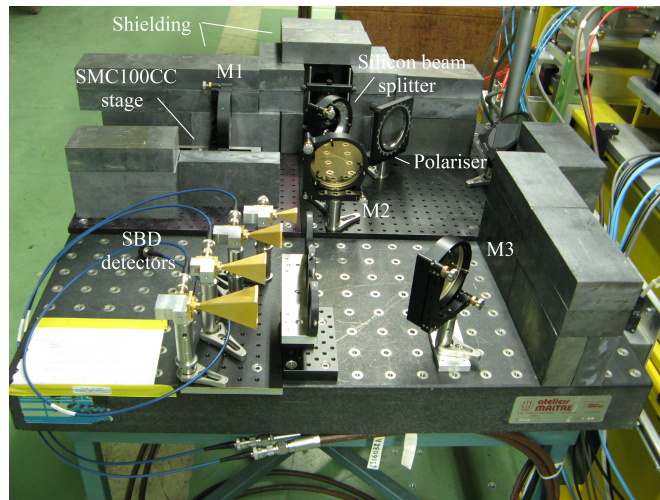
Figure 6.9: Interferometric system of the CDR setup at CTF3.

GHz. In the current configuration of the interferometric system the wires are positioned parallel to the surface of the optical table, so the vertical polarisation component of the radiation is transmitted towards the Michelson interferometer.
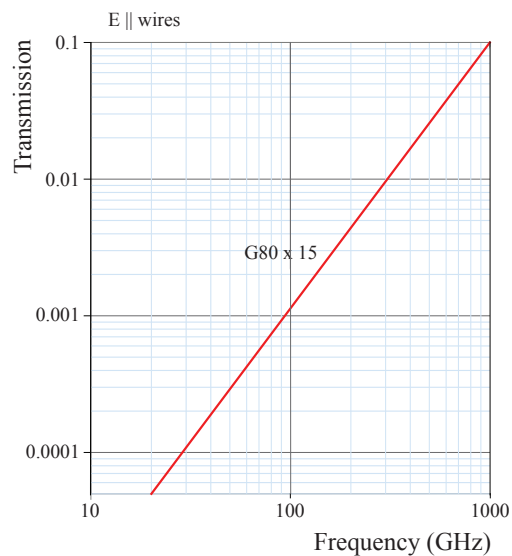
Figure 6.10: Transmission characteristic of the electric field component parallel to the wires in the polariser.

The mirrors used in the periscope as well as in the interferometer are 4 inch (101.6 mm) broadband aluminum coated mirrors (Melles Griot, PAV-PM-4050-C) mounted in suitable holders. Two axes of each mirror holder can be controlled with fine adjustment
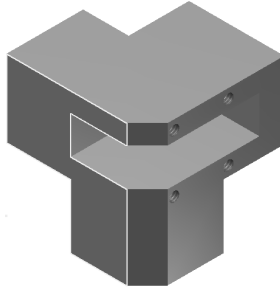
Figure 6.11: Holder for the DXP08 detector.

screws.

The movable mirror in the interferometer is translated by a linear stage (Newport Corp., UTS100CC). The stage provides a translation range of 100 mm, a minimum incremental motion of 0.3 μm and a resolution of 0.1 μm. It is powered and interfaced with a controller (Newport Corporation, SMC100CC) which is connected to the lab computer via an RS232 connection.

As a part of the upgrade process during 2010-2011 a silicon beam splitter (thickness of the wafer is 150 μm) was installed in the interferometer. It provided better efficiency in the mm wavelengths range than the Kapton and Mylar beam splitters which were in use before. In addition, a detector holder for the DXP08 Schottky diode was developed using Autodesk Inventor and manufactured at Royal Holloway Physics department workshop (see figure 6.11).

6.3.4 Detectors

The main properties of the Schottky barrier detectors used in the experiment are shown in table 6.1 [71]. They provide very compact and economical solution for a power detection in the frequency region of 40 to 140 GHz and have a flat frequency response for power levels below -10 dBm, as their sensitivity shows a minor variation over entire waveguide band.

Millitech DXP detectors utilise Metal-Induced Crystallisation (MIC) and Schottky Barrier technologies. MIC is based on the concept that crystallisation of some materials like Si or Ge is drastically reduced when they are put in contact with certain metals,

Detector	Freq. band	Freq. range [GHz]	Sensitivity [mV/mW] (min into 1 MΩ)
DXP-19	U-band	$40-60$	1000
DXP-15	V-band	$50-75$	850
DXP-12	E-band	$60-90$	700
DXP-08	F-band	$90-140$	300

Table 6.1: SBD detectors used in the experiment.

such as Al, Au, Ag or Ni. Schottky barrier is a rectifying junction that allows a current to flow only in one direction [72].

In order to understand the junction dynamics it is important to examine the energy-band diagram presented in figure 6.12 [72]. When a semiconductor material forms a crystal electrons in the atoms become restricted to the certain ranges of allowed energies, called the valence E_V and conduction E_C bands. These bands are separated by the Fermi energy level E_F at which the probability function of the electrons to conduct current in the crystal is equal to one half. The amount of the energy required for an electron to move from E_V to E_C depends on the temperature and the semiconductor doping profile. The whole diagram is referenced to the vacuum potential. The electron affinity ($q\chi$) is the energy required to remove an electron from the bottom of the conduction band up to the vacuum potential. Another important parameter in figure 6.12 is the metal work function (ϕ_m) which defines the energy required to remove an electron from the Fermi level up to the vacuum potential.

If the semiconductor Fermi level is greater than the metal Fermi level ($\chi + V_{CF} < \phi_m$), which is shown in figure 6.12(a), then electrons will diffuse from the semiconductor to the metal. As electrons are depleted from the semiconductor a positive charge is created in the semiconductor at the junction, therefore opposing a diffusion current. Figure 6.12(b) shows the junction at the equilibrium. The semiconductor energy bands bend in response to the described process, the bend is characterised by the built-in potential V_{bi}.

When a Schottky barrier is exposed to electromagnetic radiation, electrons cross the depletion barrier due to thermal activation in the barrier which is a dominant effect at the room temperature. A Schottky barrier diode provides an output voltage without needing any external DC bias and the detector response is proportional to the input
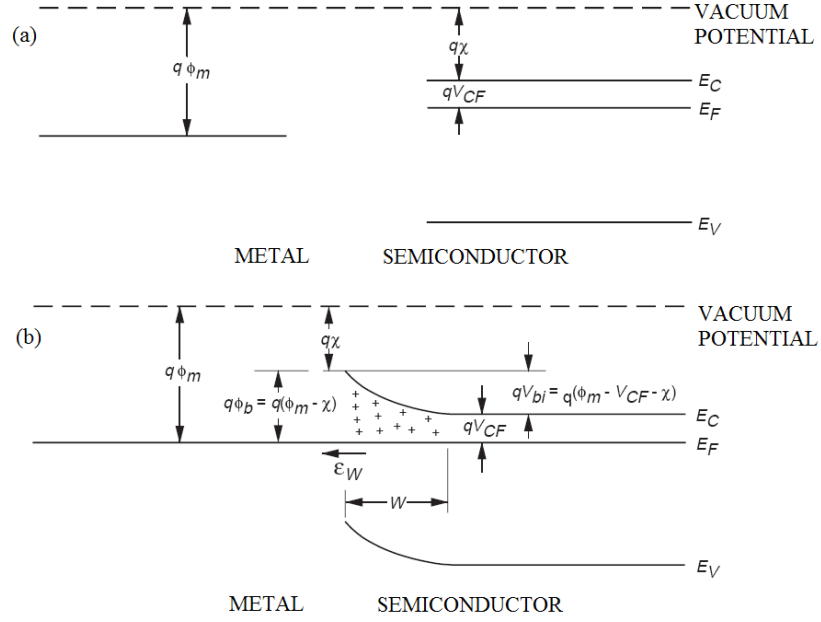
Figure 6.12: Energy-band diagram of Schottky junction.

radiation power. In [73] it was experimentally shown that an SBD detector response time of less than 1 ns can be achieved.

The SBD detectors in the experiment are coupled into waveguides. The radiation is concentrated by standard gain horn (SGH) antennas. Therefore the detectors are polarisation sensitive. A waveguide cut-off at low frequencies and a limited response at high frequencies reduce a bandwidth of this type of detectors.

6.3.5 Data acquisition and controls

In order to control all the hardware described in the previous sections a hardware control interface has to be established. There are two main locations for the CDR setup and controls at CTF3: the Delay Loop streak camera lab and the CRM line. In the streak camera lab all the control equipment is situated, including a DAQ computer, a BALDOR NextMove e100 motion controller and an Acqiris DC282 digitiser. The rest of the hardware was installed in the tunnel. In figure 6.13 a block diagram of the experimental setup is presented.

A translation stage SMC100CC in the interferometer is controlled by a single axis SMC100 controller which requires an RS232 connection to the DAQ computer. For the

stage controller at a baud rate of $96kBit/s$ the length of the cable connecting the stage and the DAQ computer is limited to a few meters. Since the distance between the lab and the setup is approximately 60 metres a serial-to-IP hub is used to connect the RS232 cable to the DAQ computer via an ethernet connection. The DAQ computer can access the controller, demand the position of the stage and read out the encoder for an accurate position of the mirror on the stage.
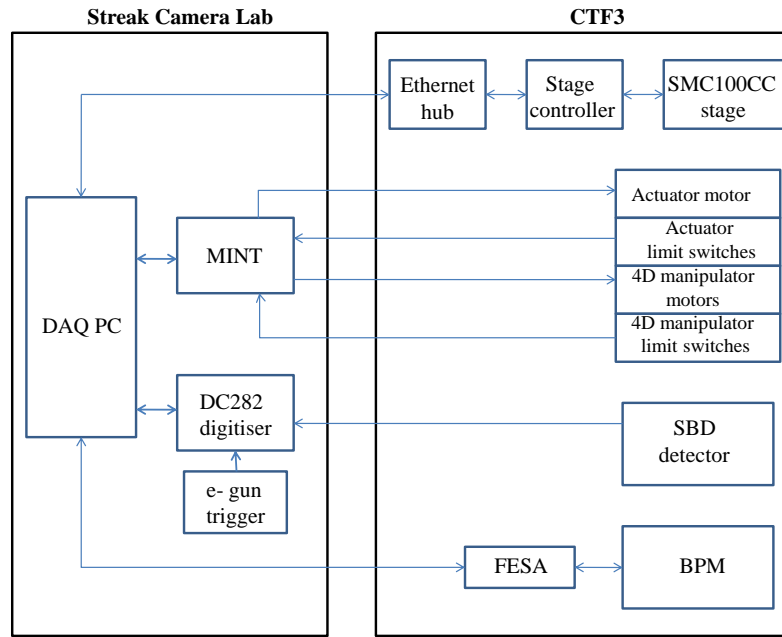
Figure 6.13: CDR experiment block diagram.

In order to control the position and orientation of the targets in the dual target configuration the motors of the UHV manipulators have to be monitored and encoders have to be read out. The translation and rotation of the downstream target and the translation of the upstream target are operated by the BALDOR NextMove e100 motion controller, which is connected to the DAQ computer and managed by a Motion INTelligence program (MINT). From the controller the cables for the power supplies, the encoders and limit switches are pulled into CTF3 to interface with the UHV manipulators. Multi-lead wires are used with 9, 15 and 23 pin connectors respectively.

Data acquisition is performed using a 10-bit Acqiris DC282 digitiser. The digitiser can provide four channel sampling at up to 2 GS/s or dual and single-channel sampling

at 4 Gs/s and 8 Gs/s respectively. In the experiment a 4Gs/s sampling for two channels is used. The input for an external trigger provides a precise synchronisation with the electron gun trigger. The data is read out at a frequency of 0.8 GHz for each bunch train and transferred to the digitiser through high quality RF cables.

BPM readings are acquired directly to the DAQ computer using a FESA class via the CERN technical network. The FESA is the so-called Front-End Software Architecture, it is developed by CERN to monitor and control all the devices at CTF3. The FESA class can be used to acquire readings from BPMs, klystrons, OTR screens etc. of the accelerator directly into the acquisition system of the DAQ computer. On the DAQ computer a LabVIEW program is run to control all the hardware in the experimental setup, it can also perform reading of the digitiser memory. Three major experimental scans were performed for the dual-target configuration of the targets: an interferometric scan, a rotation scan and a 2D scan. The logic of the scans is the following:

1. All the components are initialised: the DC282 digitiser is calibrated, the SMC100CC stage is reset and homed, the connections to the 4D manipulator of the downstream target and to the actuator of the upstream target are established.

2. Using the Motion INTelligence program (MINT) the targets are positioned in a certain way for each scan.

Interferometric scan is performed for the fixed vertical and rotational positions of both targets.

Rotational scan is performed for the fixed vertical positions of both targets, while the second (downstream) target is rotated.

2D scan is a sequence of the rotation scans taken for different impact parameters of the second target.

3. A delay time of the read out with respect to the trigger, a sampling interval (can be down to 0.25 ns) and a number of shots per acquisition have to be preset.

Interferometric scan: the initial point, incremental and travelling range of the movable mirror in the interferometer are preset. The scan is performed.

Rotational scan: the initial rotation, rotation increment and rotational range of the second target are preset. The scan is performed.

2D scan: the same as for the rotation scan, but additionally the initial translation

point, translation increment and translation range of the second target have to be preset. The first rotation scan starts at the initial rotation angle and the fixed impact parameter (translation) of the second target. Once the rotation scan is completed, the translation of the second target is changed to the next value resulting in the gradual increase of the second target impact parameter. The rotation scan is repeated, but now for the new value of the second target impact parameter. The process continues until the translation of the second target reaches the maximum value of the allowed travelling range.

4. While the scans are taken a preset number of shots per acquisition are recorded and the data are stored in a data file. For each shot the DAQ records a signal from the entire bunch train using a chosen SBD detector, BPM reading and the signals from other online monitors. Once the scan is completed, the data files are stored in a separate folder and ready for analysis. A number of data files equals to the number of acquisitions per scan.

5. In order to analyse the data a MatLab software package is used. Each file contains the signal shots, obtained from the detector in or beside the interferometer (other optional readings from online diagnostics tools, such as BPMs or RF pickups) and the information about the configuration of the setup at the time of the measurement: the second target rotation and translation, the first target translation, the number of shots per acquisition etc. The BPM and RF pickup readings are recorded for a further usage in data analysis.

For each scan an average integrated intensity per acquisition is obtained, an integration region of the signal can be chosen at different parts of the shot. The integration is performed for each shot of an acquisition and then averaged, therefore resulting in a data point for a position of the mirror in the interferometric scan, a rotation angle of the second target in the rotation scan, or a (rotation, translation) position of the second target in the 2D scan.

The same manipulations can be performed with any recorded signal, i.e. BPM or RF pickup readings.

Figure 6.14 shows a simplified graphical scheme of the interferometric, rotation and 2D scans. The blocks initialise; monitor and move; perform scan; acquire and save
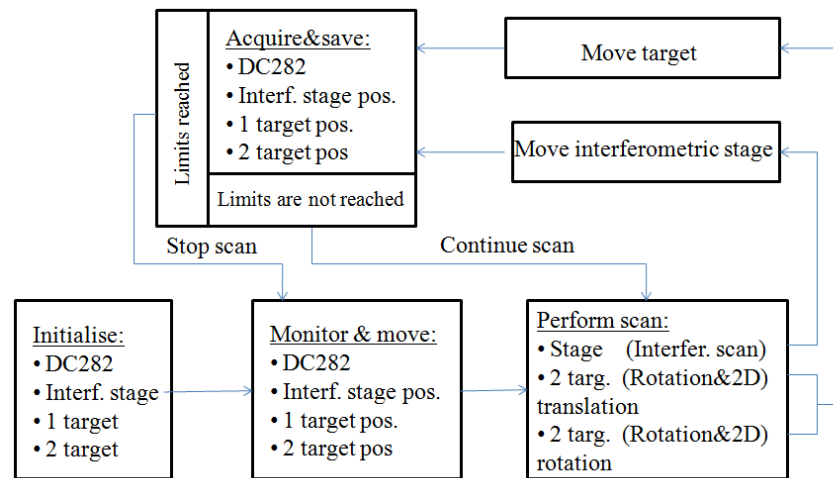
Figure 6.14: Scheme of the interferometric, rotation and 2D scans in LabVIEW.

correspond to the first four steps of the scan logic described above.

6.4 Summary

In this chapter a detailed description of the CDR experiment hardware and controls was given. The setup is located in the CRM line of the machine which allows for the CDR and CSR measurements to be taken. The location of the setup provided sufficient working space for the installation of the optical table and the interferometric system alongside the beam line.

The upgrade of the experimental setup was performed by the author of this thesis in 2010 - 2011. The second target with an UHV actuator was installed in the upstream cross and the interferometric system was modified.

The principles of DAQ at the experimental setup were discussed and the procedures of taking the interferometric, rotation and 2D scans were described. All the major hardware components were described as well and reasoning for their installation was explained.

Chapter 7

Experimental results

The major experimental results will be discussed in this chapter. In January 2011 during the winter shutdown at CTF3 a second target was installed in the experimental setup. By positioning an additional target upstream of the existing target, we anticipated to achieve a suppression of unwanted backgrounds.

Understanding of the CDR spatial distribution from the two targets is essential for achieving an optimal configuration of the experimental setup. When the second target was installed, it was important to find out how it would affect the final CDR distribution. Moreover, the theoretical calculations were performed in chapter 4 and a direct comparison of the experimental and the theoretical data can now be carried out. The measurements of the CDR spatial distributions as functions of the second target impact parameter and rotation for the two main configurations of the two-target system will be shown.

The coherent backgrounds originating upstream of the experimental setup, such as coherent Synchrotron Radiation and wakefields can significantly complicate experimental results interpretation. In order to investigate the ability of the upstream target to cut off the backgrounds, the measurements of the CSR reflection from the downstream target for four different positions of the upstream target will be presented in this chapter.

The ultimate goal of the experiment is to obtain the spectrum of the CDR from the two targets. In this chapter the interferometric measurements obtained at the

experimental setup will be shown. The corresponding spectra will be presented as well. The reproducibility of the measurements, the applicability of the measurements to a bunch profile reconstruction and the identified hardware constraints will be discussed. The bunch shape instabilities at CTF3 will be investigated and their influence on the measurements will be explained. Some experimental results which will be discussed in this chapter were published in [74, 75].

7.1 CDR spatial distributions

The CDR spatial distribution from the two targets was investigated theoretically in chapter 4. The CDR distributions as functions of the second target impact parameter and an angular (horizontal) coordinate at the observation plane were calculated for the two main configurations of the experiment. In the first configuration the impact parameter of the first target is 30 mm and the second target impact parameter is variable in the region of 10 to 30 mm. In the second configuration the first target impact parameter is 10 mm and, as in the first configuration, the second target impact parameter is variable in the region of 10 to 30 mm.

The developed theory should provide us with information on the main characteristics of the CDR spatial distribution. In the experimental setup the radiation distribution as a function of the second target impact parameter and rotation can be measured and then directly compared with the theoretically calculated distribution. This type of measurement was referred to as a 2D scan in chapter 6.

The detectors used for the 2D scans were DXP15 (50 - 75 GHz) and DXP12 (60 - 90 GHz). Depending on the polarisation component which was measured, a detector was either placed in the interferometer to measure the vertical polarisation of CDR or beside the interferometer to measure the horizontal polarisation.

Figure 7.1 demonstrates the vertical polarisation component of the CDR distribution measured using the DXP15 detector. The vertical and horizontal axes correspond to the second target rotation and translation respectively. The zero rotation corresponds to the mirror reflection angle from the second target. The first target is positioned 27mm away from the beam and the second target travelling range in the vertical

plane is from 7 to 23 mm away from the beam. The distribution data points were normalised by the current reading, obtained at the time of the measurement. The radiation distribution has a single mode shape, however the presence of the backgrounds distorting the shape of the distribution is clearly seen.

Figure 7.2 shows the vertical polarisation of the CDR for the second configuration of the targets, i.e. the first target is positioned 7 mm away from the beam and the second target travelling range in the vertical plane is from 7 to 23 mm away from the beam. For the second configuration a significant suppression of the integrated intensity is present due to a destructive interference between the targets and a suppression of the backgrounds by the upstream target.

Overall, figures 7.1 and 7.2 qualitatively agree with the theoretically calculated radiation distributions presented in chapter 4 (figures 4.16 and 4.17). The distributions have a single mode shape and the radiation suppression is present when the upstream target is positioned closer to the beam. The theoretical CDR distributions were calculated for the wavelength $\lambda = 5$ mm. The detectors have a flat frequency response in the wavelength regions 4 - 6 mm (DXP15) and 3.33 - 5 mm (DXP12). In the region 3.33 - 6 mm the CDR spatial distribution does not change significantly, therefore the radiation distribution calculated for $\lambda = 5$ mm can be used for a comparison with the experimental results.

Figure 7.1: The vertical polarisation of the CDR distribution measured using the DXP15 detector (50-75 GHz). The first target impact parameter $h_1 = 27$ mm.
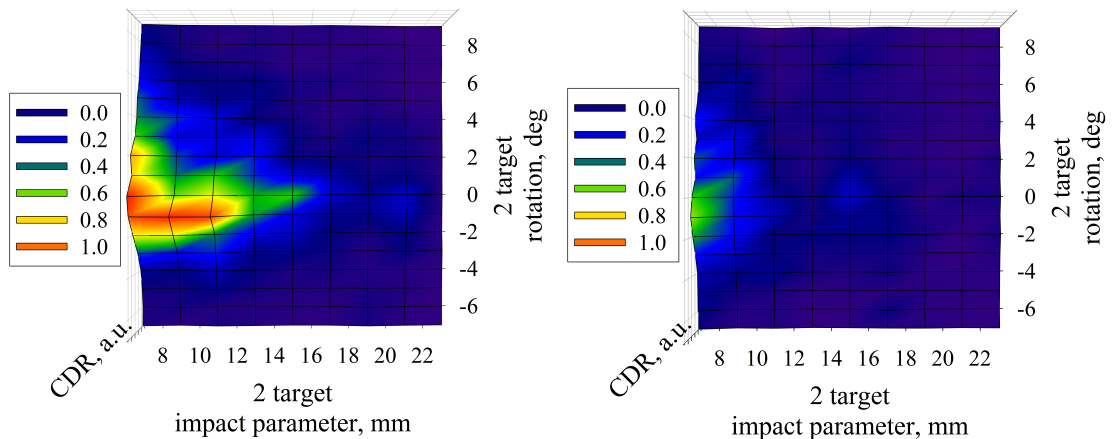
Figure 7.2: The vertical polarisation of CDR distribution measured using the DXP15 detector (50-75 GHz). The first target impact parameter $h_1 = 7$ mm.

In figures 7.3 and 7.4 the horizontal polarisation components of the CDR distribution are presented. Figure 7.3 demonstrates the distribution of the CDR when the first target is positioned 30mm away from the beam. A rough shape of the distribution suggests that it has a significant contribution of the coherent backgrounds. Figure 7.4 shows the radiation distribution when the first target is 7 mm away from the beam. In the latter case the radiation distribution is less distorted, which brings us to a conclusion that the upstream target effectively blocked the backgrounds generated upstream. For both figures 7.3 and 7.4 the second target travelling range was 7 to 25 mm away from the beam.

According to the theoretical calculations the horizontal polarisation component should have a dual mode shape with a minimum at a mirror reflection angle (see chapter 4, figures 4.18 and 4.19). In the theoretical calculations the radiation intensity is also not gradually reduced for the second configuration of the targets, but it is modulated as a function of wavelength. Similar behavior is seen in figures 7.3 and 7.4. One may notice a peak-to-peak asymmetry which was not predicted by the theoretical model. This asymmetry can be caused by the fact that the targets are tilted with respect to each other. Since the targets are also close together, the destructive interference can be a source of the observed asymmetry. The vertical polarisation should not be affected as much as the horizontal, because it is perpendicular to the plane of incidence. Nevertheless, additional theoretical studies are necessary.

One may be interested in how the distributions will change if measured by the detectors sensitive to lower or higher frequencies. DXP12 sensitive to 60-90 GHz is another detector which was used in the experiment. Figures 7.5 and 7.6 show the vertical polarisation of CDR measured by this detector. For the figure on the left the first target is 27 mm away from the beam (the first configuration) and for the figure on the right (the second configuration) the first target is 7 mm away from the beam. The second target impact parameter is changing in the region of 7 to 25 mm. For the second configuration of the targets the radiation is suppressed due to the destructive interference between them. It is worth noting that the spatial distribution in figure 7.5 is less distorted than in figure 7.1, which might be due to the milder background conditions in this wavelength range and better beam stability at the time of the measurement. A

Figure 7.3: The horizontal polarisation of the CDR distribution measured using the DXP15 detector (50-75 GHz). The first target impact parameter $h_1 = 30$ mm.

Figure 7.4: The horizontal polarisation of the CDR distribution measured using the DXP15 detector (50-75 GHz). The first target impact parameter $h_1 = 7$ mm.

general agreement of the measured vertical polarisation of the CDR with the theoretical calculations can be confirmed.

Figure 7.5: The vertical polarisation of the CDR distribution measured using the DXP12 detector (60-90 GHz). The first target impact parameter $h_1 = 27$ mm.

Figure 7.6: The vertical polarisation of CDR distribution measured using the DXP12 detector (60-90 GHz). The first target impact parameter $h_1 = 7$ mm.

The horizontal polarisations of CDR measured with the DXP12 detector are shown in figures 7.7 and 7.8. For figure 7.7 the first target impact parameter is 24 mm, for figure 7.8 the first target impact parameter is 10 mm. The destructive interference is observed for the second configurations of the targets, the minimum of the radiation intensity at the mirror reflection angle is also visible. The peak-to-peak asymmetry

121

is observed again. The distribution in figure 7.7 is more dispersed than in figure 7.8, which is caused by the coherent backgrounds not blocked by the upstream target at its furthest position from the beam.
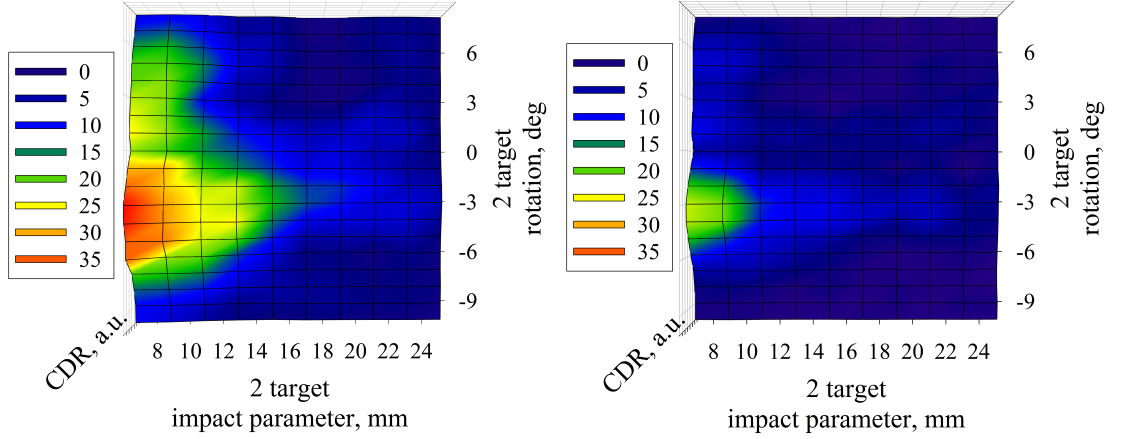
Figure 7.7: The horizontal polarisation of the CDR distribution measured using the DXP12 detector (60-90 GHz). The first target impact parameter $h_1 = 24$ mm.
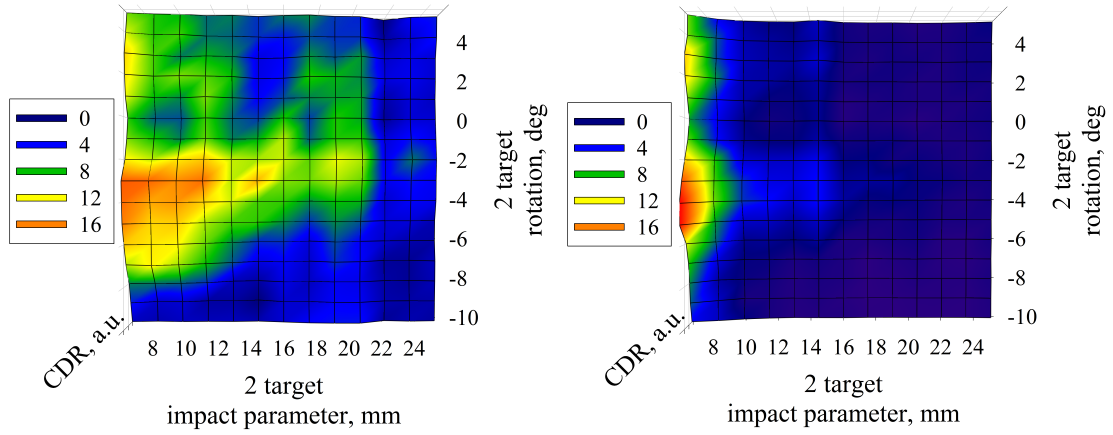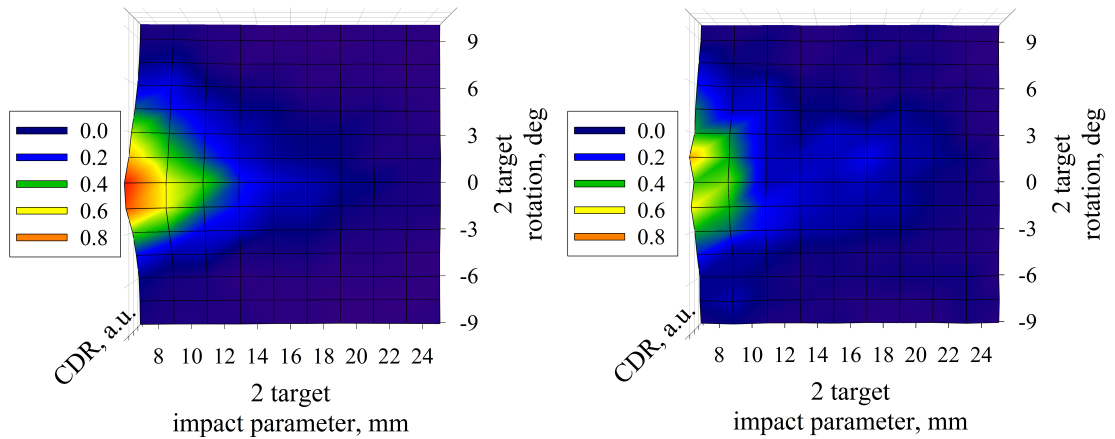
Figure 7.8: The horizontal polarisation of the CDR distribution measured using the DXP12 detector (60-90 GHz). The first target impact parameter $h_1 = 10$ mm.

The presented distributions showed the geometry of the detected radiation as a function of two coordinates. It was very useful geometry for understanding of the shape of the radiation distributions and the investigation of backgrounds suppression by the first target. Now we shall concentrate on the properties of the CDR intensity as a function of the second target rotation, which is correlated with the CDR angular distribution. The presented 2D scans are used in this analysis, but we take a "slice" of a scan corresponding to the second target impact parameter $h_2 = 7$ mm. The values of the measured radiation intensity are normalised by the maximum value and the errors are calculated as standard deviations of the integrated intensity per acquisition (several shots per acquisition are taken).

A theoretical dependence can also be calculated for each experimental curve. We assumed that two detectors, DXP12 and DXP15, have a flat response in the wavelength ranges 3.33 - 5 mm and 4 - 6 mm respectively. The vertical and horizontal polarisation components of the CDR do not charge dramatically in these wavelengths regions. Therefore in order to plot a theoretical curve for each detector the central wavelengths of the mentioned regions were chosen, i.e. $\lambda = 4.15$ mm for the DXP15 detector and

$\lambda = 5$ mm for the DXP12 detector. The theoretical distributions of the CDR intensity are calculated as functions of the horizontal (angular) coordinate η on the observation plane, while the vertical coordinate ξ is fixed at the value corresponding to the maximum radiation intensity in that plane. The distributions are calculated for the two main configurations of the targets, corresponding to the following relations between the target impact parameters h1 and h2: for the first configuration h1 > h2 and for the second configuration h1 $\simeq$ h2 (please note that now both targets are at fixed positions). The conversion of the horizontal coordinate on the observation plane into the angular coordinate is performed in the following way:

$$\alpha = tan^{-1}\left(\frac{\eta}{a}\right)\frac{180}{\pi}, \tag{7.1}$$

where a is the distance from the second target to the observation plane.

Figure 7.9: The rotation scan of the vertical polarisation of CDR performed using DXP15 detector for the first configuration of the targets. The dashed line: theoretical distribution calculated for $\lambda = 4.15$ mm.
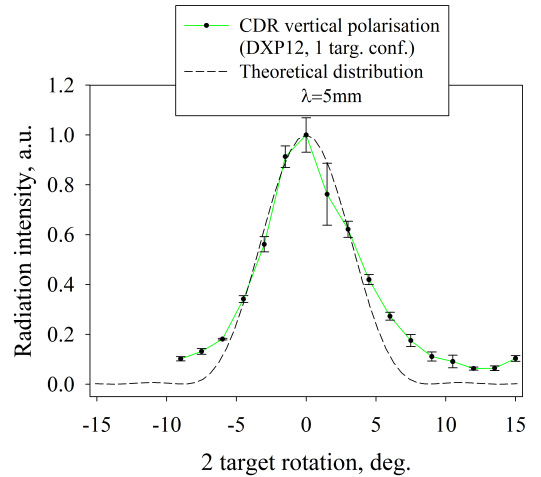
Figure 7.10: The rotation scan of the vertical polarisation of CDR performed using DXP15 detector for the first configuration of the targets. The dashed line: theoretical distribution calculated for $\lambda = 5$ mm.

Figure 7.9 demonstrates the rotation scan of the vertical polarisation component of CDR measured using DXP15 detector for the first configuration of the targets. The second target impact parameter is fixed at 7 mm from the beam. The dashed line is the theoretical radiation distribution calculated for $\lambda = 4.15$ mm. The points represent the experimentally measured dependence. Both dependencies were normalised to the

maximum values for a qualitative comparison. Large error bars at some rotation angles might be due to the abrupt changes in the machine behavior during the scan.

A similar rotation scan, but measured using DXP12 detector, is presented in figure 7.10. The background level is more clear for this measurement. The theoretical distribution is calculated for $\lambda = 5$ mm. Both experimental distributions, in figures 7.9 and 7.10, qualitatively agree with the theory.

Figure 7.11 and 7.12 demonstrate the rotation scans of the vertical polarisation component of CDR measured using DXP15 and DXP12 detectors, but now for the second configuration of the targets when both of them are positioned at the same distance from the beam. There are some aspects here that are worth mentioning. The distribution becomes broader when the first target is fully inserted, because of the destructive interference. Coming back to the 2D distributions, in figure 7.1 it is clearly seen that the coherent radiation background distorts the CDR spatial distribution. The CDR photon yield depends exponentially on the impact parameter. When the second target is fully inserted, the CDR contribution is dominant, which is confirmed by a good consistency of the theoretical and experimental distribution shapes.
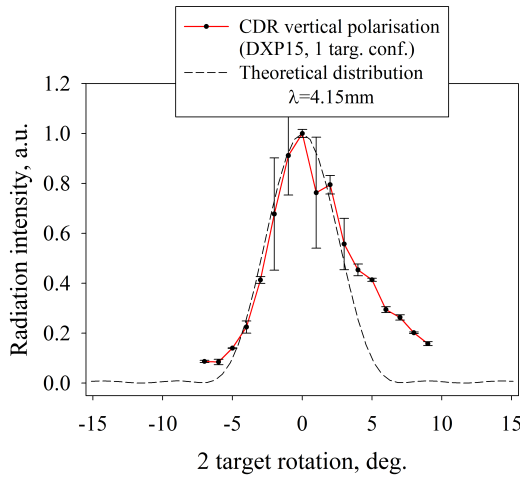
Figure 7.11: The rotation scan of the vertical polarisation of CDR performed using DXP15 detector for the second configuration of the targets. The dashed line: theoretical distribution calculated for $\lambda = 4.15$ mm.

Figure 7.12: The rotation scan of the vertical polarisation of CDR performed using DXP15 detector for the second configuration of the targets. The dashed line: theoretical distribution calculated for $\lambda = 5$ mm.
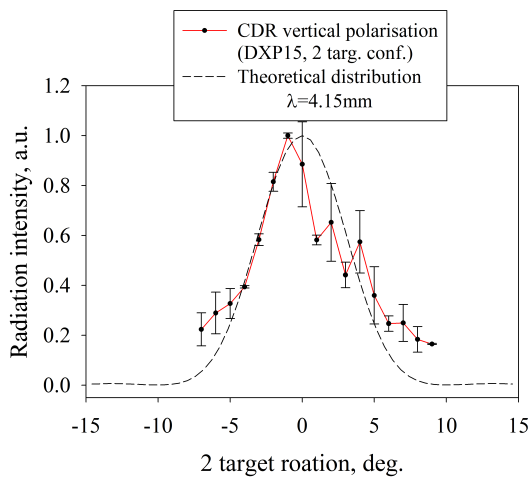
Now we shall consider the horizontal polarisation component of the CDR from the

dual-target system. The second target impact parameter is $h_2 = 7$ mm. Figure 7.13 shows the rotation scan of the horizontal polarisation of CDR measured using DXP15 detector for the first configuration of the setup, i.e. the upstream target is positioned far from the beam and its influence on the distributions is minimal, however the backgrounds generated upstream are present. A similar scan, but taken using DXP12 detector is shown in figure 7.14.

Figure 7.13: The rotation scan of the horizontal polarisation of CDR performed using DXP15 detector for the first configuration of the targets. The dashed line: theoretical distribution calculated for $\lambda = 4.15$ mm.

Figure 7.14: The rotation scan of the horizontal polarisation of CDR performed using DXP12 detector for the first configuration of the targets. The dashed line: theoretical distribution calculated for $\lambda = 5$ mm.

It is seen straight away that the background pedestal is very high, which is caused not only by the inability to block the backgrounds coming from the upstream of the experimental setup, such as CSR and wakefields, but also by the fact that the horizontal polarisation component of CDR is less intense than the vertical one (approximately factor 5, see chapter 4). One should also note that for the CSR the horizontal polarisation component is much larger than the vertical one, therefore it can significantly contribute in the radiation distributions in figures 7.13 and 7.14.

Figure 7.15 and 7.16 demonstrate the distributions of the horizontal polarisation of CDR measured with DXP15 and DXP12 detectors for the second configuration of the targets, i.e. both targets are roughly at the same distance from the beam. In this configuration of the targets the maximum suppression of the backgrounds is achieved.

Moreover, it was studied in chapter 4 that despite the destructive interference the intensity of the horizontal polarisation does not drop as fast as the vertical polarisation, but it is modulated as a function of wavelength. The horizontal component becomes approximately two times less than the vertical polarisation component for the second configuration, compared to the factor five for the first configuration. Together with the background suppression by the first target, it results in the lower background level than in figures 7.13 and 7.14.
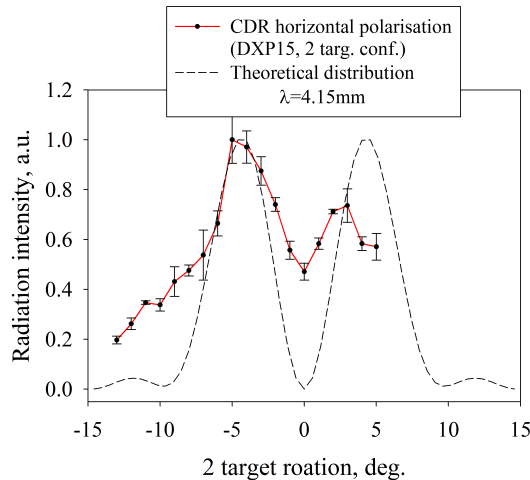
Figure 7.15: The rotation scan of the horizontal polarisation of CDR performed using DXP15 detector for the second configuration of the targets. The dashed line: theoretical distribution calculated for $\lambda = 4.15$ mm.
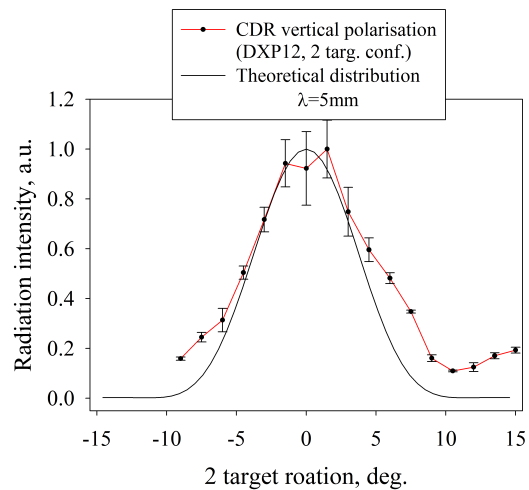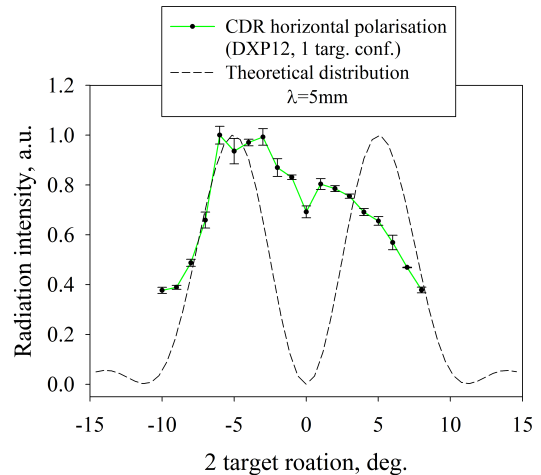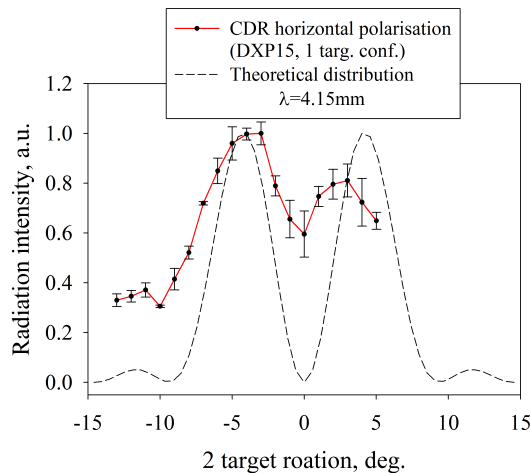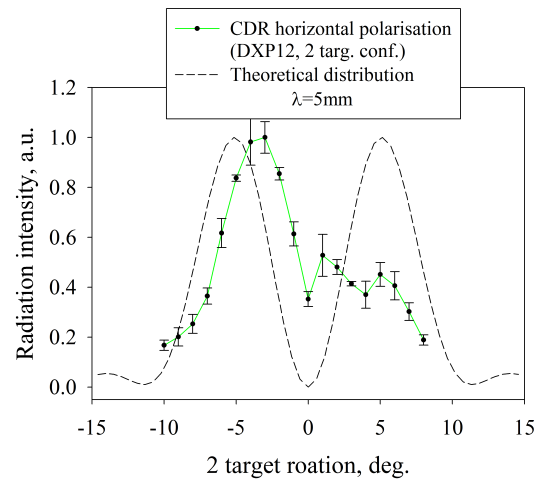
Figure 7.16: The rotation scan of the horizontal polarisation of CDR performed using DXP12 detector for the second configuration of the targets. The dashed line: theoretical distribution calculated for $\lambda = 5$ mm.

For figure 7.16 the similar discrepancies with the theoretical curves are present as in figures 7.13 and 7.14, but it is worth mentioning that because of the lower background pedestal the peaks are more clearly visible and the intensity minimum at the mirror reflection is deeper. However one may notice that the experimental peaks are shifted toward the mirror reflection angle. This most likely signifies that the spectrum of the detected radiation is shifted towards higher frequencies, which change the distribution in a way that the distance between the peaks of the radiation intensity is reduced.

One should point out that the dual-target system does not cut off the coherent backgrounds completely. The horizontal polarisation component of CSR is much larger than the vertical one. Some part of this radiation might diffract around the first

target or reflect from the vacuum chamber and find its way into the detector. It might partially explain the discrepancies between the experiment and the theory, including the peak-to-peak asymmetry. Additional experimental studies are necessary in order to investigate this further.

7.2 Measurements of the CSR propagation in the CRM line

The suppression of the backgrounds originating upstream of the experimental setup was one of the main motivations for the installation of the additional target. As was discussed in chapter 6, the location of the experimental setup allows for the measurements of the CSR coming from the bending magnet at the entrance to the CRM line. When it is switched on, the beam is circulated in the Combiner Ring generating the CSR, the reflection of which from the second target can be measured by the same detection system on the optical table as for CDR.

In order to test the ability of the first target to cut-off the backgrounds, the dedicated measurements of the CSR reflection from the second target were performed. The main idea of a CSR scan is to measure the radiation intensity as a function of the second target rotation, while the upstream target is positioned either in the centre of the six way cross or as far as possible from the centre. In addition to the rotation scan, a 2D scan of the CSR reflection can be performed as well, which is just a combination of the rotation scans for different positions of the upstream target.

In figures 7.17 and 7.18 the scans of the horizontal polarisation of the CSR reflection from the second target as functions of the second target impact parameter and rotation are shown. The measurements were performed using the DXP15 detector. In figure 7.17 the first target is positioned 27mm away from the centre of the upstream six-way cross and the second target translation range is 15mm with the lowest point at the centre of the downstream six-way cross. Figure 7.18 demonstrates the maximum cut-off of the backgrounds coming from the upstream by positioning the first target in the centre of the beam pipe. The CSR suppression by approximately a factor of 5 is achieved.

In order to study a trend in the background suppression with respect to the different
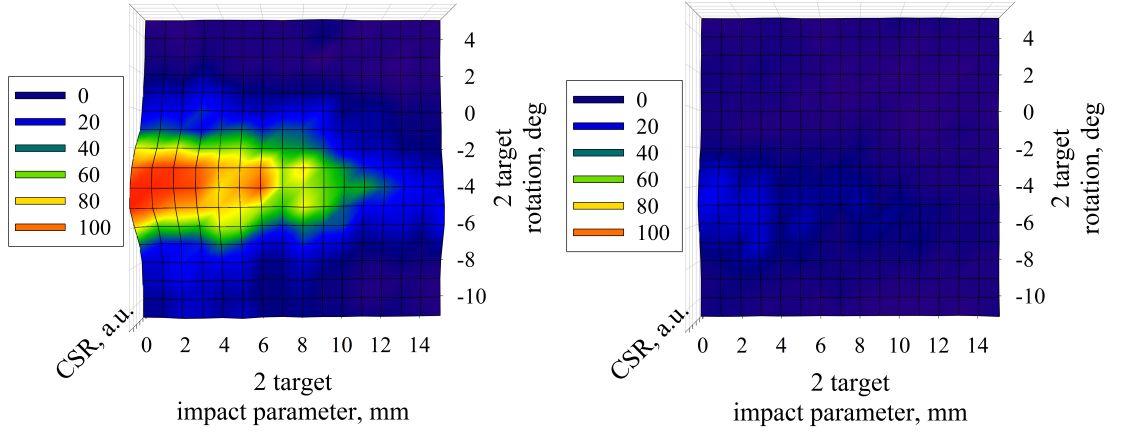
Figure 7.17: The horizontal polarisation of the CSR distribution measured using the DXP15 detector (50-75 GHz). The first target impact parameter is $h_1 = 27$ mm.

Figure 7.18: The horizontal polarisation of the CSR distribution measured using the DXP15 detector (50-75 GHz). The first target is in the centre of the six-way cross.

positions of the upstream target in the beam pipe, four rotation scans were performed (see figure 7.19). The scans were taken over 16 degrees of the second target rotation, the horizontal polarisation of the radiation was measured by the DXP15 detector. The data were normalised by the current. The red curve in figure 7.19 corresponds to the following configuration of the targets: the first target is at 30 mm from the centre of the upstream cross, the second target is in the centre of the downstream cross. The green curve corresponds to the configuration when both targets are in the centre of the six-way crosses and the maximum suppression of the CSR should be achieved. The blue and the black curves show the detected CSR when the first target is 10 and 20 mm away from the centre respectively. It is seen that a gradual insertion of the upstream target into the six-way cross allows for a significant suppression of the CSR. However, the green curve shows that some radiation is still detected even though the upstream target is right in the centre of the beam pipe, which is most likely due to the residual reflections in the coupled six-way crosses. This remaining part might cause distortions of the CDR pattern and is yet to be understood.
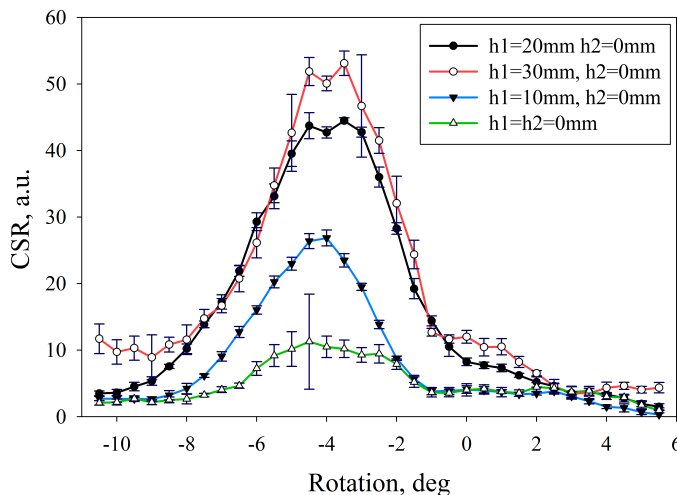
Figure 7.19: The CSR rotation scans for the four different configurations of the experimental setup.

7.3 Interferometric measurements

The ultimate goal of the CDR experiment is to measure the spectrum of the CDR. One of the ways to do that is to use an interferometer based system. The spectrum can be then used to calculate the bunch form-factor. More information on the longitudinal profile reconstruction procedure was presented in chapter 5, section 5.3.

In this section the interferometric measurements taken by the Michelson interferometer using two different SBD detectors will be discussed. Once an interferometric measurement is performed, a Fourier transform can be applied to obtain the spectrum of the detected radiation. The obtained spectra have to be assessed from the point of view of their applicability to longitudinal parameters reconstruction.

The time required to record an interferogram at the experimental setup is relatively long, therefore the measurement is subject to the machine drifts which affect its quality, e.g. changes of the bunch shape in time. These effects will be discussed in this chapter.

Figure 7.20 demonstrates a sample interferogram, measured by the DXP15 detector for the second configuration of the targets (both targets are positioned 7mm away from the beam). The interferogram has a clearly defined central peak and the central part of the interferogram is not symmetric, which can be explained by the machine drifts and bunch shape instabilities that will be discussed in detail in section 7.4. The theo-

retical interferogram for 50 - 75 GHz polychromatic source was calculated in chapter 5, section 5.1. One may notice that the interferogram in figure 7.20 differs from the theoretically calculated one, therefore a spectral analysis of the frequencies contributing in the measurement shall be performed.
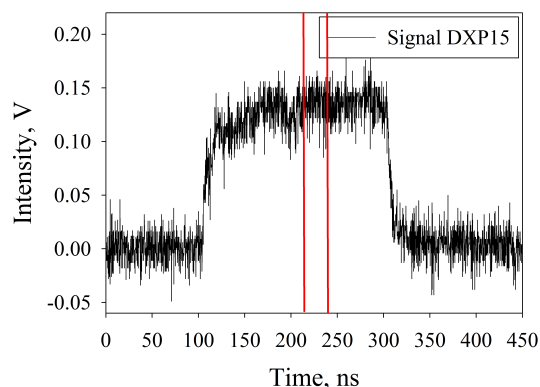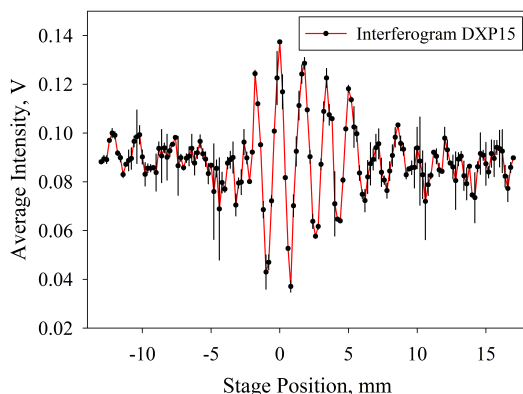
Figure 7.20: The interferogram measured by DXP15 for the following configuration of the targets: $h_1 = h_2 = 7$ mm.

Figure 7.21: A sample signal from the DXP15 detector with the marked integration region.

A sample signal from the detector with the marked integration region is shown in figure 7.21, the length of the entire pulse is approximately 200 ns and the width of the integration region is 25 ns. It is chosen to be very narrow to minimise the effect of the signal variation along the pulse.

In order to calculate the spectrum from the presented interferometric measurement, a Fourier transform has to be applied. The mirror travelling range of $x = 30$ mm yields the maximum path difference of $z = 2x = 60$ mm. The corresponding time delay in the Michelson interferometer is $T = z/c = 200$ ps. The resolution of the interferometric measurement is defined by the maximum path difference z in the following way: $\delta = 1/z = 0.017$ mm^{-1}. The resolution of the corresponding spectrum is $\delta_S = 1/T = 5$ GHz. Theoretically this gives 5 data points in the region of 50 - 75 GHz, where the DXP15 detector demonstrates a flat frequency response. A pyramidal horn antenna coupled to the detector gives a low frequency cut-off at 50 GHz.

The spectrum corresponding to the interferometric measurement is shown in figure 7.22. The low frequency cut-off at 50 GHz is marked with the red line. Figure 7.22 demonstrates that the spectrum of the detected radiation is rather narrow and shifted
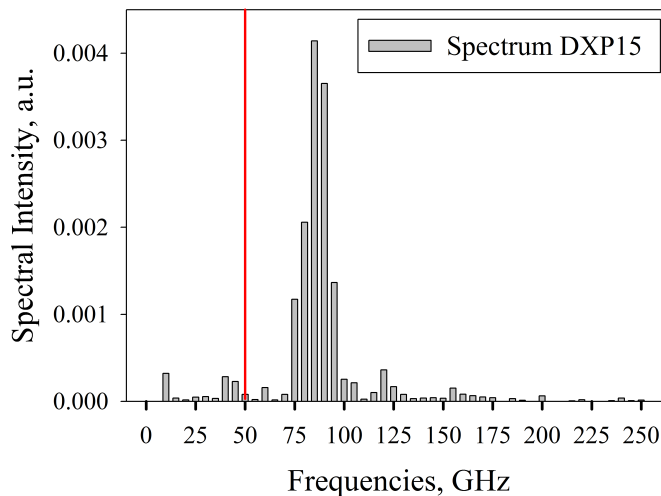
Figure 7.22: Spectrum obtained from the interferogram in figure 7.20

towards the higher frequency in the region of 75 to 100 GHz. This measurement cannot be used directly for the bunch form factor reconstruction as the response function of the detector is not known between 75 and 100 GHz. More data point have to obtained towards the lower and higher frequencies to have sufficiently large spectral coverage. Despite the fact that several SBD detectors are installed at the experimental setup, in the current configuration only one at a time can be used for the interferometric measurements. Processing of the measurements taken at different times and using different detectors is potentially very challenging task due to the changing machine parameters. In addition, the sensitivity range of the detectors in use is not known precisely.

The presented spectral measurement was performed for the targets positioned at the same distance from the beam, therefore providing the maximum suppression of the backgrounds originating upstream. In order to test the reproducibility of the interferometric measurement shown in figure 7.20, another measurement using the same DXP15 detector, but now for the first configuration of the setup was performed ($h_1 = 27$ mm; $h_2 = 7$ mm).

The scan was taken over the 30 mm of the stage travelling range. Three shots per position of the mirror were acquired. The measured interferogram is shown in figure 7.23. It is seen that the interferogram obtained in the latter case is more noisy and

also asymmetric, however a central peak of the interferogram is clearly visible. In the figure 7.23 when the stage position reaches, for instance 11 and 14 mm, abrupt changes of the detected radiation intensity are observed, which are clearly not interferometric effects. The cause of these changes in the measured intensity of the CDR will be discussed later on in section 7.4.
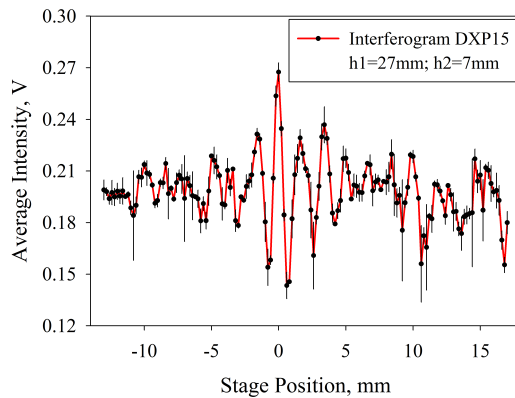
Figure 7.23: The interferogram measured by DXP15 for the following configuration of the targets: $h_1 = 27$ mm; $h_2 = 7$ mm.
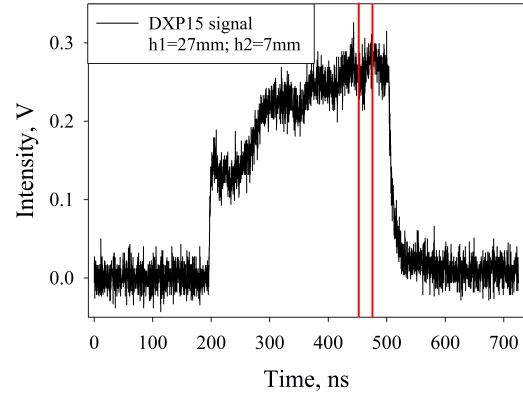
Figure 7.24: A sample signal from the DXP15 detector with the marked integration region for the following configuration of the targets: $h_1 = 27$ mm; $h_2 = 7$ mm.

A sample signal obtained from the DXP 15 detector, which was used in the latter interferometric measurement, is shown in figure 7.24. The region confined within the red lines is the integration region which was used to plot the interferogram. The signal is not flat and a significant variation of the radiation intensity along the pulse is visible. Further in this chapter it will be also proven that the signal is not stable from shot to shot, resulting in the changing time profile of the signal. Coming back to the integration region, the main criterion for choosing it, is finding the part of the pulse which is less sensitive to the bunch shape variation. Another criterion is that the shorter the region of integration the less the contribution of the changing time profile of the pulse in the measurement.

The spectrum of the CDR obtained from the interferogram in figure 7.23 is presented in figure 7.25, the low frequency cut-off is marked by the red line. The spectrum is more noisy compared to the one in figure 7.22, which is caused by the severe variation of the radiation intensity along the pulse. Once the spectra from the presented measurements

132
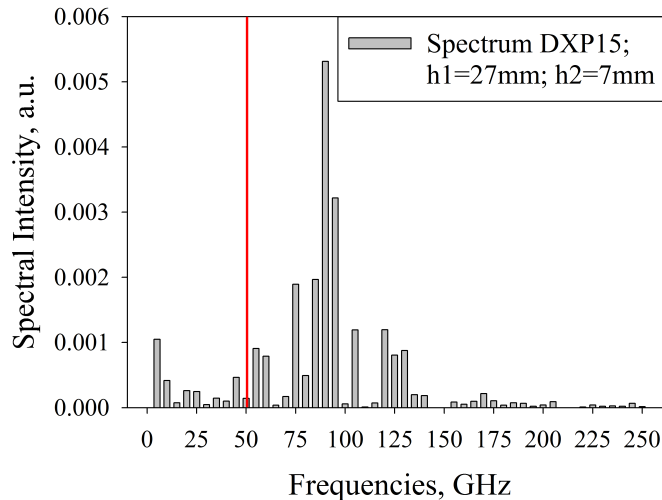
Figure 7.25: The spectrum obtained from the interferogram in figure 7.23.

are compared, one may conclude that the general characteristics of the spectrum of CDR are reproducible, i.e. the spectra in both cases are narrow band and shifted towards the higher frequencies. However the detailed features of the spectra change from measurement to measurement.

7.4 Bunch shape instability studies

A bunch length stability along the pulse is a key to successful spectral measurements. When a bunch length varies along the pulse the Coherent Diffraction Radiation is generated with different wavelengths from different parts of the pulse, therefore complicating the analysis. An additional problematic issue is the instability of the bunch shape. At CTF3 bunch length manipulations are performed before the beam is injected into the delay loop and the combiner ring and after it is extracted from them. In the linac section of CTF3 the bunch length is in the region of 1 - 7 ps, then the beam is directed through the stretching chicane (known as a Frascati chicane) where the bunches are stretched up to 15 - 20 ps to achieve an effective recombination in the rings. Later on the bunches are shortened to 1 - 2 ps to achieve an effective RF transfer in the PETS. When the beam goes through the Frascati chicane the bunches can become distorted and micro-bunching structures can occur, which results in distortion of the

133

signals obtained using the SBD detectors.

At CTF3 we can use the SBD detectors to perform a real-time bunch length monitoring throughout the train. There is also RF - pickup hardware, which is installed in the Transfer Line 1 of CTF3 and consists of a single WR28 waveguide pickup attached to the beam pipe and separated by a thin vacuum window. The beam induced fields flow to the detector box placed on the girder of the machine where they are transmitted via a pyramidal horn antenna (see figure 7.26) [15]. The emitting and receiving antennas are insulated from one another and their separation is calibrated for the required attenuation. The power is detected by the SBD detector sensitive in the frequency region of 26.5 - 40 GHz. There are five RF-pickups installed at different locations of the CTF3 to provide a real time monitoring of the longitudinal parameters of the beam before and after the bunch manipulation chicanes.
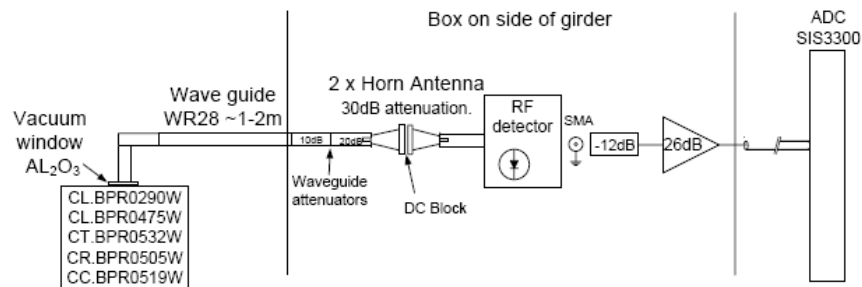
Figure 7.26: Schematic layout of the BPR waveguide pickup.

In order to understand which factors affect the quality of the interferometric measurements, an additional interferometric scan was taken using DXP12 detector with a flat frequency response in the region of 60 - 90 GHz. The scan was taken following the standard procedure for the interferometric measurement, however in addition to the signal from the detector and the current reading from the BPM0195S, the signal from the RF-pickup (BPR0532W) located at the beginning of the CTF3 Transfer Line 1 after the Frascati chicane was also recorded for each acquisition.

The reason why these additional measurements are interesting is that they serve us as a direct representation of a long-term machine stability in terms of a bunch length variation. The BPR measures power in the 26.5 - 40 GHz region of frequencies,

this corresponds to the wavelengths of 7.5 - 11 mm or 25 - 38 ps. From this simple estimation we can conclude that only the major changes in the bunch length or shape will be detected by this instrument. Nevertheless, by measuring the integrated power in this region as a function of the time during the one interferometric scan, one may obtain the information demonstrating whether the longitudinal characteristics of the beam were changing in time or not. The interferometric measurement is shown in figure 7.27.
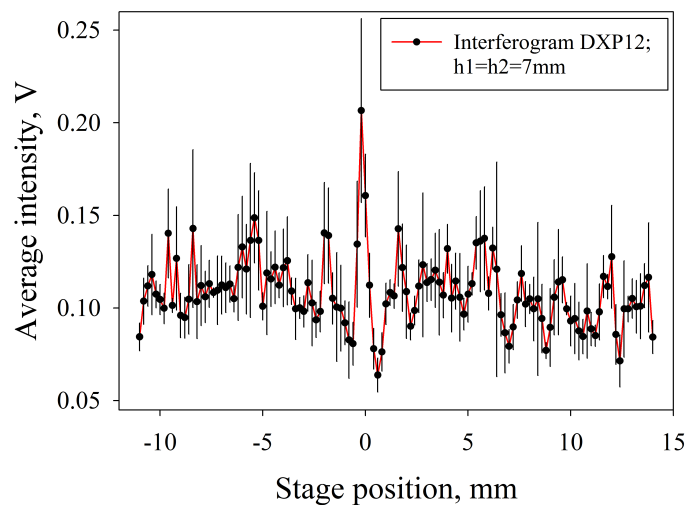
Figure 7.27: The interferogram measured by DXP12 for the following configuration of the targets: $h_1 = 7$ mm; $h_2 = 7$ mm.

The scan was taken over 25 mm of the movable mirror travelling range, seven shots for each signal were acquired per mirror position. The readings from the three instruments were recorded, i.e. the DXP12 signal, the reading of the integrated power from BPR0532W and the current reading from BPM0195S. The DXP12 signal is used for the interferometric measurement, the BPR0532W signal is used for bunch length variation monitoring, and the current reading for the current stability evaluation as well as for a qualitative comparison with the other signals.

The measurement demonstrates a clear central peak with the factor two increase of the maximum measured intensity, the peak is located at exactly the same mirror position, corresponding to a zero path difference, as in figures 7.20 and 7.23. In fig-

135

ure 7.28 the signals from the the DXP12 detector sensitive between 60 and 90 GHz and the waveguide pick-up are presented. The region within the dashed red lines is the integration region for the interferometric measurement. The shape of the signal represents the CDR intensity generated from different parts of the pulse. If the bunch length and shape do not change significantly throughout the bunch train, the detected intensity should be relatively constant throughout the pulse, however this is not the case for this measurement.
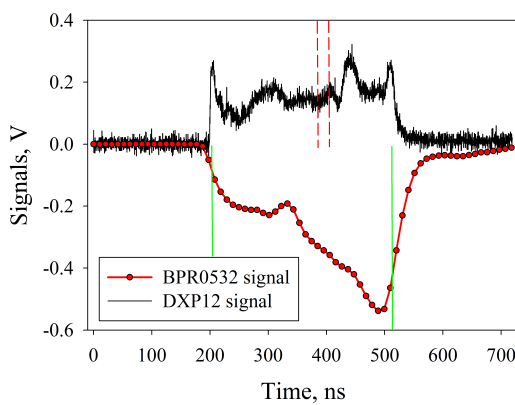
Figure 7.28: The signals from the DXP12 detector, and the BPR located in the CTF3 Transfer Line 1.
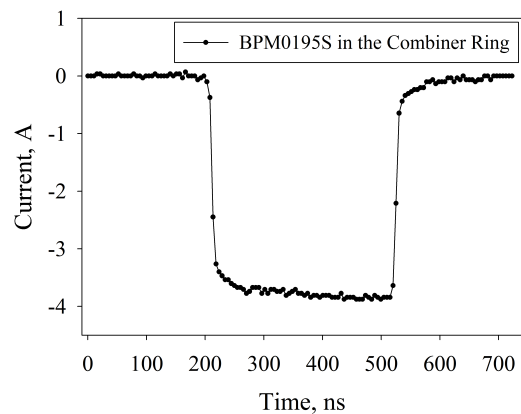
Figure 7.29: A sample current reading taken while recording the interferogram in figure 7.27.

A significant variation of the longitudinal parameters of the bunches along the train is detected despite of the fact that the current is flat (see figure 7.29). Both diagnostics (BPR0532W and DXP12) are positioned after the Frascati chicane which could be the source of the problem. It is important to mention here that the signals from the RF-pickups in the linac before the chicane demonstrate flatter signals. In the chicane the bunches can be stretched or shortened by varying the phase of the accelerating RF. Depending on whether the electron bunch is accelerated on crest, the rising or falling edge, the bunch length is changed differently. If the head of the bunch experiences a smaller accelerating gradient than the tail, the bunch is compressed. If the head is under the higher accelerating gradient than the tail, the bunch is stretched. Various effects such as wakefields might introduce irregularities in the longitudinal charge distribution during the stretching of shortening of the bunch, which are also known as micro-bunch

instabilities.

The patterns observed with DXP12 and BPR0532W (figure 7.28) are different due to the difference in wavelength sensitivity ranges of the instruments. The flat response range of the DXP12 corresponds to the wavelengths in the regions of 3.33 - 5 mm or 11 - 17 ps, which means that this detector can resolve finer details of the observed bunch, compared to the BPR053W. In conclusion, the bunch shape instabilities in the machine make it very challenging to obtain fairly lengthy interferometric scans, which require 7 to 15 minutes to take.

Figure 7.29 demonstrates a current reading taken from the same shot as the signals in figure 7.28, the signal from BPM0195S demonstrates a stable current along the bunch train. The current stability and stability of the longitudinal parameters of the beam during the interferometric scan can be compared. In order to investigate the former, we can calculate the average current as a function of the time during the interferometric scan shown in figure 7.27. The latter can be analysed by calculating an average intensity over the entire signal acquired from the BPR as a function of the time during the same interferometric scan (the area confined within the two solid green lines in figure 7.28). It will give us the information how the power measured by the BPR in 26.4 - 40 GHz region of frequencies changes throughout the scan. Despite the fact that the interferometric measurement and the BPR scan cannot be compared directly, the BPR integrated intensity measurement can give qualitative information about the stability of the longitudinal parameters of the beam during the interferometric scan.

Figure 7.30 demonstrates the current as a function of the scan time, the average current is approximately 3.74 A and the stability is within 2 - 3 %. However when we draw our attention to the BPR scan, it is clear that the average intensity measured by BPR0532 changes by at least 20 % during the scan, which can significantly affect the interferometric measurement and which is demonstrated in the interferometric scan in figure 7.27. Although the central peak is clearly visible the tails of the interferogram are affected by the machine drifts, some points of the scan correspond to the measured intensities which change abruptly from one position of the mirror to another and do not have interferometric nature.

An additional measurement was taken by the same instruments and the average

Figure 7.30: Average current as a function of the scan time.
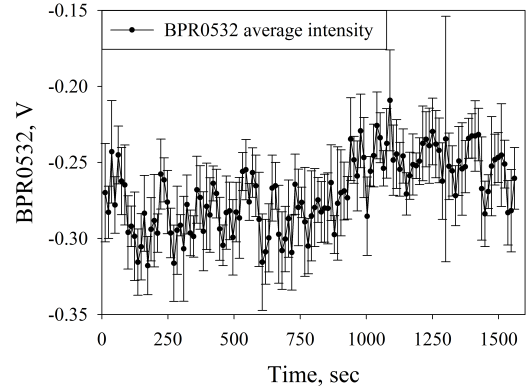
Figure 7.31: Average intensity of the BPR signal as a function of the scan time.

intensities of the observed signals were plotted as functions of the scan time. Figure 7.32 demonstrates the signal from the BPR located in the CTF3 transfer line 1. The intensity variation along the pulses is rather severe, compared with the current reading taken from the same shot (see figure 7.33).
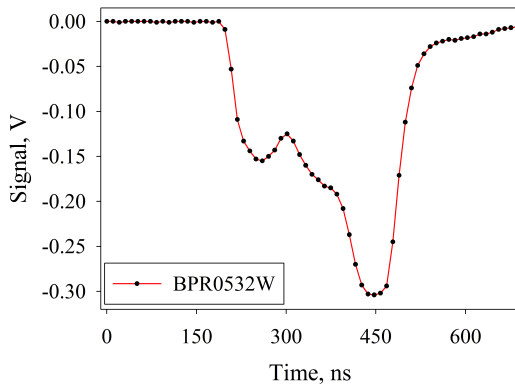
Figure 7.32: Signal from the BPR located in the CTF3 Transfer Line 1.
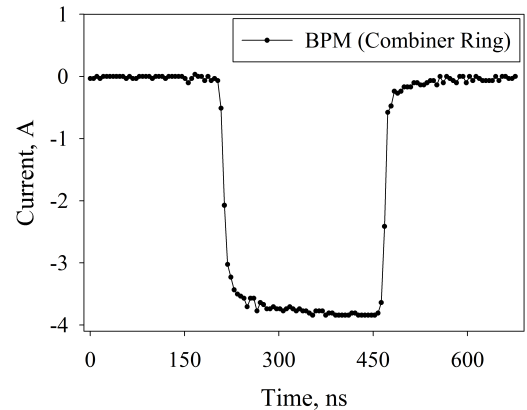
Figure 7.33: A sample current reading.

The shape of the BPR signal also changes from shot to shot, which is not obvious from figure 7.32. However if one plots the average intensity of the radiation detected by BPR0532W as a function of the time during the scan, the change in the average radiation intensity will be seen. The similar dependence can be plotted for the current reading throughout the scan. Figure 7.34 demonstrates a BPM average current scan, the current is relatively stable within 2 - 3 % with respect to the average value.

138

Figure 7.35 shows a BPR average intensity scan, it is clear that a significant variation of the measured power is observed, moreover it follows a periodic dependence with a period of approximately 50 seconds. If such a variation of the beam intensity overlaps with the interferometric measurement, it will inevitably compromise its quality and further applicability to the bunch shape reconstruction.
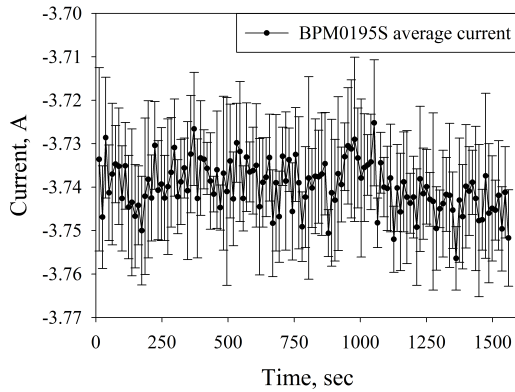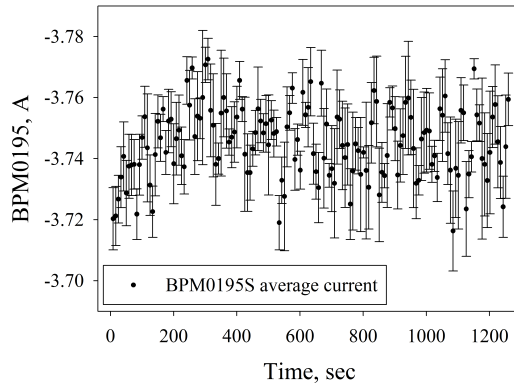

Figure 7.34: Average current as a function of the scan time.
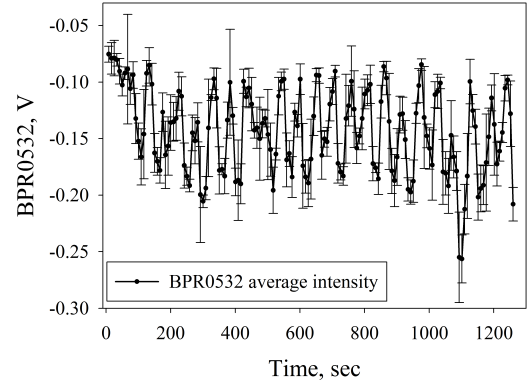
Figure 7.35: Average intensity of the BPR signal as a function of the scan time.

7.5 Summary

An overview of the experimental measurements obtained using the CDR experimental setup was presented. The results of the CDR spatial distribution measurements were discussed. Two detectors, demonstrating a flat frequency response in 50 - 75 GHz (DXP15) and 60 - 90 GHz (DXP12), were used in the experiment. All measurements were performed for two main positions of the first target: far from the beam or close to the beam (the same impact parameter as the second target).

The rotation and 2D scans of the CDR from the two target configuration were taken. The experimental results were compared with the theory. The vertical polarisation component was proven to be in a good agreement with the theory. Some discrepancies between the theory and the experiment were identified for the horizontal polarisation component of the CDR, namely the inequality of the peak intensities and the different depths of the radiation intensity minimum at the mirror reflection angle. The former could be explained by the fact that the targets are tilted with respect to the beam

propagation direction. The latter might be a consequence of the CSR background not being fully cut-off by the upstream target. In both instances additional experimental and theoretical studies are required.

The dedicated measurements of the CSR reflection from the second target for four positions of the upstream target in the beam pipe were performed. The ability of the first target to block the backgrounds originating upstream of the experimental setup was tested. A CSR intensity suppression with a factor five was achieved by the two-target system.

The interferometric measurements were performed at the experimental setup. Two interferograms were obtained using the same detector (DXP15) for two configurations of the targets. The general characteristics of the obtained spectra were reproducible, i.e. the spectra in both cases were narrow band and shifted towards higher frequencies.

One more interferogram was obtained using the DXP12 detector. During this measurement the signal from the online bunch shape monitor (BPR0532W) was recorded and was used to check the bunch shape and length stability during the measurement. A direct comparison of the current stability and the bunch shape stability during the interferometric scan was performed as well. The spectra obtained from the three interferometric measurements presented in this chapter can not be used for the bunch shape reconstruction directly. The narrow band detectors and the machine drifts, affecting the quality of the measurements, limit their applicability for this purpose.

Chapter 8

Main conclusions and outlook

The monitoring and control of the longitudinal bunch profile is crucially important for free-electron lasers (FELs) and future linear collides. The electron bunches in high-gain FELs are longitudinally compressed to achieve extremely high peak currents which are necessary to drive the FEL gain process. Monitoring of the longitudinal bunch profile is essential for the effective bunch compression. The Compact Linear Collider (CLIC) is a future linear collider aiming to achieve a 3 TeV centre of mass collision energy. In order to achieve a high luminosity at the CLIC Interaction Point and effective power production in Power Extraction and Transfer Structures the longitudinal bunch profile has to be monitored continuously during the beam's generation, acceleration and delivery. The development of a sufficiently fast, robust and non-invasive longitudinal bunch profile measurement system is essential. A low cost of the technique is also very important, as at least fifty longitudinal diagnostic stations are required for CLIC.

A frequency domain technique based on the detection of a Coherent Diffraction Radiation (CDR) spectrum is a promising candidate for a longitudinal diagnostic of very short bunches with the length down to femto-second region. A CDR technique is generally very advantageous for beam diagnostics due to the following reasons:

- no theoretical resolution limit on bunch length diagnostics;

- non-invasive nature;

- high radiation intensity due to a quadratic dependence on a beam charge;

- instantaneous emission allows for time-resolved measurements to be performed;

- well advanced Diffraction Radiation theory based on the Classical Electrodynamics;

- large emission angles for low background measurements.

In this thesis the process of the CDR emission from the dual-target system at CTF3 was investigated theoretically and experimentally . The dual-target system is a new type of a CDR generator proposed in this thesis. The overall simplicity of the suggested target configuration and its effectiveness for the radiation generation and transfer makes it a very good alternative to more conventional screen geometries, e.g. a slit between screens or a circular hole in a screen [35, 39, 43]. At the same time the dual target system has the following advantages:

- suppression of the backgrounds originating upstream of the experimental setup by the upstream target;

- the upstream target is additional source of CDR;

- possibility of multiple reflection suppression by installing an absorber in the upstream cross of the experimental setup;

- transverse kick compensation by positioning the targets at 45 degrees with respect to the beam propagation direction.

Now, an overview of this thesis shall be presented. An introduction to the working principles and the most challenging parameters of CLIC as well as a description of the CLIC Test Facility 3, which was built as a test bench for a novel drive beam acceleration scheme, were given in chapter 1. Chapter 2 was dedicated to the current state of the art in longitudinal diagnostics. Several techniques, such as the streak camera, the RF deflecting cavity, the RF pick-up and the electro - optic technique were discussed and their main advantages and disadvantages were identified. Coherent radiation techniques based on the emission of beam induced radiation were discussed in detail. In chapter 3 four radiative processes were considered: Synchrotron Radiation, Transition Radiation,

Diffraction Radiation and Smith-Purcell radiation. An overview of the experimental investigations of these processes in application to longitudinal diagnostics was presented as well.

In chapter 4 a new theoretical model developed during the PhD program and dedicated to the calculation of the CDR characteristics from the two-target system was introduced. The main purpose of the developed model is to calculate a single electron spectrum, which is an essential step towards the bunch profile reconstruction procedure. The single electron spectrum is used to normalise the measured CDR spectrum in order to retrieve the longitudinal bunch form factor. A comprehensive analysis of the CDR geometry was performed. A computer code for simulating the CDR characteristics was developed and tested. The main features of the CDR spatial distributions were identified: the vertical polarisation has a single peak at the mirror reflection angle from the second target, the horizontal polarisation component has a dual mode shape and significantly less intense than the vertical polarisation. A dominance of the vertical polarisation component in the final distribution was identified, however for some wavelengths the final distribution changes under the influence of the horizontal polarisation component which is modulated as a function of wavelength. The radiation from the targets positioned at the same distance from the beam is suppressed due to the destructive interference, but still measurable.

Chapter 5 was dedicated to a theoretical work towards longitudinal diagnostics which was performed during the PhD program. After the longitudinal form factor is determined, the main challenge of retrieving the beam parameters from a spectral measurement is missing phases of electrons in the bunch. In this thesis the Kramers-Kronig technique was studied as a tool for the phase and longitudinal profile reconstruction. Two different scenarios of the form factor spectral coverage were considered. It was pointed out that the bunch profile reconstruction can be accurate only if the form factor data points are obtained over a broad range of frequencies. The development of a detection system which would provide this capability is very important. One may consider usage of a grating spectrometer. If one grating is used, the spectrometer is only able to provide a coverage of very small part (one octave) of the coherent radiation spectrum. Therefore several gratings have to be used in order to provide a sufficient

coverage of several octaves in the spectrum for an accurate bunch profile reconstruction. In this case the gratings must be changed during the measurements, which increases the measurement time and does not allow for a single shot mode of operation to be performed. Alternatively, several gratings can be used at the same time, but in this case different parts of the radiation spatial distribution are measured and the calculation of the detection system response function is rather complex.

A detailed description of the CDR experiment hardware and controls was given in chapter 6. The upgrade of the experimental setup was performed in the period of 2010 - 2011 and included installation of an additional target, an UHV actuator in the upstream cross and the modification of the measurement system. One of the main motivations for installation of the additional target was the suppression of the backgrounds originating upstream of the experimental setup, e.g. coherent Synchrotron Radiation (CSR) and wakefields.

An overview of the experimental measurements obtained using the CDR setup was presented in chapter 7. Two detectors demonstrating a flat frequency response in 50 - 75 GHz (DXP15) and 60 - 90 GHz (DXP12) were used in the experiment. The vertical polarisation component of the CDR was proven to be in a reasonable agreement with the theory. Some discrepancies between the theory and the experiment were identified for the horizontal polarisation component of the CDR, namely the inequality of the peak intensities and the different depths of the radiation intensity minimum at the mirror reflection angle. The former could be explained by the fact that the targets are tilted with respect to the beam propagation direction. The latter might be a consequence of the CSR background not being fully cut-off by the upstream target. In both instances additional experimental and theoretical studies are required.

The ability of the first target to block the backgrounds originating upstream of the experimental setup was tested. A CSR intensity suppression by a factor five was achieved in the two-target system. The residual part of the CSR might still distort the CDR spectrum and therefore additional investigations are required.

Systematic interferometric measurements were performed with the experimental setup. The interferograms were obtained using the DXP15 detector for two configurations of the targets. The general characteristics of the obtained spectra were repro-

ducible, i.e. the spectra in both cases were narrowband and shifted towards higher frequencies. One more interferogram was obtained using the DXP12 detector. A direct comparison of the current stability and the bunch shape stability during the interferometric scan was performed. The spectra obtained from the interferometric measurements could not be used for the bunch shape reconstruction directly. The narrow band detectors and the bunch shape instabilities limit their applicability for this purpose.

As an outlook, several issues have to be addressed here as regard to the detection system of the CDR experiment. An immediate solution to the bunch shape instability could be a usage of the broadband detector sensitive into the frequencies below 100 GHz to reduce the sensitivity of the detection system to micro-bunching. However, this will compromise the ability of the system to measure the high frequency tail of the form factor, which is very important for an accurate bunch profile reconstruction. Moreover, such a fast and broadband detector is not commercially available at present, but a broadband Schottky detector is currently being developed by some technology companies.

A long term solution would be the development of a single shot spectrometer that provides a broad spectral coverage. A single shot mode of operation should eliminate the problem of the changing bunch profile from shot to shot. In [34] Wesch with colleagues developed a multi-channel THz and infrared spectrometer for femtosecond single-shot electron bunch diagnostics using coherent Transition Radiation. The spectrometer was equipped with five consequitive dispersion gratings and it could be operated in short wavelengths mode (5 - 44 μm) as well as in long wavelengths mode (45 - 430 μm). The signal from each grating was transferred via a ring mirror towards an array of thirty pyroelectric detectors. A similar scheme could be used for the setup at CTF3, however a development of more sensitive and sufficiently fast detector array would be required. Moreover, an accurate calculation of the response function for such a complex arrangement of gratings is not a trivial task.

One may also consider an idea of a single shot interferometer shown in figure 8.1. The signal is not recombined at the splitter as it is done in a Michelson interferometer. Half of the radiation is reflected from the splitter and another half is transmitted by the splitter, then the radiations are reflected from the mirrors M1 and M2 and recom-
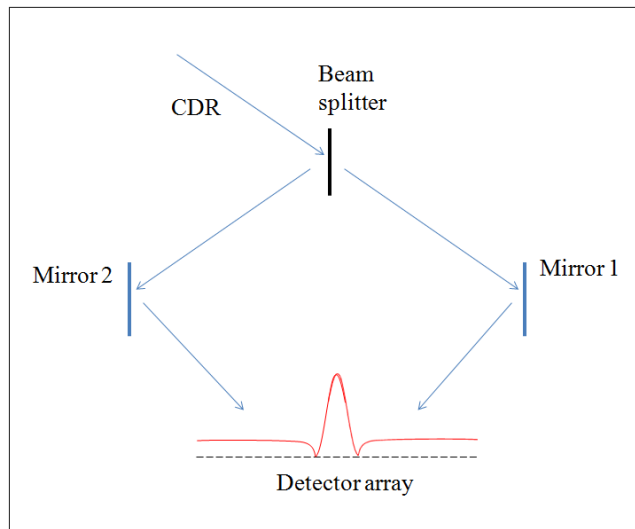
Figure 8.1: A possible scheme for a single shot interferometer.

bined at the observation plane where they are registered by a detector array. In this configuration the development of a sufficiently broadband detector is very important as all the necessary spectral information has to be recorded in one pass.

Appendix A

Fresnel's Integrals

We shall consider two types of the Fresnel's integrals $C(z) = \int\limits_0^z \cos\left(\frac{\pi}{2}t^2\right) dt$ and $S(z) = \int\limits_0^z \sin\left(\frac{\pi}{2}t^2\right) dt$. The rational approximation of the integrals can be written as [76]:

$$C(z) = \frac{1}{2} + \frac{1 + 0.926z}{2 + 1.792z + 3.104z^2} \sin\left(\frac{\pi}{2}z^2\right) - \frac{1}{2 + 4.142z + 3.492z^2 + 6.67z^3} \cos\left(\frac{\pi}{2}z^2\right),$$

(A.1)

$$S(z) = \frac{1}{2} - \frac{1 + 0.926z}{2 + 1.792z + 3.104z^2} \cos\left(\frac{\pi}{2}z^2\right) - \frac{1}{2 + 4.142z + 3.492z^2 + 6.67z^3} \sin\left(\frac{\pi}{2}z^2\right).$$

(A.2)

The Fresnel's integrals also follow the rule:

$$C(z) = \begin{cases} C(z) & \text{if } z > 0 \\ -C(|z|) & \text{otherwise} \end{cases} ; S(z) = \begin{cases} S(z) & \text{if } z > 0 \\ -S(|z|) & \text{otherwise.} \end{cases}$$

(A.3)

T_i terms

The terms T_i containing the Fresnel's integrals can be expressed as:

$$T_1(x_1, \xi) = C(t_1(x_1, \xi)) - C(t_2(x_1, \xi)), T_2(y_1, \eta) = C(t_3(y_1, \eta)) - C(t_4(y_1, \eta)); \quad \text{(B.1)}$$

$$T_3(x_1, \xi) = S(t_1(x_1, \xi)) - S(t_2(x_1, \xi)), T_4(y_1, \eta) = S(t_3(y_1, \eta)) - S(t_4(y_1, \eta)); \quad \text{(B.2)}$$

where

$$t_1(x_1, \xi) = \sqrt{\frac{2(a+d)}{\lambda a d}} \left(x_{hight} + impact - \frac{ad}{a+d} \left(\frac{x_1}{d} + \frac{\xi}{a} \right) \right), \quad \text{(B.3)}$$

$$t_2(x_1, \xi) = \sqrt{\frac{2(a+d)}{\lambda a d}} \left(impact - \frac{ad}{a+d} \left(\frac{x_1}{d} + \frac{\xi}{a} \right) \right), \quad \text{(B.4)}$$

$$t_3(y_1, \eta) = \sqrt{\frac{2(a+d)}{\lambda a d}} \left(\frac{y_{width}}{2} - \frac{ad}{a+d} \left(\frac{y_1}{d} + \frac{\eta}{a} \right) \right), \quad \text{(B.5)}$$

$$t_4(y_1, \eta) = \sqrt{\frac{2(a+d)}{\lambda ad}} \left(-\frac{y_{width}}{2} - \frac{ad}{a+d} \left(\frac{y_1}{d} + \frac{\eta}{a} \right) \right), \tag{B.6}$$

$x_{hight} + impact$ and $impact$ are the coordinates which correspond to the upper and the lower edges of the first target, and $-y_{width}/2$ with $y_{width}/2$ correspond to the left and the right edges of the first target.

Bibliography

[1] CLIC Conceptual Design Report (latest preliminary version, as of January, 2012) Chapter: The CLIC Concept: Key Issues and feasibility ("Introduction" section).

[2] CLIC Conceptual Design Report (latest preliminary version, as of January, 2012) Chapter: The CLIC Concept: Key Issues and feasibility ("CLIC Scheme Overview" section).

[3] CLIC Conceptual Design Report (latest preliminary version, as of January, 2012) Chapter: The CLIC Concept: Key Issues and feasibility ("Drive beam generation" section).

[4] CLIC Conceptual Design Report (latest preliminary version, as of January, 2012) Chapter: The CLIC Concept: Key Issues and feasibility ("Key issues" section).

[5] A. Chao and M. Tigner, *Handbook of Accelerator Physics and Engineering*, 3 ed. (World Scientific, 1999).

[6] H. Braun et al., "The CLIC RF power source: a novel scheme of two-beam acceleration for electron-positron linear colliders, CLIC-Note-364 (1998).

[7] CLIC Conceptual Design Report (latest preliminary version, as of January, 2012) Chapter: CLIC Parameter tables.

[8] R. Corsini, Proc. PAC'01, Chicago (USA) p. 412 (2001).

[9] G. Geschonke *et al.*, CERN/PS 2002-008 (RF), CERN (2002).

[10] F. Tecker et.al., Proc. PAC'03, Portland (USA) p.684 (2003).

[11] CLIC Conceptual Design Report (latest preliminary version, as of January, 2012) Chapter: CLIC technologies demonstrated at CTF3.

[12] E. Adli et al., Proc. IPAC 2010, Kyoto (Japan), p.4410 (2010).

[13] A. Dabrowski, "Longitudinal Diagnostics at CTF3", Talk at DITANET workshop on longitudinal diagnostics (2010).

[14] C. Welsch *et al.*, Journ. of Instrument. **1**, P09002 (2006).

[15] A. Dabrowski et al., Proc. of LINAC10, Tsukuba (Japan), p.647 (2010).

[16] Hamamatsu streak cameras, http://sales.hamamatsu.com/en/products/system-division/ultra-fast/streak-systems/part-c6138.php.

[17] D. Alesini et al., "CTF3 Bunch Length Measuremnt with 1.5 GHz RF deflector", CTFF3-010 Technical Note (2007).

[18] R. Akre et al., PAC'01, Chicago, IL, p. 2353 (2001).

[19] M. Hüning et al., Proc. FEL 2005, Stanford (USA), p. 538 (2005).

[20] A. Dabrowski et al., Proc. of LINAC08, Victoria, BC (Canada), p.588 (2008).

[21] S. Jamison et al., Proc. of EPAC'06 (TUYPA01), Edinburgh (UK), p.915 (2006).

[22] B. Steffen *et al.*, Physical Review Special Topics - Accelerator and Beams **12**, 032802 (2009).

[23] A. Debus *et al.*, Physical Review Letters **104**, 084802 (2010).

[24] Lecture on "Role of Electromagnetic Radiation in Charged Particle Bunch Length Diagnostics" by Dr Pavel Karataev, DITANET Beam Diagnostics School, Royal Holloway UoL, Egham, UK (2009).

[25] J. Nodvick and D. Saxon, Physical Review **96**, 180 (1954).

[26] A. P. Potylitsyn, M. I. Ryazanov, M. N. Strikhanov, and A. A. Tishchenko, *Diffraction Radiation from Relativistic Particles*, 1 ed. (Springer Tracts in Modern Physics, 2011).

[27] I. Gradshteyn and I. Ryzhik, *Table of integrals, series and products*, 7 ed. (ISBN number: 0-12-373637-4, 2007).

[28] T. Nakazato, Phys. Rev. Lett. **63**, 1245 (1989).

[29] L. Frohlich and O. Grimm, Proc. FEL 2005, Stanford (USA), p.114 (2005).

[30] I. M. Frank and V. Ginzburg, J. Phys. (Moscow) **9**, 353 (1945).

[31] U. Happek, A. Sievers, and E. Blum, Phys. Rev. Lett. **67**, 2962 (1991).

[32] Y. Shibata *et al.*, Phys. Rev. E **50**, 1479 (1994).

[33] P. Kung *et al.*, Phys. Rev. Lett. **73**, 967 (1994).

[34] S. Wesch et al., "A multi-channel THz and infrared spectrometer for femtosecond electron bunch diagnostics by single-shot spectroscopy of coherent radiation", arXiv:1109.0458v1 [physics.ins-det] (2011).

[35] M. L. Ter-Mikaelian, *High-Energy Electromagnetic Processes in Condensed Media* (Wiley-Interscience, 1972).

[36] A. Potylitsyn, Nucl. Instrum. and Meth. in Phys. Res. B **145**, 169 (1998).

[37] T. Muto *et al.*, Physical Review Letters **90**, 104801 (2003).

[38] I. Vnukov *et al.*, JETP Letters **67**, 802 (1998).

[39] Y. Shibata *et al.*, Phys. Rev. E **52**, 6787 (1995).

[40] Y. Shibata *et al.*, Physical Review E **52**, 6787 (1995).

[41] K. Ishi *et al.*, Phys. Rev. A **43**, 5597 (1991).

[42] Y. Shibata *et al.*, Phys. Rev. E **49**, 785 (1994).

[43] M. Castellano *et al.*, Phys. Rev. E **63**, 056501 (2001).

[44] I. Frank, Izv. Akad. Nauk. SSSR, Ser. Fiz. **6**, 3 (1942).

[45] W. Salisbury, U.S. Patent No. 2,634,372(26 October 1949).

[46] S. Smith and E. Purcell, Phys. Rev. **92**, 1069 (1953).

[47] K. Lekomtsev, M. Strikhanov, and A. Tishchenko, Journal of Physics: Conference Series **236**, 012023 (2010).

[48] F. G. de Abajo, Phys. Rev. E **61**, 5743 (2000).

[49] N. Horiuchi *et al.*, Phys. Rev. E 74 , 056601 (2006).

[50] G. T. di Francia, Nuovo Cimento **16**, 61 (1960).

[51] K. Ishi *et al.*, Phys. Rev. E **51**, R5212 (1995).

[52] G. Doucas *et al.*, Phys. Rev. Special Topics - Accelerators and beams **9**, 092801 (2006).

[53] D. Karlovets and A. Potylitsyn, Phys. Rev. Special Topics - Accelerators and beams **9**, 080701 (2006).

[54] V. Blackmore *et al.*, Phys. Rev. Special Topics - Accelerators and beams **12**, 032803 (2009).

[55] A. Potylitsyn, P. Karataev, and G. Naumenko, Phys. Rev. E **61**, 7039 (2000).

[56] A. Potylitsyn, D. Karlovets, and G. Kube, Nucl. Instrum. and Meth. in Phys. Res. B **266**, 3781 (2008).

[57] K. Lekomtsev and L. Sukhikh, Draft chapter on Coherent Radiation techniques, DITANET booklet (to be published in 2012).

[58] K. Lekomtsev *et al.*, Il Nuovo Cimento **34C**, 261 (2011).

[59] P. Karataev, Physics Letters A **345**, 428 (2005).

[60] P.V. Karataev, Lecture on "Fourier Transform Spectroscopy", Department of Physics at Royal Holloway University of London, Egham, UK, 2012.

[61] P. Jacquinot, Appl. Opt. **8**, 497 (1969).

[62] P. Karataev *et al.*, Nuclear Instruments and Methods in Physics Research B **227**, 198 (2005).

[63] R. Lai and A. J. Sievers, Phys. Rev. E **50**, R3342 (1994).

[64] R. Lai and A. J. Sievers, Phys. Rev. E **50**, R4294 (1994).

[65] M. Micheler *et al.*, Journal of Physics: Conference Series **236**, 012021 (2010).

[66] O. Grimm and P. Schmuser, "Principles of Longitudinal Beam Diagnostics with Coherent Radiation", TESLA-FEL Internal Report (2006).

[67] M. Micheler, "Development of Longitudinal Diagnostics for Electron Beams based on Coherent Diffraction Radiation", PhD Thesis, Royal Holloway UL (2010).

[68] Courtesy of the CLIC/CTF3 study group.

[69] S. Casalbuoni et al., Far-Infrared Transition and Diffraction Radiation; Part 2: The THz beamline at the VUV-FEL Linac, TESLA-FEL 2006-04.

[70] Microtech Instruments, Wire Grid Polarisaers Data Sheet, www.mtinstruments.com.

[71] Millitech, Series DXP General Purpose Detectors Datasheet, www.millitech.com.

[72] G.E. Ponchak, Note on "Metal-Semiconductor Junctions", California Institute of Technology (http://parts.jpl.nasa.gov/mmic/3-II.PDF).

[73] A. Aryshev *et al.*, Nuclear Instruments and Methods in Physics Research A **580**, 1544 (2007).

[74] K. Lekomtsev et al., "Investigation of Coherent Diffraction Radiation from a Dual Target system at CTF3", Journal of Physics: Conference Series, (the paper has been accepted), (2012).

[75] K. Lekomtsev et al., Proc. of LINAC10, Tsukuba (Japan), p. 644 (2010).

[76] C. Brezinski and M. Redivo Zaglia, *Extrapolation methods theory and practice* (ELSEVIER, 1991).